# Diffusion of guest molecules through small-pore zeolites studied with advanced molecular dynamics simulations

Pieter Janssens

Supervisors: Prof. dr. ir. Veronique Van Speybroeck, Prof. dr. ir. An Ghysels

Master's dissertation submitted in order to obtain the academic degree of
Master of Science in Engineering Physics

Department of Applied Physics
Chair: Prof. dr. ir. Christophe Leys
Faculty of Engineering and Architecture
Academic year 2015-2016

UNIVERSITEIT
GENT


This research was conducted at the Center for Molecular Modeling.

# Preface

Many people deserve words of gratitude in the realization of this master thesis. First and foremost, I would like to express my appreciation and gratitude to prof. dr. ir. Veronique Van Speybroeck and prof. dr. ir. An Ghysels, whose expertise, guidance, and support has been indispensable in the completion of this work.

I would like to express my gratitude to ir. Ruben Demuynck and dr. ir. Kristof De Wispeleare. I am genuinly thankful for their daily enthusiasm, guidance, precious advice, and valuable comments which made this thesis not only an educational, but also enjoyable experience.

Let's not forget to thank my fellow thesis students, Klaas, Michiel, Yentl, Senne, and Titus for creating a pleasant atmosphere and sharing many fun lunch breaks. Thank you for the many memories I will take away.

There is not enough room to thank all the people of the CMM who have supported me throughout the year. Inevitably, some people are left out. However, I am grateful to you too. Thank you!

Finally, I would also like to thank my wonderful girlfriend, family, and friends for their kind support and everlasting patience.

# Copyright agreement



Pieter Janssens, June 2016

# Diffusion of guest molecules through small-pore zeolites studied with advanced molecular dynamics simulations

by Pieter Janssens

Supervisors: prof. dr. ir. Veronique Van Speybroeck, prof. dr. ir. An Ghysels
Councellors: ir. Ruben Demuynck, dr. ir. Kristof De Wispelaere

Master's dissertation submitted in order to obtain the academic degree of
Master of Science in Engineering Physics

Department of Applied physics
Chair: prof. dr. ir. Christophe Leys
Faculty of Engineering and Architecture
Academic year 2015–2016

## Summary

The free energy barrier for diffusion of propylene through the narrow eight-rings of H-SAPO-34, a small-pore zeolite, is studied using advanced classical molecular dynamics simulations. The influence of the temperature, the number of acid sites in the eight-ring, and of the presence of additional spectator molecules is assessed. It is observed that the free energy barrier is dominated by its entropic contribution. We found the addition of extra acid sites to the ring does not have a significant effect on the free energy barrier. As extra spectator molecules are added to the cages, the diffusion barrier is lowered, which opens up interesting perspectives to study diffusion pathways of propylene through zeolites at realistic loading conditions.

## Keywords

molecular dynamics, metadynamics, diffusion, enhanced sampling techniques, H-SAPO-34, methanol-to-olefins process

# Diffusion of guest molecules through small-pore zeolites studied with advanced molecular dynamics simulations

Pieter Janssens
Supervisors: prof dr. ir. Veronique Van Speybroeck and prof dr. ir. An Ghysels
Counsellors: ir. Ruben Demuynck and dr. ir. Kristof De Wispelaere

*Abstract*—**The free energy barrier for diffusion of propylene through the narrow eight-rings of H-SAPO-34, a small-pore zeolite, is studied using advanced molecular dynamics simulations. The influence of the temperature, the number of acid sites in the eight-ring, and of the presence of additional spectator molecules is assessed. It is observed that the free energy barrier is dominated by its entropic contribution. We found the addition of extra acid sites to the ring does not have a significant effect on the free energy barrier. As extra spectator molecules are added to the cages, the diffusion barrier is lowered, which opens up an interesting perspectives to study diffusion pathways of propylene through zeolites at realistic loading conditions.**

*Keywords*—**molecular dynamics, metadynamics, diffusion, H-SAPO-34, MTO process**

## I. Introduction

Today, catalysts play a pivotal role in the chemical industries. Zeolites are among the most popular materials for catalyst applications, which is due to their special nanoporous structure, and also due to the fact that Brønsted acid sites can be introduced. Without a doubt, the most important application of zeolites in catalysis is the refining of crude oil into high quality fuels and other byproducts of petroleum.

However, oil reserves are depleting and the demand for base chemicals is rapidly increasing. With the *methanol to olefins* (MTO) process, one can produce base chemicals such as ethylene and propylene from non-oil sources such as natural gas, coal, or biomass. This conversion happens via a complex catalytic cycle that is not yet fully understood.

The main focus of this work is to explore the validity and applicability of advanced molecular dynamics techniques based on force fields to study the diffusion of propylene through the small eight-rings of H-SAPO-34, one of the most promising and industrially relevant catalysts for the MTO process [1].

The influence of the temperature, the ring chemistry, and the pore loading on the diffusion of propylene through H-SAPO-34, has been assessed. Knowledge of the diffusion barrier and a profound insight into its determinants facilitates a deeper understanding of the product-shape selectivity in H-SAPO-34 and the product distribution of the MTO process [2]. As diffusion of propylene is a rare event on the time scale of classical molecular dynamics simulations, enhanced sampling techniques are required. Additionally, an attempt is made to recover kinetic information from biased simulations using transition state theory.

## II. Methodology

The free energy barrier for diffusion of propylene is studied in H-SAPO-34, a silico-alumino-phosphate material with a chabazite (CHA) topology. It consists of large elliptical chabazite cages (10.0 $\times$ 6.7 Å), interconected by small 8-ring windows (3.8 $\times$ 3.8 Å). To determine this free energy barrier, a propylene molecule is actively pushed through an 8-ring during metadynamics simulations. This procedure is repeated at different temperatures for different rings with a varying number of acid sites. Figure 1 provides an overview of the four distinct types of 8-rings that have been defined. A type I ring contains no acid sites. In a type II ring, a P atom has been substituted for a Si atom, the charge-compensating proton is located in an adjacent 8-ring. A type III ring is similar but now the proton is in the ring itself. An extra acid site had been added to create a type IV ring.

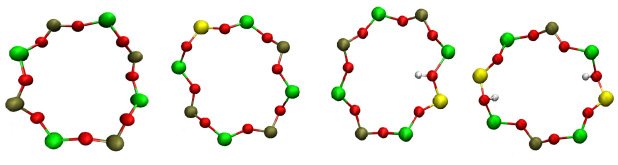

**(a)** Type I **(b)** Type II **(c)** Type III **(d)** Type IV

**Figure 1:** Definition of the 4 ring types. O atoms are red, Al atoms are green, Si atoms are yellow, P atoms are brown, and H atoms are white.

### II.1. Ab initio simulations

To account for the negative thermal expansion of H-SAPO-34 [3], inital ab initio MD simulations of empty H-SAPO-34 unit cells have been performed. The DFT calculations have been carried out with the CP2K software package [4], using a hybrid Gaussian and plane wave (GPW) basis set. The revPBE functional was chosen over the PBE functional for its improved performance for solid-state calculations. These relaxations have been performed in the NPT-ensemble for two distinct unit cells at three temperatures (300 K, 450 K, 600K) and at a pressure of 1 atm. The temperature was controlled by a chain of 5 Nosé-Hoover termostats, and the pressure by a Martyna-Tobias-Klein (MTK) barostat. The first unit cell contains one Brønsted acid site, the second unit cell has a ring with two Brønsted acid sites. The total simulation time is 20 ps (40000 integration steps of 0.5 fs). From these trajectories, the most reoccuring unit cell shape was employed to construct a 2 $\times$ 2 $\times$ 2 supercell, which was subsequently used as a starting structure for the force field simulations in the NVT-ensemble.

### II.2. Force field simulations

The molecular dynamics engine used for the force field calculations is DL_POLY Classic (version 1.9) [5]. All MD simulations were performed in the NVT-ensemble where the temperature is controlled by means of a Nosé-Hoover thermostat with a coupling time of 1 ps. The Nosé-Hoover thermostat only lightly perturbs the dynamics of the system, so that the true dynamic quantities can nearly exactly be recovered. This is crucial when modeling diffusion. The velocity Verlet integrator was used with a time step of 1 fs. Long-range interactions are evaluated using the smoothed particle mesh Ewald method with a cutoff radius of 11.8 Å.
The potential energy surface is defined by a flexible force field that can handle zeolites and silico-aluminophosphate (SAPO) materials with any (Si, Al, P) distribution and with Brønsted acid sites [6].

### II.3. Collective variable

The construction of the free energy profile requires the definition of a collective variable. The collective variable should be able to distinguish between the different stable states and the transition states. Here, the coordinate $\xi$ is used to describe the position of a molecule with respect to a ring. $\xi$ is the projection of the center of mass of the molecule onto the axis that is normal to the ring plane and goes through the geometrical center of the ring (Figure 2). Ring crossings occur when $\xi$ changes sign.

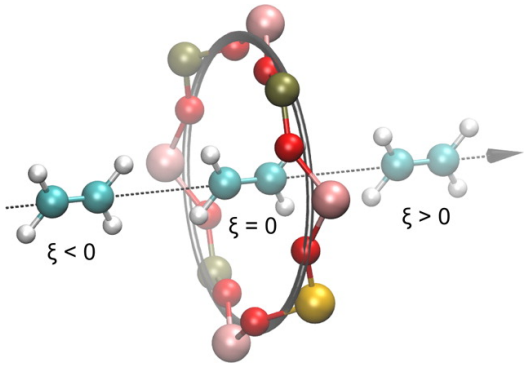


**Figure 2:** A graphical representation of the collective variable. The center of mass of the ethylene molecule is projected onto the $\xi$-axis. Figure taken from Ref. [6].

### II.4. Restraints

The collective variable depends on the position of the propylene molecule and the geometrical center of the ring, which implies both the propylene molecule and the ring molecules will feel the influence of the metadynamics potential. To eliminate framework translation, the ring under study is fixed by a harmonic potential with a force constant of 1500 kJ.mol$^{-1}$/Å$^2$.
Two additional restraints are added to prevent the molecule from escaping through a different ring than the one under investigation. Harmonic walls are placed at $\pm$ 8.5 Å along the $\xi$-axis with a force constant of 1500 kJ.mol$^{-1}$/Å$^2$. The distance to the $\xi$-axis ($\equiv r$) has also been restricted to a maximum of 5.0 Å by means of a harmonic wall, again using a force constant of 1500 kJ.mol$^{-1}$/Å$^2$. The position of the harmonic walls has been chosen so that the natural motion of the propylene molecule in the cages is not hindered.

### II.5. Enhanced sampling simulations

The free energy calculations have been performed with PLUMED, an open source library for free energy calculations in molecular systems [7]. In the metadynamics simulations, the gaussian hills have a height of 0.5 Å kJ.mol$^{-1}$ and a width of 0.5 Å. The deposition stride is 5000 integration steps (corresponding to a metadynamics time of 5 ps). The average free energy profile is determined by running 10 independent metadynamics simulations and subsequently averaging them out. The size of the error bars in one standard deviation.
To eliminate obvious mistakes in the implementation of the metadynamics calculations, the free energy barrier has also been determined by umbrella sampling. Figure 3 shows a very good correspondence between both free energy methods.
For the umbrella sampling simulations, 50 umbrellas with a force constant of 100 kJ.mol$^{-1}$/Å$^2$ are centered

on 50 equidistant points ranging from -5 Å to 5 Å along the ξ-axis. This high value for the force constant is necessary to ensure sufficient sampling in the region around the top of the barrier. The error bars are again the size of one standard deviation and have been calculated using a bootstrap method.

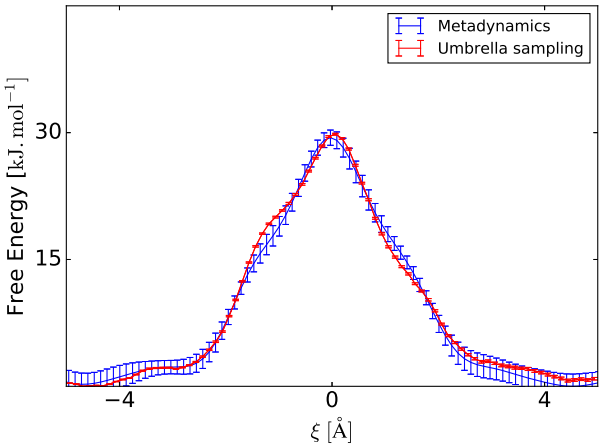


**Figure 3:** Free energy profile for propylene crossing a type II ring determined via two different methods: metadynamics (blue) and umbrella sampling (red).

As an additional verification, the free energy barrier was also determined with metadynamics for an ethylene molecule at 450 K. A free energy barrier height of 31.9 kJ.mol$^{-1}$ was obtained, which is in agreement with the barrier height Ghysels *et al.* found by using classical MD simulations with the same force field [6].

## III. Results and discussion

### III.1. Influence of temperature

The free energy barrier has been determined at 300 K, 450 K, and 600 K for each of the four ring types defined in Figure 1. An increase of the diffusion barrier from roughly 30 kJ.mol$^{-1}$ at 300 K to around 50 kJ.mol$^{-1}$ has been observed (Table 1). These values correspond to 12 $k_BT$ and 10 $k_BT$ respectively. Hence, at higher temperatures, a higher diffusion coefficient is expected. Figure 4 shows the free energy profiles for a type I ring. Similar behavior is observed for the other ring types.
The free energy barrier consists of two contributions: an energetic barrier and an entropic barrier.
At 300 K, the energetic barrier is approximately 9 kJ.mol$^{-1}$ and it rises to about 14 kJ.mol$^{-1}$ at 600 K. This small increase of 5 kJ.mol$^{-1}$ is likely caused by the negative thermal expansion coefficient of H-SAPO-34 and the associated reduction of the accessible window area of the ring as defined by Ghysels *et al* in Ref. [6]. At all temperatures, the energetic barrier makes up no more than one third of the free energy barrier.

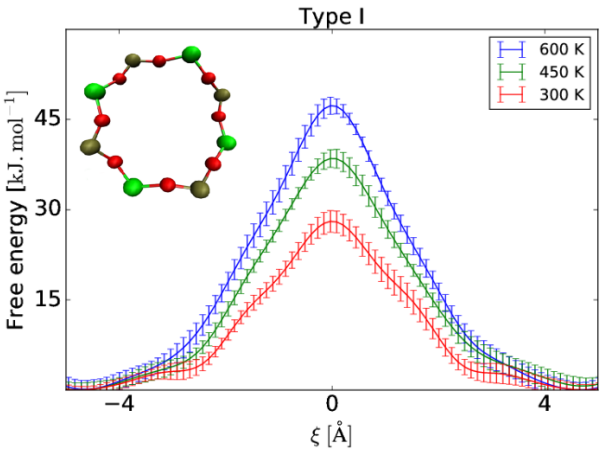


**Figure 4:** Free energy profile along the ξ-axis for a type I ring. The free energy barrier sharply raises with temperature, from around 30 kJ.mol$^{-1}$ to about 50 kJ.mol$^{-1}$.

Clearly, the dominant contribution to the free energy barrier for diffusion is the entropic barrier (-TS). The entropic barrier is due to the tight fit of the propylene molecule in the small eight-rings, which forces the molecule into a very limited set of configurations when pushed through the ring. Increasing the temperature further enhances this effect because of a decrease in the accessible window area caused by the negative thermal expansion coefficient of H-SAPO-34. However, this is likely a minor effect, as the temperature dependence of the entropic barrier (-TS) is fairly linear. This can be deduced by comparing the free energy and energy barrier heights at the three different temperatures. When the temperature doubles, the free entropic barrier (-TS) also approximately doubles.

### III.2. Influence of ring chemistry

To assess how the presence of an acid site in an eight-ring affects the free energy barrier, the analysis above has been repeated for each of the four ring types. Table 1 lists the average heights of the free enery barriers. The influence of the ring chemistry on the free energy barrier is not immediatly clear from Table 1. Surprisingly, the free energy barrier is lower for a type IV ring, which has two acid sites, than for a type III ring, which has only one acid site.
In Ref. [6], it is found that diffusion is considerably slower in materials with acid sites. Here no significant influence of the acid sites on the height of the free energy barriers is found. A diffusion coefficient can be interpreted as an attempt rate multiplied by a success

rate and the height of the free energy barrier is related to the success rate. The small differences in the heights of the free energy barrier alone are most likely not enough to adequatly explain why diffusion is slower in acidic materials. This suggests that the presence of acid sites might affect the attempt rate, which is related to the motion of the molecules in the cages.

**Table 1:** Overview of the average free energy barrier heights for each of the four ring types. Standard deviations have been provided. Units are in kJ.mol$^{-1}$.

| | Type I | Type II | Type III | Type IV |
|---|---|---|---|---|
| 300 K | 28.1 (1.8) | 29.4 (0.9) | 31.6 (1.9) | 25.7 (1.9) |
| 450 K | 38.5 (1.5) | 41.5 (1.2) | 41.7 (1.8) | 38.3 (1.8) |
| 600 K | 47.3 (1.4) | 49.5 (1.4) | 50.6 (1.8) | 50.4 (2.0) |

### III.3. Increasing the pore loading

During the transport of the product species in the MTO process, it is probable that situations arise in which multiple propylene molecules share a cage. To assess the influence of the pore loading on diffusion, simulations with extra propylene molecules inside the cages have been performed. To prevent these spectator molecules from escaping their cages, the projections on the $\xi$-axis of these molecules and their distance to the $\xi$-axis ($r$) is restrained. For example, the spectator molecules in Figure 5 can move freely in a cylindrical space with $\xi$ ranging from 0 Å to 8.5 Å, and with $r$ from 0 Å to 5 Å.

In case of one extra spectator molecule per cage, the effect on the free energy barrier is lowered by approximately 5 kJ.mol$^{-1}$. However, when two spectator molecules are present in a cage a more substantial decrease of about 20 kJ.mol$^{-1}$ is observed, as can clearly be seen in Figure 5. As the intermolecular interactions between propylene molecules are weak, this is most likely an entropic effect. The molecules inside the cage struggle for space and experience a more limited freedom of motion, lowering the entropy inside the cage.

Another feature of the free energy profile in Figure 5 that stands out is the fact that the error bars on the right hand side are noticeably larger. This is due to the fact that, with the addition of the spectator molecules, new degrees of freedom have been added to the system. Properly sampling these degrees of freedom takes a very long time, hence the bigger error bars.

In Ref. [6], it was found that for propylene, diffusion itself is a rare event at the time scale of MD simulations and that it is impossible to extract meaningful quantitative information. However, the sizeable reduction of the free energy barrier at higher pore loadings opens up interesting new perspectives. Whereas Ghysels *et al.* performed MD simulations with a loading of one or two molecules per cage, the results here suggest that simulations with higher pore loadings, for example three to four molecules per cage, are better suited for a kinetic study of diffusion. Whether such loadings are relevant for the MTO process of course depends on the operating conditions.

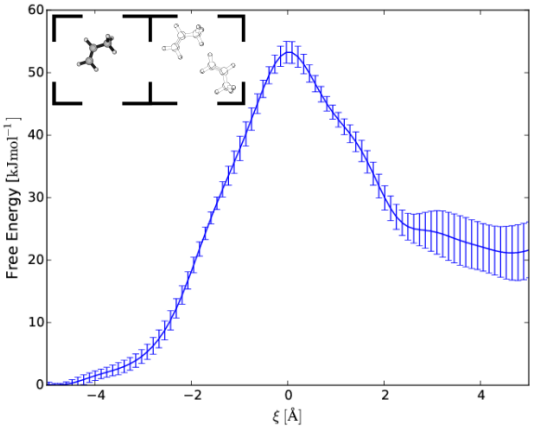


**Figure 5:** An asymmetrical situation with three propylene molecules. Top left panel: the coloured propylene molecule is actively pushed through the ring by means of a metadynamics bias. The transparent propylene molecules are simply spectator molecules and are confined to their cages. Bottom panel: the free energy profile for diffusion through a type III ring at 600 K is now highly asymmetrical, with a reduction of the free energy barrier of around 20 kJ.mol$^{-1}$ on the right hand side.

### III.4. Presence of a hydrocarbon pool species

In the MTO process, the hydrocarbon pool (HP) species grow by repeated methylation. Light olefins are subsequently eliminated, regenerating the hydrocarbon pool species and closing the catalytic cycle [8]. To assess the influence of the presence of the HP species on diffusion of the product species, a metadynamics simulation at 600 K is performed during which an ethylene molecule is pulled through a type III eight-ring with a hexamethylbenzene (HMB) molecule one of the two cages.

Clearly, the presence of the HMB molecule has a large effect on the free energy landscape in the cage. As there is no longer a stable minimum along the $\xi$-axis, it can safely be concluded that the driving force for diffusion is now oriented out of this cage (Figure 6). Therefore, after the ethylene molecule is eliminated from the HP species, it is likely that its first hop out of the cage will be much faster than all the subsequent hops. Additionally, the ethylene molecule is less likely to hop into a cage that contains a large HP species as

the free energy barrier is now higher. This leads to the interpretation of so-called blocked sites that the ethylene molecules will try to avoid on their way out of the crystal. This effect will likely be even more pronounced for the larger propylene molecules. As the concentration of these blocked sites in the material rises, less unobstructed paths out of the crystal will be available, and the macroscopic transport diffusion coefficient of the crystal will decline.

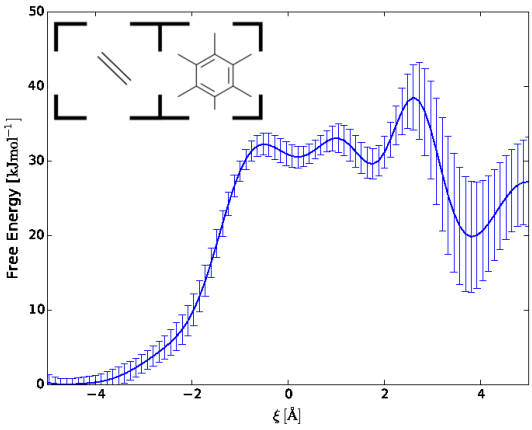


**Figure 6:** Free energy barrier for diffusion of ethylene through a type III ring at 600 K. A HP molecule is present in the right cage.

### III.5. Recovering kinetic information

So far, no kinetic information about the diffusion of the product species in the MTO process has been calculated. Simulations with a fixed bias have been performed that accelerate the sampling of rare events by pushing the system out of the free energy wells. Using transition state theory, it is possible to link the time scales of the biased and the unbiased systems. During this process, it is essential that no bias is deposited in the transition region around the top of the barrier.

Figure 7 shows an Arrhenius plot for the diffusion coefficient through a type I ring. These diffusion coefficients are on the order of $10^{-12}$ $\frac{m^2}{s}$, which is about two orders of magnitude smaller than the diffusion coefficients for ethylene reported in Ref. [6], which is in line with the expectations.

Although these diffusion coefficients satisfy the Arrhenius relation reasonably well, in the sense that they lie relatively close to the fitted line, this result should be interpreted with caution. After all, diffusion coefficients are macroscopic properties whereas here, only crossings through one particular ring have been studied. The diffusion coefficient obtained here is likely a better measure of the 'rate' of the specific ring under investigation, in which 'rate' is correlated with the number of expected ring crossings.

Extending the methodology used here to three-dimensional systems is an interesting line of future research.

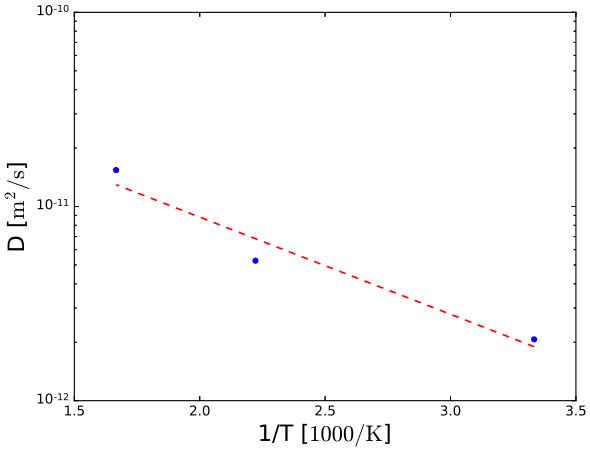


**Figure 7:** Arrhenius plot for the diffusion coefficient of propylene through a type I ring. The blue dots are the values obtained from the simulations. The dashed red line is a linear fit. The activation energy was found to be approximately 10 kJ.mol$^{-1}$.

### III.6. Resulting picture of diffusion

From a broader point of view, the goal of this research is to work towards a deeper understanding of the global picture of diffusion of the product species of the MTO process in H-SAPO-34. Figure 8 combines several of the insights gathered in this work into a single, hypothetical overview picture.

In the top left corner of Figure 8, a propylene molecule is eliminated from a HP molecule, this elimination is catalyzed by a Brønsted acid site and is represented by a purple star. The first diffusion step of the molecule is likely to be a fast one and has been accordingly labelled 'fast'. The molecule then continues its path through the molecule via several slower steps (labelled 'slow'), the rate of which will depend on the process temperature. This is supported by the fact that the diffusion coefficient for hopping through a ring satisfies an Arrhenius relation.

As the propylene molecule progresses on its path out of the material, it might come across a blocked site and accidentally jump in. However, the molecule is not expected to stay long and will likely jump right back. As the concentration of these blocked sites increases, the overall diffusion coefficient of olefins in the material is expected to decrease.

Similar considerations apply when the molecule hops

into a cage that happens to contain extra spectator molecules. In Figure 8, the jump out of such a cage is also labelled 'fast'. As diffusion out of cages that contain extra spectator molecules is faster than diffusion into these cages, asymmetrical situations in which a cage houses more molecules than its neighbouring cages are probably rare.

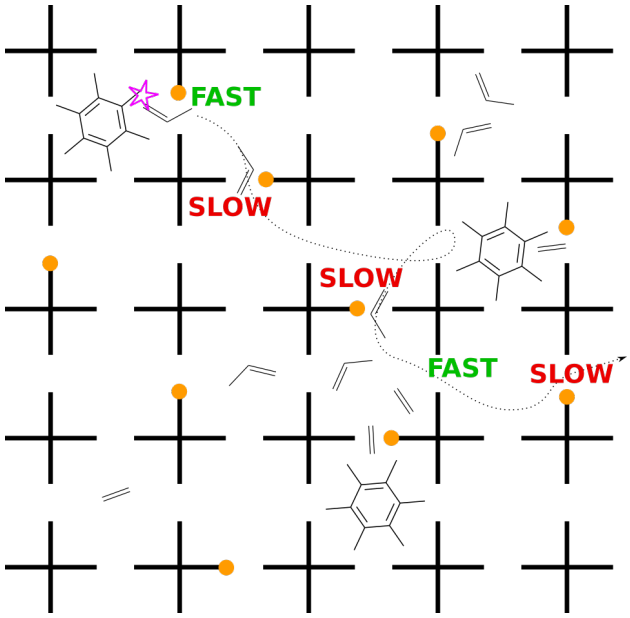


**Figure 8:** An overview of the diffusion process of light olefins in H-SAPO-34. The purple star represents the elimination of a propylene molecule from a HP molecule. Acid sites are represented by orange dots. Diffusion events have been labelled 'fast' or 'slow' based on the height of the free energy barrier for diffusion.

## IV. Conclusions

In this work, the validity and applicability of advanced molecular dynamics techniques based on force fields to study diffusion of propylene through the small eight-rings of H-SAPO-34 has been confirmed. This study is relevant in the context of the MTO process, where the diffusion of product species determines to a large extent the product selectivity and distribution.

The influence of the temperature on the free energy barrier for diffusion through various types of 8-rings in H-SAPO-34 was studied under relevant MTO process conditions. It has been found that the free energy barrier is dominated by the entropic contribution (-TS), which also explains the sharp raise of the diffusion barrier with temperature. Varying the number of acid sites in a single eight-ring did not significantly affect the free energy barrier.

The presence of extra spectator molecules or hydrocarbon pool species completely transforms the free energy surface. Propylene molecules are to leave cages in which other propylene molecules are present quickly. The same applies for cages in which a hydrocarbon pool species is present.

Next, an attempt has been made to recover kinetic information from simulations with a fixed bias. The obtained diffusion coefficients satisfy an Arrhenius relation.

This thesis was concluded by presenting a hypothetical global picture of diffusion of small olefins in H-SAPO-34.

## Acknowledgements

This work was performed at the Center for Molecular Modelling (CMM) under the supervision of prof. dr. ir. Veronique Van Speybroeck, prof. dr. ir. An Ghysels, dr. ir. Kristof De Wispelaere, and ir. Ruben Demuynck. I wish to thank them for their support and guidance. I would also like to thank the other members of the CMM for their support. The computational resources an services used were provded by Ghent University (Stevin Supercomputer Infrastructure).

## References

[1] S. Wilson and P. Barger, "The characteristics of SAPO-34 which influence the conversion of methanol to light olefins," *Microporous and Mesoporous Materials*, vol. 29, no. 1-2, pp. 117–126, 1999.

[2] B. P. Hereijgers, F. Bleken, M. H. Nilsen, S. Svelle, K.-P. Lillerud, M. Bjørgen, B. M. Weckhuysen, and U. Olsbye, "Product shape selectivity dominates the methanol-to-olefins (mto) reaction over h-sapo-34 catalysts," *Journal of catalysis*, vol. 264, no. 1, pp. 77–87, 2009.

[3] D. A. Woodcock, P. Lightfoot, L. A. Villaescusa, M.-J. Díaz-Cabañas, M. A. Camblor, and D. Engberg, "Negative thermal expansion in the siliceous zeolites chabazite and itq-4: A neutron powder diffraction study," *Chemistry of materials*, vol. 11, no. 9, pp. 2508–2514, 1999.

[4] J. Hutter, M. Iannuzzi, F. Schiffmann, and J. VandeVondele, "cp2k: atomistic simulations of condensed matter systems," *Wiley Interdisciplinary Reviews: Computational Molecular Science*, vol. 4, no. 1, pp. 15–25, 2014.

[5] W. Smith and T. Forester, "Dl_poly_2. 0: a general-purpose parallel molecular dynamics simulation package," *Journal of molecular graphics*, vol. 14, no. 3, pp. 136–141, 1996.

[6] A. Ghysels, S. Moors, K. Hemelsoet, and K. De Wispelaere, "Shape-selective diffusion of olefins in 8-ring solid acid microporous zeolites," 2015.

[7] G. Tribello, M. Bonomi, D. Branduardi, C. Camilloni, and G. Bussi, "Plumed 2: New feathers for an old bird," *Computer Physics Communications*, vol. 185, no. 2, pp. 604–613, 2014.

[8] K. Hemelsoet, J. Van der Mynsbrugge, K. De Wispelaere, M. Waroquier, and V. Van Speybroeck, "Unraveling the reaction mechanisms governing methanol-to-olefins catalysis by theory and experiment," *ChemPhysChem*, vol. 14, no. 8, pp. 1526–1545, 2013.

# Contents

# List of abbreviations

| | |
|---|---|
| SAPO | silico-alumino-phosphate |
| MTO | methanol-to-olefins |
| MSD | mean squared displacement |
| DFT | density functional theory |
| HP | hydrocarbon pool |
| MD | molecular dynamics |
| CHA | chabazite |
| FES | free energy surface |
| TST | transition state theory |
| AWA | accessible window area |
| HMB | hexamethylbenzene |
| CV | collective variable |

# 1 Introduction

## 1.1 Catalysts

Today, catalysts play a central role in the chemical industries. Over 90% of all products emerging from the chemical industries are in some way produced utilizing these materials. [1] Some of the most well-known applications are the refining of crude oil to produce high-quality fuels, the production of ammonia, all kinds of plastics, and also the production of pharmaceuticals [2].

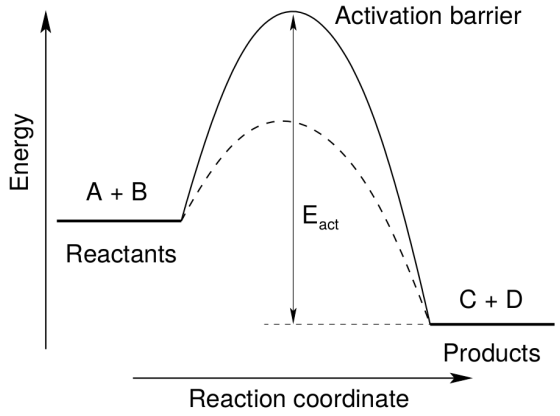


**Figure 1.1:** The principle of catalysis: the height of the activation barrier for the conversion from reactant to product is lowered by the catalyst. Full line: original activation barrier without catalyst. Dashed line: lowered activation barrier with catalyst. Figure taken from Ref. [2].

The principle of catalysis was first explained by Friedrich Ostwald, who received a Nobel Prize in Chemistry in 1909 for his work on catalysis, chemical equilibria, and reaction velocities [3]. Figure 1.1 schematically depicts how an energy barrier needs to be overcome when converting a reactant into a product. This energy barrier originates from the fact that

certain changes need to be made to the molecules, such as breaking bonds between atoms or bending parts of the molecules. In general, the function of a catalyst is to provide an alternative pathway from reactant to product with a lower activation barrier, thus requiring less energy. During the conversion from reactants to products, the catalyst itself is not consumed and, in most cases, the equilibrium between the reactants and the products does not shift, as the energy levels which the reactants and products occupy remain unchanged.

Catalysts can be classified into homogeneous and heterogeneous catalysts, depending on whether the catalyst particles are in the same phase as the reactants or not. Many examples of processes that are catalyzed by homogeneous catalysts can be found in the human body; in this context the catalysts are called enzymes. Metal surfaces, for example platinum or palladium, are used as heterogeneous catalysts. Another class of materials that is often used in heterogeneous catalysis applications are zeolites.

## 1.2 Zeolites

Zeolites are a class of nanoporous crystalline materials. They were first classified in 1756 by the Swedisch mineralogist Axel Fredrik Cronstedt (*1722 - †1765) who discovered that, upon rapid heating, the material stilbite produced large amounts of steam from adsorbed water molecules. He therefore called the material a zeolite, from the Greek zeo, meaning "to boil" and lithos meaning "stone". Since then, over 200 unique zeolite structures have been identified, 40 of which occur in nature. Strictly speaking, the term "zeolite" is reserved only for aluminosilicate materials; here it will be used as a catch-all for zeotype materials.

Nowadays, zeolite chemistry has established itself as a key area in the evolution of materials science. [4] Zeolites are produced synthetically on an industrial scale, with a world production that is estimated to be in the range of 2.7 million to 3.2 million metric tons in 2014. [5, 6] They consist of a periodic framework made of nanoporous channels and cages, resulting in a large surface area and high porosity. Their unique chemical and structural properties make zeolites fit for use in a broad range of industrial applications such as catalysis, gas separation, and ion exchange. [7] The industrial relevance of zeolites provides a powerful incentive to research the optimization of existing zeolite structures and to investigate new zeotype materials with valuable functionalities.

### 1.2.1 Structure

A zeolite framework is uniquely characterized by its pore topology and its chemical composition. Zeolite frameworks are made from interlinked tetrahedrals, mostly of silica ($SiO_4$) and alumina ($AlO_4$) but sometimes also phosphate ($PO_4$). Each tetrahedral (T) vertex is surrounded by four oxygen positions, and each oxygen atom is chemically bonded to two atoms (Si, Al, P) in T sites. [8] These primary units in turn form so-called secondary building blocks (such as 4- ,5- ,6- or 8-rings) which can form a broad variety of channels or cages. These channels and cages are at the basis of the periodic network of pores in zeolite frameworks (see Figure 1.2). Zeolite structures are well known from many crystallographic studies and easily accessible from reference material such as Meier and Olson's Atlas of Zeolite Structure Types [9] or online material such as the IZA database [10].

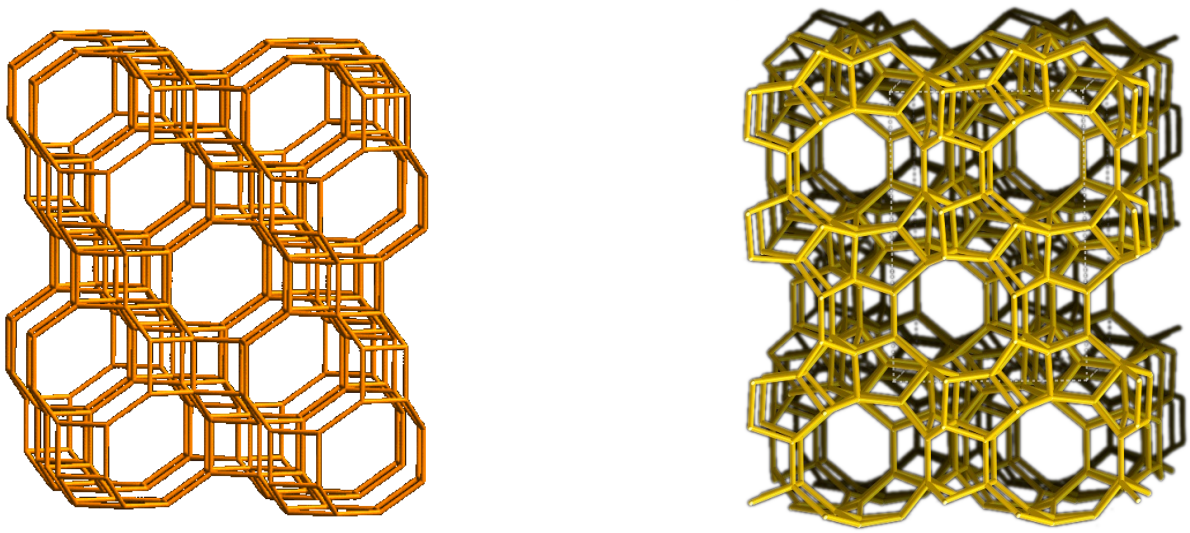

**(a)** **(b)**

**Figure 1.2:** Examples of different zeolite framework topologies: (a) CHA (chabazite) topology, (b) MFI topology. Figures adapted from the IZA database [10]

### 1.2.2 Zeolites in catalysis

The feature that makes zeolites so suitable for catalytic applications is the fact that substitutional defects can be introduced in the framework, for example Al atoms replacing Si atoms in zeolites or Si atoms replacing P atoms in zeotype materials. Because of the different valency of these defects, effective negative charges are introduced in the framework.

Such negative charges then have to be compensated by e.g. protons, which form Brønsted acid sites. In essence, the Brønsted acid sites behave in the same way as protons in an acidic solution. However, the benefit of using zeolites as catalysts lies in their specific structure of pores and cages, which can greatly enhance the reaction selectivity (i.e. the ratio of the desired product and the total amount of converted reactants), because not all products can easily be formed. The pores and cages of zeolite materials can also host other catalytic materials such as platinum, iron, or nickel to create catalysts with a high surface area that unite several catalytic functions into one particle.

Without a doubt, the most important application of zeolites in catalysis is the refining of large and complex hydrocarbon molecules originating from crude oil into smaller molecules that are of more economic value such as gasoline, diesel fuel, kerosine, and other byproducts of petroleum. This refining process involves various reactions among which catalytic cracking is the most important, with a worldwide production of around 15 million barrels per day of gasoline and light olefins [11].

However, oil reserves are depleting and the demand for base chemicals is rapidly increasing [12, 13]. With the *methanol to olefins* proces, one can produce base chemicals such as ethylene and propylene out of non-oil sources such as natural gas, coal or biomass. Because of its potential technological and economic value as an alternative to the oil-based route, the *methanol to olefin process* (MTO process) has been a popular research topic over the past decades. [14] It was accidentally discovered by two teams of Mobil scientists in 1977, using the zeolite H-ZSM-5 (MFI topology) as a catalyst. [15] 50 years after the Fischer-Tropsch process, the MTO process was the first major breakthrough in synthetic fuels and it has now been commercialized on an industrial scale around the world. [16, 17]

### Catalytic cycle

The reactants are converted into products via a catalytic cycle that comprises a sequence of steps, an example is depicted in Figure 1.3. In zeolites, the catalytically active sites are not directly accessible to the reacting molecules due to the special structure of pores and cages. First, the molecules have to diffuse through the structure towards the reactive sites inside the pores, where they can be adsorbed at the active site so that the conversion into products can readily take place. To close the catalytic cycle, the reactive sites must be cleared in order to catalyze the next reaction, which happens by desorption followed by diffusion. The products have to be transported back out of the zeolite crystal and out of the reactor by a diffusion process. Because reactions take place only when the reactants can make it to the

active sites, or when the products can leave the active site, diffusion plays a central role in the properties of zeolite catalysts. Over time, zeolite catalysts gradually lose their catalytic functions, for example due to the clogging of the cages by large hydrocarbon molecules. Although this catalyst deactivation is inevitable, some of its most severe consequences can often be deferred, or even reversed [18].

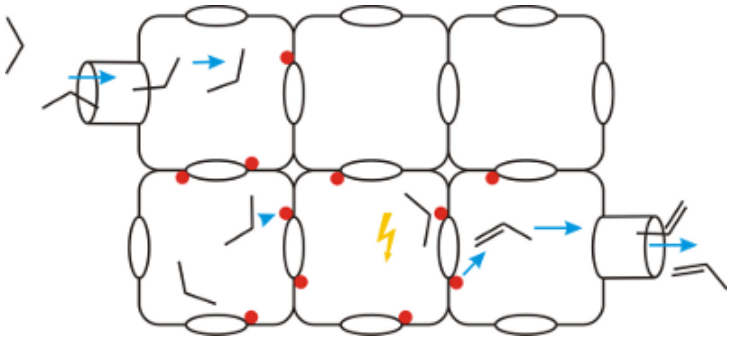

**Figure 1.3:** Schematic depiction of the catalytic cycle for the MTO process (vide infra). The blue arrows indicate the path of the molecules through the zeolite framework. Methanol molecules enter the framework on the left. They diffuse through the framework until they adsorb at an active site (indicated in red), where the conversion (represented by the yellow lightning symbol) of methanol molecules into propylene molecules takes place via a complicated mechanism. The formed propylene molecules are then evacuated out of the framework by diffusion.

### Reaction mechanism of the MTO process

The mechanism governing the MTO process has long been a controversial topic in the field of heterogeneous catalysis. A lot of reactions occur both in a consecutive and/or competing fashion, which makes the overall process very complicated. Obtaining more insight into the exact mechanism enables the design of the MTO process at the molecular scale. Although olefin formation was initially thought to occur through a direct mechanism, this hypothesis could not be reconciled with the experimental observation of a so-called induction period (a delay between the start of the process and the first olefins showing up in the reactor effluent). [17, 19] Also, a rigourous DFT-based study on a large number of suggested direct reaction mechanisms has shown that every imaginable direct pathway features at least one highly activated reaction step or unstable intermediate and no viable direct route from methanol to ethene or propene could be identified [20]. Based on the evidence mentioned here, the hypothesis of a direct mechanism has nowadays been rejected.

In the early 1990's an indirect mechanism was proposed by Dahl and Kolboe who suggested that hydrocarbons present in the zeolite pores act as co-catalysts for the MTO conversion; this is the hydrocarbon pool mechanism [21–23]. The hydrocarbon pool (HP) species grow by repeated methylation; light olefins are subsequently eliminated, regenerating the HP molecules and closing the catalytic cycle. Both the zeolite framework and the HP species play a central part in the MTO process. This inspired Haw et al. to propose the concept of a supramolecular catalyst which has properties dependent on both the zeolite (topology, chemical composition, Brønsted acid sites) and the nature of the HP species inside the pores of the MTO catalysts. [24] There is a lot of ongoing research on the exact chemical nature of the HP species, although the importance of cyclic carbenium ions and heavily methylated benzenes such as hexamethylbenzene (HMB) as organic reaction centres has been established for H-SAPO-34. [24–27] The formation of the HP is also a matter of scientific dispute. First, direct C-C coupling was thought to play an important role during the induction period. However, Song et al. have shown that direct C-C coupling might never take place and suggested that the HP grows from reactions with the carbonaceous impurities present in methanol feeds or in zeolite crystals. [28] This observation was contradicted by Jiang et al., whose experiments demonstrated that the organic impurities present in methanol streams do not influence the formation of the primary hydrocarbons. [29] For H-ZSM-5, a theoretically plausible route has been proposed for a ship-in-a-bottle formation of cyclic HP compounds inside the H-ZSM-5 framework, starting from methanol and small hydrocarbon fragments [30].

Identifying the actual catalytic cycles leading to the formation of olefins from methanol is challenging, even with the HP mechanism as a starting point. The issue is further complicated by the experimental observation that different topology and different chemical composition give rise to different product selectivities. Several experimental studies have already demonstrated the crucial role of diffusion in understanding the product distribution. [31–35] Although relatively large molecules can fit the spacious cages of H-SAPO-34, these cannot diffuse through the small 8-ring windows connecting the cages. Hence the product spectrum of H-SAPO-34 is primarily composed of smaller hydrocarbons such as propylene and ethylene. By contrast, H-ZSM-5 features larger 10-ring channels allowing for migration of bulkier hydrocarbons such as methyl benzenes with up to four methyl groups.

Over time, the HP species present in the zeolite pores can transform into larger compounds (coke species), blocking pores or poisoning acid sites and hence leading to catalyst deactivation. Experimental evidence suggests that, much like the composition of the product

stream, coke formation also depends on both catalyst topology and acidity. The influence of topology can be determined by comparing H-SAPO-34 with H-ZSM-5. In H-SAPO-34, large polyaromatics that are trapped in the pores are the culprit for deactivation whereas in the case of H-ZSM-5, the deactivation is due to the growth of large aromatic species at the channel crossings. With deactivation, there is a change in product selectivity from propylene to ethylene. This might be linked with the observation that there is a decrease of the mean number of methyl groups per aromatic ring with deactivation. However, according to Hereijgers et al. the reaction effluent is dominated by the product-state selectivity in case of deactivated H-SAPO-34. [31] A detailed reaction mechanism for coke formation is still a topic of ongoing research.

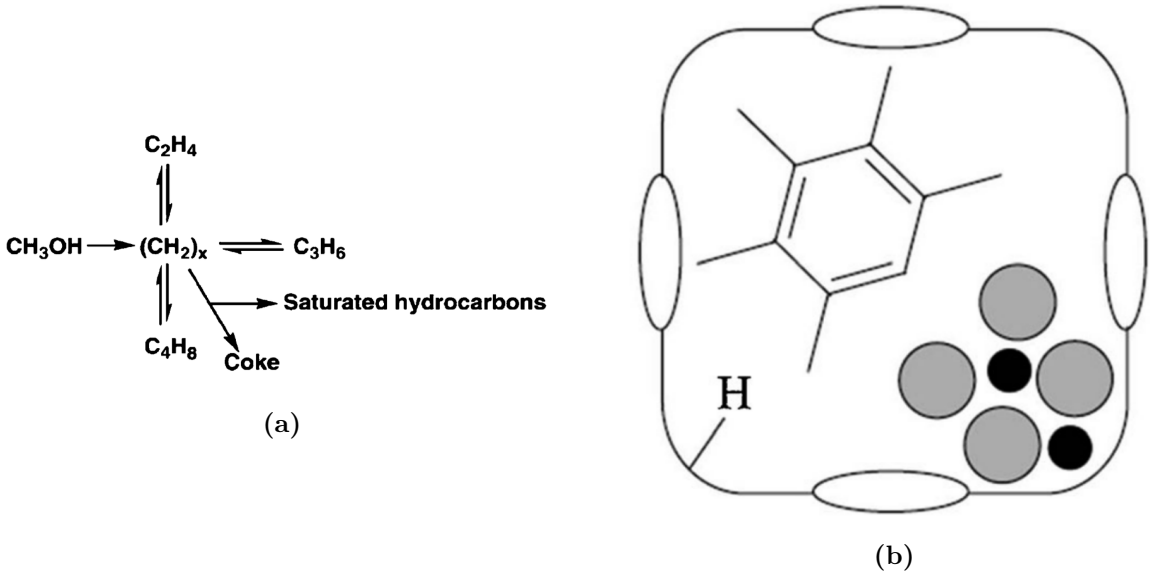


**Figure 1.4:** (a) Schematic representation of indirect HP reaction mechanism. [36] Copyright 1993 Springer (b) Visual representation of concept of supramolecular zeolite catalysis. Four key features are indicates: topology, acid function, organic compound, inorganic compound. [24] Copyright 2005 Springer

## 1.3 Objective

It has generally been acknowledged that, for the MTO process, diffusion of the product species through small-pore zeolites determines to a large extent the product selectivity and distribution. Various experimental evidences support this view. Despite this, theoretical diffusion studies for ethylene and propylene in small-pore zeolites are scarce. This is

especially true for the study of diffusion of propylene as diffusion itself becomes a rare event and special sampling techniques are necessary to obtain free energies of diffusion and diffusion coefficients [37]. This is precisely the aim of the current master thesis, to explore the validity and applicability of advanced molecular dynamics techniques based on force fields to study the diffusion of propylene through the small eight-rings of H-SAPO-34, one of the most promising and industrially relevant catalysts for the MTO process [38–40].

## 1.4 Outline

The relevance of diffusion through small-pore zeolites had been established in this introduction. Chapter 2 starts with a concise overview of the foundations of diffusion theory before dealing with the specifics of diffusion in zeolites. Also, an overview of literature data about diffusivities and diffusion barriers is presented with the aim of providing a good reference for the results chapter. Before discussing molecular dynamics simulations and advanced free energy techniques in chapter 4, chapter 3 first repeats some fundamental concepts from statistical mechanics. The computational and methodological details are described in chapter 5, before discussing the results in depth in chapter 6. This thesis ends with chapter 7, that gives a brief overview of the obtained results and succinctly summarizes the conclusions that can be rawn.

# 2 Diffusion

Diffusion is the migration of small particles or molecules due to thermal motion. In layman's terms, diffusion is most easily explained as a spontaneous tendency of all systems to equalize concentration over space. From a more fundamental viewpoint, this tendency can be understood as a manifestation of the second law of thermodynamics which tells us nature is always trying to maximize entropy.

Diffusion is important in almost all applications of zeolites since it is crucial in catalysis and gas separation processes. In the context of the MTO process, understanding diffusion can help us get a grip on the product selectivity and the product distribution.

This chapter first discusses the foundations of diffusion theory before dealing with the particularities of diffusion in zeolites.

## 2.1 Fick's laws

Diffusion was first quantitatively described in the work of Adolf Fick published in 1855. A measure for diffusion is the material flux, defined as the number of molecules passing through a given surface area per unit time. The observation that these fluxes disappear in the absence of a concentration gradient inspired Fick's first law which postulates a linear relation between the flux, $\boldsymbol{J}$, and the concentration gradient, $\boldsymbol{\nabla} C$.

$$\boldsymbol{J} = -D^t \boldsymbol{\nabla} C \tag{2.1}$$

The proportionality constant $D^t$ is called the Fickean diffusion coefficient (also known as transport diffusion coefficient or transport diffusivity), and it can be interpreted as a measure of how sensitive the system is to a concentration gradient. The units of the parameters defined above are: $D^t$ [length$^2$/time], $C$ [molecules/volume], and $J$ [molecules/area $\cdot$ time].

The flux, and hence the diffusion coefficient, must be chosen relative to some frame of reference.

On a more fundamental level, the driving force for diffusion is a gradient of the chemical potential, $\mu$. Particles always move to positions where the chemical potential is lowest to lower the total free energy of the system. Using irreversible thermodynamics, an alternative form of Fick's first law can be derived: [41]

$$\boldsymbol{J} = -L\boldsymbol{\nabla}\mu, \tag{2.2}$$

where $L$ is the single component phenomenological Onsager coefficient. In literature, this equation is also known as the Onsager relation.

Fick's first law can be combined with the law of conservation of mass

$$\frac{\partial C}{\partial t} = -\boldsymbol{\nabla} \cdot \boldsymbol{J}. \tag{2.3}$$

When one assumes $D^t$ is independent of $C$ and homogeneous, substitution of equation 2.1 into equation 2.3 gives Fick's second law, which describes how diffusion causes the concentration to change over time:

$$\frac{\partial C}{\partial t} = D^t \boldsymbol{\nabla}^2 C. \tag{2.4}$$

## 2.2 Transport diffusion versus self-diffusion

So far, only transport diffusion, which results from a concentration (or chemical potential) gradient, has been discussed. It is important to understand that the concept of a concentration gradient is fundamentally macroscopic. Fick's first law and the transport diffusion coefficient $D^t$ are thus macroscopic.

The result of this transport diffusion process is a uniform distribution of the molecules, and in absence of a concentration gradient there is no more net mass transport. However, as soon as the equilibrium is established, the mechanism of self-diffusion takes over. Self-diffusion is the spontaneous mixing of molecules in absence of a concentration gradient due to the random motion of the molecules. Self diffusion is a microscopic phenomenon, and experimentally, it is usually measured by tracking isotopic tracer molecules or molecules that are otherwise labeled, which is why it is also known as tracer diffusion.

Defining a self-diffusion coefficient $D^s$ that is analogous to the transport diffusion coefficient $D^t$ is not trivial. To understand how this is done, the time evolution of the concentration profile of a tagged species is derived by solving equation 2.4, under the assumption that the tagged species is concentrated at the origin of a spherical coordinate frame $(r, \theta, \phi)$ at time t = 0. Mathematically, this translates to the boundary condition

$$C(\boldsymbol{r}, 0) = N_0 \delta(\boldsymbol{r}), \tag{2.5}$$

where $\delta(\boldsymbol{r})$ is a Dirac delta function and $N_0$ is the total number of labelled molecules. The Gaussian concentration profile $C(r, t)$ that is obtained gradually widens with time,

$$C(r, t) = \frac{N_0}{(4\pi D^t t)^{3/2}} \exp\left(-\frac{r^2}{4D^t t}\right). \tag{2.6}$$

The vector notation in $C(r, t)$ has been dropped as there is only a radial dependency. Using the fact that the total amount of particles remains constant over time

$$\int d\boldsymbol{r} C(r, t) = N_0, \tag{2.7}$$

it is possible to define the probability distribution $P(r, t) = C(r, t)/N_0$. The mean squared displacement $\langle r^2(t) \rangle$ is the second moment of $P(r, t)$:

$$\langle r^2(t) \rangle = \frac{1}{N_0} \int d\boldsymbol{r} r^2 C(r, t). \tag{2.8}$$

Multiplying equation 2.4 by $r^2$ and integrating over all of space yields:

$$\frac{\partial}{\partial t} \int d\boldsymbol{r} r^2 C(r, t) = D^t \int d\boldsymbol{r} r^2 \nabla^2 C(r, t). \tag{2.9}$$

The left hand side of the previous equation is by definition equal to

$$N_0 \frac{\partial \langle r^2(t) \rangle}{\partial t}, \tag{2.10}$$

so that, after applying partial integration, a relation between the transport diffusion coefficient $D^t$ and the width of the concentration profile is finally obtained.

$$\begin{aligned} \frac{\partial \langle r^2(t) \rangle}{\partial t} &= D^t \int d\boldsymbol{r} r^2 \nabla^2 C(r, t) \\ &= 6D^t, \end{aligned} \tag{2.11}$$

By integration the equation above, an equivalent relation is obtained:

$$MSD(t) = \langle r^2(t) \rangle = 6D^t t. \tag{2.12}$$

Equation 2.12, which was first derived by Einstein, establishes a relation between the width of the concentration profile and the diffusion coefficient. Although the this relation is derived from a macroscopic law, it ties the diffusion coefficient (which is a macroscopic quantity) to the mean squared displacement (which is a microscopic quantity). In the case of self-diffusion, although no macroscopic concentration gradient is present and the only relevant quantity characterizing the diffusion process is the MSD, a self-diffusion coefficient $D^s$ can still be defined via the equation 2.12. Transport diffusion and self-diffusion, the transport diffusion coefficient and the self-diffusion coefficient are generally different. In the limit of infinite dilution, the physics of transport diffusion and of self-diffusion will become equivalent.

Equation 2.12 also provides a way of measuring $D^s$ in a computer simulation. The mean squared displacement of the labelled particles can simply be calculated as

$$\langle \Delta r(t)^2 \rangle = \frac{1}{N} \sum_{i}^{N} \Delta r_i(t)^2, \tag{2.13}$$

where N is the total amount of particles and $\Delta r_i(t)$ is the distance traveled by particle $i$ in time $t$. Alternatively, a self-diffusion coefficient can be defined through the Green-Kubo relations, which relate the velocity autocorrelation to the self-diffusivity: [42]

$$D^s = \frac{1}{3} \int_0^\infty \langle \boldsymbol{v}(0) \cdot \boldsymbol{v}(t) \rangle dt. \tag{2.14}$$

Time-correlation functions, such as the velocity autocorrelation function in the Green-Kubo relation for the diffusion coefficient, are easy to measure in molecular dynamics simulations. For classical systems, equations 2.12 and 2.14 are strictly equivalent.

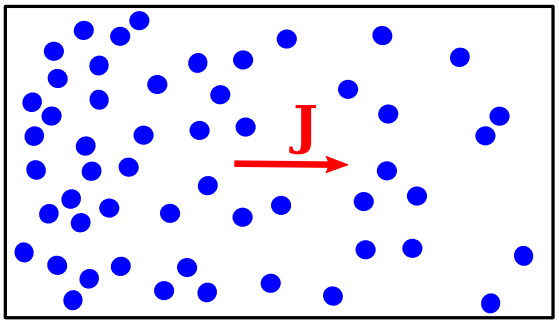


**Figure 2.1:** Transport diffusion

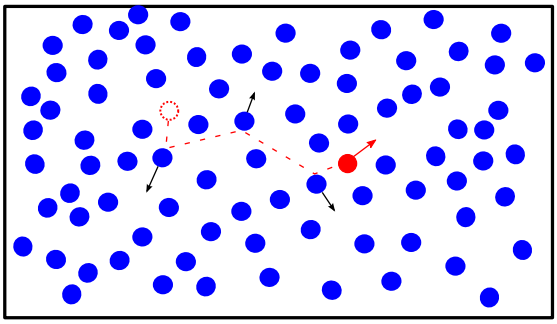

**Figure 2.2:** Self-diffusion

## 2.3 A molecular view on diffusion

In this work, a system will be studied in which a single propylene molecule diffuses between two chabazite cages connected by an 8-ring. Therefore, calculating the mean squared displacement is not a good strategy to fit a diffusion coefficient. It has been established that propylene diffuses between cages by an activated jump process [37]. On average, the molecules spend a certain waiting time $\tau$ in a cage before crossing a ring to a adjacent cage. Here, a relation between this average waiting time $\tau$ and the diffusion coefficient is derived, starting from a random walk. This relation is then used in section 6.5 to make an estimate of the diffusion coefficient.

On a molecular level, the image we have of diffusion is that of molecules executing a random walk: a molecule has a certain probability $P\Delta\tau$ to jump to a new position in a time interval $\Delta\tau$ and a probability $(1-P)\Delta\tau$ to stay put. Now suppose a molecule jumps $N_r + N_l = N$ times, where $N_r$ and $N_l$ denote the number of jumps to the right and to the left respectively. Denoting the average distance travelled in each jump by $\lambda$, the net travelled distance can be expressed as $(N_r - N_l)\lambda$. Writing the difference $N_r - N_l$ as $n$, the number of ways W to make precisely $N_r$ jumps to the right and $N_l$ jumps to the left is equal to:

$$W = \frac{N!}{N_r!N_l!} = \frac{N!}{\left[\frac{1}{2}(N+n)\right]!\left[\frac{1}{2}(N-n)\right]!}. \tag{2.15}$$

Taking $N$ steps can be done in $2^N$ ways. The chance $P_N(n)$ that a molecule has traveled a distance $n \times \lambda$ after $N$ jumps is therefore given by:

$$P_N(n) = \frac{W}{2^N} = \frac{N!}{\left[\frac{1}{2}(N+n)\right]!\left[\frac{1}{2}(N-n)\right]!2^N}. \tag{2.16}$$

Applying Stirling's formula to rewrite $\ln x!$ we find:

$$\ln x! = \ln\sqrt{2\pi} + (x+\frac{1}{2})\ln x - x. \tag{2.17}$$

$\ln[P_N(n)]$ can now be reworked into:

$$\ln[P_N(n)] = \ln\left(\frac{2}{\pi N}\right)^{1/2} - \frac{1}{2}(N+n+1)\ln\left(1+\frac{n}{N}\right) - \frac{1}{2}(N-n+1)\ln\left(1-\frac{n}{N}\right). \tag{2.18}$$

For small net travelled distances ($n << N$), $\ln(1\pm n/N)$ can be replaced by $\pm n/N - (n/N)^2/2$ and the previous expression reduces to:

$$\ln[P_N(n)] = \ln\left(\frac{2}{\pi N}\right)^{1/2} - \frac{n^2}{2N}. \tag{2.19}$$

This probability of stepping a net amount of $n$ steps to the right after a total of $N$ jumps can easily be linked to the probability $P_N(x)$ of travelling a certain distance to the right via the simple relation:

$$x = n\lambda. \tag{2.20}$$

Because a molecule has a chance $P\Delta\tau$ to jump to a new position in a time interval $\Delta\tau$, the average waiting time for a jump $\tau$ is given by $1/P$. It therefore takes a molecule on average a time $t = N\tau$ to make N jumps. Using the aforementioned results, the probability $P(x,t)$ that a molecule travels a distance $x$ to the right in a time $t$ is given by a gaussian distribution:

$$P(x,t) = \left(\frac{2\tau}{\pi t}\right)^{1/2} \exp\left(-\frac{x^2\tau}{2t\lambda^2}\right). \tag{2.21}$$

Now consider the solution of Fick's second law (equation 2.4) for one dimensional diffusion from a point source:

$$C(x,t) = \frac{1}{\sqrt{4\pi Dt}} \exp\left(-\frac{x^2}{4Dt}\right). \tag{2.22}$$

When comparing equations 2.21 and 2.22, it becomes clear that both expressions describe the same process and that we have derived a macroscopically measurable diffusion characteristic starting from microscopic statistical assumptions. The similarity between both expressions allows for an alternative interpetation of the diffusion coefficient in terms of the average jump length and the average waiting time for a jump:

$$D = \frac{\lambda^2}{2\tau}. \tag{2.23}$$

From this equation it is clear that diffusion will be faster if the waiting time for a jump decreases and/or if the average distance travelled in one jump increases. This result can also be generalized from one to three dimensions. The caveat is that the particle can then jump in three directions, so that on average only one in three jumps will be in the $x$ direction. In other words, the waiting time for jumps in the $x$ directions triples so that $D$ becomes:

$$D = \frac{\lambda^2}{6\tau}. \tag{2.24}$$

## 2.4 Diffusion in nanoporous media

Most of the foundations of diffusion theory are based on gaseous and liquid diffusion. For these isotropic media, the calculation of relevant properties for diffusion, such as the mean free path or the collision rate, is straightforward. In porous media, the situation is more

complicated. For smaller (or larger) diameter pores, intermolecular interactions between the diffusion species and the host framework will play a larger (or smaller) role. Depending on the size of the pores, and therefore depending on the nature of the dominant interactions, the diffusion in porous materials has been classified into 3 different regimes (Figure 2.3). When the pore diameter is larger than the mean free path of the molecules, the collisions between the molecules are more frequent than those between the molecules and the pore surfaces [43]. This regime is called *gaseous* or *molecular* diffusion and a typical diffusion constant is $10^{-5}$ $m^2.s^{-1}$. As collisions between the molecules and pore walls become more frequent, either due to decreasing pore dimension or due to an increase of the mean free path, the behavior of the diffusing molecules changes. When the molecules collide more often with the wall than among themselves, they enter the *Knudsen* regime and they will flow almost independently from one another. [44] For pore sizes that are roughly the same size as the diffusing molecules, typically in the range of 2 nm or less, the molecules constantly experience the interaction with the pore surface. This regime is called *configurational* diffusion.

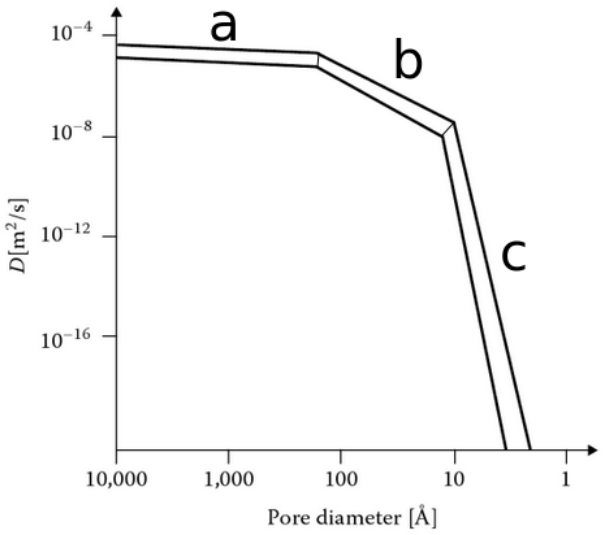


**Figure 2.3:** Relation between diffusivity and pore diameter. Three diffusion regimes can be distinguished. (a) molecular diffusion, (b) Knudsen diffusion, (c) configurational diffusion. Figure adapted from [45].

From the previous section, it is clear that diffusion in small-pore zeolites happens in the configurational regime because of the small pore sizes. This regime is characterized by high activation energies (in the range of $10 - 100$ $kJ.mol^{-1}$) and very low diffusivities (spanning many orders of magnitude, from $10^{-8}$ $m^2.s^{-1}$ to $10^{-20}$ $m^2.s^{-1}$). These diffusivities

and activation barriers strongly depend on the size and shape of guest molecules, the concentration of the guest molecules, temperature, and the chemistry and topology of the pores. As a result, it is challenging to develop general diffusion models that link the diffusion coefficients to all the properties mentioned above.

### 2.4.1 Concentration dependence

Diffusion of molecules in zeolites often takes place in channels where it is almost impossible for the molecules to pass each other. Therefore, the diffusion of guest molecules often displays a strong concentration dependence. A first attempt to model the concentration dependence of the diffusivity in zeolites was made by Barrer [46], who used a basic jump diffusion model. Introducing an elementary diffusion rate $D_0^s$ to jump from one site to another at infinite dilution, the diffusivity is proportional to the chance that a neighbouring site is empty:

$$D^s(\theta) = D_0^s \cdot (1 - \theta) \tag{2.25}$$

This equation assumes that the average occupancy of a site is equal to $\theta$, which is valid in the mean-field approximation.

In this thesis, the influence of the pore loading on the free energy barrier for diffusion through eight-rings of H-SAPO-34 is investigated, which might provide insight into the concentration dependence for the diffusion of the product species in the MTO process.

### 2.4.2 Temperature influence

The diffusion process in zeolites is usually modeled as an activated hopping process [47], the temperature dependence can thus be described by an Eyring equation: [48]

$$D(T) = D_0 \exp\left(-\frac{E_a}{k_B T}\right) \tag{2.26}$$

in which the pre-exponential term $D_0$ is the diffusivity at infinite temperature, and $E_a$ the activation energy of diffusion. $D_0$ can be interpreted as the rate at which particles attempt to hop to a neighbouring site, while the exponential expresses the probability that the molecules are able to overcome the activation energy barrier $E_a$ between these sites. In section 6.2 and 6.5 the influence of the temperature on the free energy barrier and on the diffusion coefficients is studied, respectively.

The attempt rate can be expressed as $D_0 = guL$, where $u$ is the velocity at which the molecules travel, $L$ is the average distance between collisions or jumps, and $g$ is a geometrical factor. The so-called gas translation model, in which the molecules inside the zeolite lattice retain their gaseous character despite the restricted movement from site to site, has been proposed [48] for diffusion in the configurational regime. According to the gas translation model, the diffusivity of a molecule from one site to one particular adjacent site inside an isotropic lattice with $z$ neighbouring sites is given by:

$$D = guL \exp\left(-\frac{E_a}{k_B T}\right) = \frac{1}{z}\sqrt{\frac{8k_B T}{\pi m}}\lambda \exp\left(-\frac{E_a}{k_B T}\right), \tag{2.27}$$

where $m$ is the molecular mass, $\lambda$ is the distance between two adjacent sites and the factor $1/z$ accounts for the possibility of the molecule moving to one of the other adjacent sites. Molecules that strongly interact with the zeolite are more or less bonded to the lattice, and lose their gaseous entity. They vibrate with their host lattice before accumulating enough free energy to jump to adjacent sites. An alternative model that deals with this kind of diffusion is the solid vibration model. [48] In this model, the molecules are assumed to vibrate harmonically around their energy minimum. The diffusion coefficient is then given by

$$D = guL \exp\left(-\frac{E_a}{k_B T}\right) = \frac{1}{z}\nu_e \lambda^2 \exp\left(-\frac{E_a}{k_B T}\right). \tag{2.28}$$

In this equation $\nu_e$ is the effective vibrational frequency of the molecule inside the zeolite. This frequency is of course related to the molecular mass $m$ and the harmonic force constant, which is simply the curvature of the potential well around the minimum.

Although this certainly is an oversimplified and overgeneralised picture of the true diffusion process, it is capable of accurately describing the temperature dependence because of its flexibility in incorporating a broad variety of assumptions with regard to the molecular motion, the interactions among the molecules, and the interactions of the molecules with the host framework.

## 2.5 Diffusion coefficients in literature

For diffusion coefficients of ethylene and propylene in materials with the CHA topology, there is a wealth of literature data available, that has been conveniently summarized by Ghysels *et al* [37]. Part of this summary is repeated here, albeit with a special focus on the data for propylene molecules. Using the the BKS force field [49], Wang *et al.* reported [50]

diffusion coefficients for propene ranging from $3.0 \times 10^{-11}$m$^2$/s at 673 K to 7.8 $\times 10^{-11}$m$^2$/s at 873 K for 3 ns trajectories and between $2.4 \times 10^{-11}$ m$^2$/s and $7.2 \times 10^{-11}$ m$^2$/s for 18 ns trajectories. The diffusion activation barrier was found to be more than 20 kJ.mol$^{-1}$, heavily restricting the diffusion of propene through the CHA catalyst. By contrast, the diffusion coefficient for the smaller ethylene molecules was found to be about 20 times higher. Combariza simulated the diffusion of propylene and propane in pure Si-CHA materials using the PMM [51] and BKS force fields [52]. For propylene, the diffusivities ranged from $5.2 \times 10^{-11}$ m$^2$/s at 300 K to $1.6 \times 10^{-10}$ m$^2$/s at 800 K using the BKS force field and ranged from $2.41 \times 10^{-11}$ m$^2$/s at 300 K to $2.75 \times 10^{-10}$ m$^2$/s at 800 K using the PMM force field. Sastre studied the diffusion or propane in acidic zeotypes AFX and AEI and found diffusivities on the order of $10^{-12}$ m$^2$/s [53].

The experimental diffusivities lie more spread out. Hedin et al. carried out PFG NMR experiments with pure Si-CHA (SSZ-13) at 301K and 1 bar, which corresponds to 1.4 ethene molecules per cage, and found a diffusivity of $3.1 \times 10^{-12}$ m$^2$/s for ethene [54]. The propylene diffusivity was below the detectable limits of the apparatus. Olsen *et al.* observed a propene diffusivity of $1.1 \times 10^{-13}$ m$^2$/s in pure Si-CHA at 353K, the diffusion activation barrier was found to be 10 kJ.mol$^{-1}$ from an adsorption experiment [55]. A similar adsorption experiment performed by Ruthven and Reyes was used to derive the diffusion coefficients of propene in SAPO-34. A propene diffusivity of $9 \times 10^{-14}$ m$^2$/s and an activation barrier of 97 kJ.mol$^{-1}$ were found. [56] Dai et al. also experimentally investigated the SAPO-34 material and reported ethylene diffusivities between $1.1 \times 10^{-11}$ m$^2$/s and $1.3 \times 10^{-11}$ m$^2$/s [34]. The narrow 8-rings of the CHA structure restricted diffusion of propylene to such an extent that the diffusivities were not measurable [34].

Both computational and experimental results in literature confirm that diffusion in small-pore zeolites happens in the configurational regime. Especially for propylene molecules, the activation barrier for diffusion becomes so high that jumps become a rare event on the time-scale of a classical molecular dynamics simulation and it becomes impossible to obtain meaningful diffusion information. To mitigate this problem, enhanced sampling techniques are required. This thesis starts with an in-depth investigation of the free energy barrier for diffusion or propylene in H-SAPO-34, a zeotype material with CHA topology.

# 3 Statistical Mechanics

This chapter presents a brief review of the theory of statistical physics with special emphasis on the issues that are relevant to computer simulations.

## 3.1 Basic theory

Statistical mechanics studies systems with many (or infinitely many) degrees of freedom. According to classical physics, these degrees of freedom are the positions and momenta of particles; sometimes magnetic moments ('spins') are also included. The space spanned by these degrees of freedom is called *phase space*. Points in phase space represent a particular configuration of the system. As time goes by, a system follows a path in phase space which is governed by the equations of motion. The values of all the degrees of freedom as a function of time are meaningless as only time averages of physical quantities are measurable. This is because any physical measuring device (e.g. thermometer, barometer) has a relatively slow response time, hence it measures a time average. However, even if it was possible to instantaneously measure some quantity of interest, for ergodic systems (vide infra) the result would still be very close the the time average of that quantity by virtue of the law of large numbers. The law of large numbers states that if a quantity is composed of $N$ uncorrelated contributions, fluctuations in that quantity are of the order of $\frac{1}{\sqrt{N}}$. For macroscopic quantities this means that the fluctuations are extremely small.

Because only a restricted amount of data can be stored in computer memory, computer simulations are limited to sampling relatively few degrees of freedom and system sizes in simulations are usually much smaller than those in experimental systems. Additionally, a time average of a physcial quantity is given by

$$\bar{A} = \lim_{T \to +\infty} \frac{1}{T} \int_0^T A(T) dt, \tag{3.1}$$

although the results must be obtained in a finite amount of time. In molecular dynamics simulations (see Chapter 4), the typical simulation time is of the order of $10^{-9} - 10^{-6}$ seconds, which is far below the response time of most physical measuring devices. This means that the results of these simulations is only meaningful when two conditions are met: (1) the spatial correlations extend over ranges smaller than the system size and (2) the correlation time of the system is much smaller than the simulation time.

## 3.2 Ensembles and the ergodic hypothesis

Systems that are not thermally and mechanically insulated will eventually take on the temperature and pressure of their surroundings. These physical quantities, that are controlled externally, are examples of *system parameters*. Different experimental circumstances correspond to different sets of system parameters that can be manipulated. In statistical physics, an alternative way to calculate averages is to do an *ensemble* average. An ensemble is a set of many mental copies of the system that all have the same system parameters. The assumption that the ensemble average is equivalent to the time average is called the *ergodic hypothesis*.

### 3.2.1 NVE-ensemble

The fundamental postulate of statistical mechanics says that all states accessible to a system with a fixed number of particles, volume, and energy are equally likely to be visited . It is also known as the postulate of *equal a priori probabilities*. Together with the ergodic hypothesis, it leads to the identification of the time average $\bar{A}$ of a physical quantity $A$ with the uniform average over all accessible states $\langle A \rangle$. For quantum systems, the ensemble average is calculated as follows:

$$\langle A \rangle = \frac{\sum_X A(X)\delta[\mathcal{H}(X) - E]}{\sum_X \delta[\mathcal{H}(X) - E]} = \bar{A}, \tag{3.2}$$

where $X$ denotes a quantum state of the system (a point in phase space), and $\mathcal{H}(X)$ is the Hamiltonian which gives the energy eigenvalue of state $X$. In case of classical systems with continuous degrees of freedom, the sums are replaced by integrals over the positions $\boldsymbol{r_i}$ and momenta $\boldsymbol{p_i}$ of the particles:

$$\sum_X \to \left(\frac{1}{h}\right)^{3N} \int d\boldsymbol{r_1} d\boldsymbol{r_2} \ldots d\boldsymbol{r_N} \int d\boldsymbol{p_1} d\boldsymbol{p_2} \ldots d\boldsymbol{p_N}, \tag{3.3}$$

Where $h$ is Planck's constant and the factor $\left(\frac{1}{h}\right)^{3N}$ accounts for the volume of a state in phase space, according to the uncertainty principle of Heisenberg. The denominator of equation 3.2 counts the number of states with prescribed number of particles, volume, and energy. This number is known as the thermodynamic probability and it is denoted by $\Omega$:

$$\Omega(N, V, E) = \sum_X \delta[\mathcal{H}(X) - E]. \tag{3.4}$$

The *entropy* is defined as a function of $\Omega(N, V, E)$ as

$$S(N, V, E) = k_B \ln \Omega(N, V, E). \tag{3.5}$$

This leads to the interpretation of the entropy as an additive measure of the number of accessible states to the system. Suppose there are two independent but otherwise identical systems instead of one, the number of accessible states will now be $\Omega^2$ but the entropy will simply be 2S.

### 3.2.2 NVT-ensemble

In experimental situations, it is often the case that the temperature is controlled instead of the energy. To achieve this, the system is coupled to a heat bath, a very large reservoir that can exchange heat with the system without changing its own temperature. The time average for such a system is equal to a weighted average over states with fixed volume and particle number (the energy is no longer restricted); the weighting factor is the *Boltzmann factor*: $\exp[-\mathcal{H}(X)/(k_B T)]$. The notation $\beta = 1/(k_B T)$ is often used. The ensembe average is thus

$$\langle A \rangle_{NVT} = \frac{1}{Z} \sum_X A(X) \mathrm{e}^{-\beta \mathcal{H}(X)}, \tag{3.6}$$

where the factor Z ensures proper normalisation

$$Z(N, V, T) = \sum_X \mathrm{e}^{-\beta \mathcal{H}(X)}. \tag{3.7}$$

The factor Z is also called the canonical *partition function* and it is related to the free energy $F$:

$$F = -k_B T \ln Z(N, V, T) = E - TS. \tag{3.8}$$

For classical systems that are continuous the canonical partition function is equal to

$$Z = \left(\frac{1}{h}\right)^{3N} \int \int \mathrm{e}^{-\beta \mathcal{H}(X)} d\boldsymbol{r_1} d\boldsymbol{r_2} \ldots d\boldsymbol{r_N} d\boldsymbol{p_1} d\boldsymbol{p_2} \ldots d\boldsymbol{p_N} \tag{3.9}$$

Under the constraint of fixed volume, temperature, and particle number, the free energy of a system reaches its minimum when the system is in equilibrium. The NVT-ensemble is also known as the *canonical ensemble* and the average as calculated in equation 3.6 is known as the canonical ensemble average. The canonical partition function can be related to the thermodynamic weight $\Omega$ from the microcanonical ensemble as follows:

$$Z(N,V,T) = \sum_E \mathrm{e}^{-\beta E}\Omega(N,V,E), \tag{3.10}$$

where the sum runs over sets of states with fixed energy. A very interesting insight can be gained from this formula. As the temperature increases, an increasing amount of phase space will become accessible to the system. This is determined by the dimensionless factor $-\beta E$, as the temperature increases, the Boltzmann factor will become larger and hence the system can reach higher energies and thus more configurations. Also, the number of states $\Omega(N,V,E)$ is a rapidly increasing function of E whereas the Boltzmann factor is a rapidly decreasing function of E. The product of these two functions will thus be sharply peaked around some value $\bar{\mathrm{E}}$ and this implies that, most of the time, the system will have an energy that is very close to this value. This means that in practice, there will not be much difference between a canonical system and a microcanonical system in which the energy is kept fixed at $\bar{\mathrm{E}}$. This is an example of what is known as *ensemble equivalence*: the law of large numbers dictates that measurable physical quantities exhibit very small flucuations, essentially fixing them to their average values. For finite systems, the differences between the ensembles increase with decreasing system size [57].

### 3.2.3 NPT-ensemble

Sometimes the pressure is controlled instead of the volume, for example in a cylinder closed by a movable piston. This ensemble is known as the *isothermal-isobaric* ensemble or NPT-ensemble. As is the case for the NVT-ensemble, the identification of the ensemble average with the time average can be made, but the weight factor is different:

$$\langle A\rangle_{NPT} = \frac{1}{Q}\int dV\ \mathrm{e}^{-\beta PV}\sum_X \mathrm{e}^{-\beta\mathcal{H}(X)}A(X), \tag{3.11}$$

$$Q(N,P,T) = \int dV\ \mathrm{e}^{-\beta PV}\sum_X \mathrm{e}^{-\beta\mathcal{H}(X)} = \int dV \mathrm{e}^{-\beta PV} Z(N,V,T). \tag{3.12}$$

$Q(N,P,T)$ is again called the partition function and it is related to the canonical partition function Z in the same way as Z is related to the function $\Omega$ in the microcanonical ensemble.

Q can also be related to the Gibbs free energy G:

$$G = -k_B T \ln Q(N, P, T) = E - TS + PV. \tag{3.13}$$

G is minimal when the system reaches equilibrium under the restrictions of fixed number of particles, fixed pressure, and fixed temperature.

# 4 Molecular Dynamics

Molecular Dynamics (MD) is a powerful computer simulation technique used to compute the equilibrium and transport properties of classical many-body systems. The MD method was invented by theoretical physicists Alder and Wainwright in the 1950's [58] and it has now had a profound impact on many fields, ranging from biology to materials science and from astrophysics to chemical kinetics.

In the chapter on statistical mechanics it has been established how the experimental values of physical quantities can be found as ensemble averages. However, experimental systems are usually so large that it is not practical to determine the ensemble average by summing over all the accessible states on a computer. Now imagine a random sample of $10^8$ configurations of the system which are all compatible with the values of the system parameters. For such a large sample, it is expected that the average of physical quantities over this sample is approximately equal to the ensemble average. Unfortunately, generating these large random samples is impossible. However, using MD methods, a sample can be generated that consists of a large number of configurations that are determined successively from each other and are hence correlated. This is done in a smart way such that the ensembles are sampled correctly.

In MD, the first step is the initialization of the system. The second step is to determine the forces on all the particles in the system, this is generally the most time-consuming step. The forces can be evaluated using a force field (in classical MD) or using quantum mechanical calculations (in *ab initio* MD). Newton's equations are then integrated numerically, usually using a variant of the Verlet algorithm, to calculate the positions and velocities of the molecules for the next time step [59]. As the system moves in phase space along a physical trajectory that is fixed by the equations of motion, MD can be regarded as a simulation of the system as it evolves over time. In this respect, MD simulations are very similar to real experiments. This is a great advantage of MD as it allows to study dynamical phenomena

such as diffusion, in addition to evaluating expectation values of static physical quantities.

When no external forces work on the system, the total energy is conserved in an MD simulation, hence MD samples the microcanonical NVE-ensemble. By contrast, experiments are often carried out at constant temperature, in the canonical NVT-ensemble. Special techniques have been developed to simulate systems at a constant temperature [42]. Two of the most famous methods are the Andersen thermostat [60] and the Nosé-Hoover thermostat [61, 62]. Both methods sample the canonical ensemble correctly, but both also influence the dynamics of the system in an artificial way. After equilibration, the probability that we find a particular configuration $X$ is proportional to the Boltzmann factor:

$$P_{NVT}(X) \propto \exp[-\beta U(X)]. \tag{4.1}$$

where $\beta = \frac{1}{k_B T}$ and $U$ is the potential energy.

Despite its successes, MD is limited in its scope by its inability to describe dynamical processes on a longer time-scale (e.g. activated processes such as diffusion in solids). Overcoming this limitation is a still a popular research topic, even with the exponential growth of computing power in the past decades.

On an atomic scale, the integration step is typically on the order of a femtosecond; this is necessary to correctly integrate the equations of motion. The short integration step also exposes the main limitation of a MD simulation: CPU-time. Computationally speaking, it is much too expensive to simulate processes on a 'macroscopic' time-scale. Diffusion in zeolites is a very good example of such a process. Diffusion coefficients for these systems can vary over many orders of magnitude. For high diffusion coefficients, a classical MD simulation suffices. However, if the diffusion coefficient is too low, molecules will only occasionally hop from one cage to another. To make a reliable estimate of the diffusion coefficient, one must observe a reasonable number of hops. The majority of the CPU-time is spent on molecules that wait for a fluctuation to give them sufficient kinetic energy to cross a barrier, making the direct simulation of the diffusion process prohibitively expensive. The higher the barrier between two adjacent sites, the longer the molecules remain trapped and hopping then becomes a *rare event* on the time-scale of the MD simulation.

## 4.1 Free energy profile from a MD simulation

A molecular dynamics simulation yields information about static as well as dynamic properties. However, it does not give information about the free energy of the system.

Details about how to extract a free energy profile along a certain coordinate from a MD simulation can be found in literature [42,63,64]. Below we discuss some of the most popular techniques to efficiently explore the *free energy surface* (FES).

### 4.1.1 Histogram method

The histogram method is by far the most simple method to study the FES of a molecular system. For a molecular system, the partition function and the free energy are given by:

$$Z = C \int \mathrm{e}^{-\beta \mathcal{H}(r,p)} dr dp, \tag{4.2}$$

$$F = -k_B T \ln Z. \tag{4.3}$$

The integration in equation 4.2 is performed over all degrees of freedom in the system. Now suppose we are interested in the free energy profile along a certain partitioning coordinate $Q(r,p)$, which can be a function of all the degrees of freedom of the system. In literature, such a partitioning coordinate is also referred to as a collective variable or a reaction coordinate. The coordinate $Q$ provides us with a way of partitioning all the available microstates of the system into sets of macrostates. The microstates are characterized by the positions and momenta of all the particles (denoted by $(r,p)$) and the macrostates are characterized by different values of $Q$ (denoted by $q$). As a consequence, the partition function and the free energy can also be partitioned into seperate contributions for every macrostate q:

$$Z(q) = C \int \mathrm{e}^{-\beta \mathcal{H}(r,p)} \delta(Q(r,p) - q) dr dp \tag{4.4}$$

$$F(q) = -k_B T \ln[Z(q)] \tag{4.5}$$

The probability that a system is in the macrostate q is thus:

$$\begin{aligned} p(q) &= \int p(r,p) \delta(Q(r,p) - q) dr dp \\ &= \frac{1}{Z} \int \mathrm{e}^{-\beta \mathcal{H}(r,p)} \delta(Q(r,p) - q) dr dp \\ &= \frac{Z(q)}{Z} = \frac{1}{Z} \mathrm{e}^{-\beta F(q)}. \end{aligned} \tag{4.6}$$

The free energy as a function of the coordinate q can be found by reversing this equation:

$$F(q) = -k_B T \ln p(q) - k_B T \ln Z \tag{4.7}$$

$$F(q) - F = -k_B T \ln p(q) \tag{4.8}$$

From a practical point of view, the free energy is retrieved by counting the amount of times the system is in a specific state, constructing a histogram, and subsequently applying equation 4.8 to calculate the free energy of each of the specific states. It is difficult to judge whether the free energy has converged when using this method. The best practice is to check if the computed histogram changes appreciably as a function of simulation time. The histogram method has poor accuracy in regions with low Boltzmann probability, e.g. transition states between local minima are not sufficiently sampled to obtain an accurate histogram.

### 4.1.2 Umbrella Sampling

The umbrella sampling method is one of the oldest enhanced sampling methods and it is inspired by the histogram method [65]. However, umbrella sampling introduces an external potential to enhance sampling in regions with low Boltzmann probability. The external potential is a function of the partitioning coordinate $Q$. The introduction of the external potential in the simulation gives rise to a biased free energy $F_b$:

$$Z_b(q) = C \int \mathrm{e}^{-\beta(\mathcal{H}(r,p)+U_b(Q))}\delta(Q(r,p)-q)drdp \tag{4.9}$$

$$\begin{aligned} F_b(q) &= -k_B T \ln[Z_b(q)] \\ &= -k_B T \ln p_b(q) + F_b \end{aligned} \tag{4.10}$$

The relation between the free energy of the unbiased system $F$ and the free energy of the biased system $F_b$ is straightforward:

$$\begin{aligned} F_b(q) &= -k_B T \ln[Z_b(q)] \\ &= -k_B T \ln[Z(q)\mathrm{e}^{-\beta U(q)}] \\ &= F(q) + U_b(q) \end{aligned} \tag{4.11}$$

However, in practice the method is slightly more complicated, a set of external potentials $\{U_b^{(k)}\}$ is introduced. Each external potential is designed to focus on a different region of the partitioning coordinate, such that the global set of external potentials spans an entire region of interest. The set of external potentials typically consists of harmonic functions that are centered at uniformly distributed positions $q_k$ over the region of interest:

$$U_b^k(q) = \frac{1}{2}k(q-q_k)^2. \tag{4.12}$$

For each of the external potentials in the set a different simulation is launched, yielding a set of histograms. These histograms (of the biased system) can be combined into a histogram

of the unbiased system using a variety of methods among which the weighted histogram analysis method (WHAM) is the most well-known [66]. More recently, a more advanced dynamic histogram analysis method (DHAM) that also provides kinetic information has been proposed [67].

### 4.1.3 Thermodynamic Integration

Another way of obtaining the free energy profile from multiple molecular dynamics runs is thermodynamic integration. Suppose the Hamiltonian of the molecular system depends on a parameter $Q$. The free energy as a function of $Q$ can then be calculated as follows:

$$F(q) = -k_B T \ln \left[ C \int \mathrm{e}^{-\beta \mathcal{H}(r,p;q)} dr dp \right] \tag{4.13}$$

$$\begin{aligned} \frac{\partial F}{\partial q} &= -k_B T \frac{C \int -\beta \frac{\partial \mathcal{H}}{\partial q} \mathrm{e}^{-\beta \mathcal{H}} dr dp}{C \int \mathrm{e}^{-\beta \mathcal{H}} dr dp} \\ &= \langle \frac{\partial \mathcal{H}}{\partial q} \rangle_q \end{aligned} \tag{4.14}$$

$$\begin{aligned} F(q_2) - F(q_1) &= \int_{q_1}^{q_2} \frac{\partial F}{\partial q} dq \\ &= \int_{q_1}^{q_2} \langle \frac{\partial \mathcal{H}}{\partial q} \rangle_q \, dq \end{aligned} \tag{4.15}$$

The subscript $q$ in equation 4.14 indicates that the average is computed in the ensemble where the Hamiltonian has a parameter $q$, hence the ensemble changes during the integration. In practice the computation consists of a numerical integration on a $\lambda$-grid and multiple simulation runs are needed to construct a free energy profile.

### 4.1.4 Metadynamics

Metadynamics offers a unified framework for simultaneously computing free energies and accelerating rare events. Suppose we are interested in the free energy profile along a certain partitioning coordinate Q. The free energy associated with a certain macrostate q is:

$$F(q) = -k_B T \ln \left[ C \int \mathrm{e}^{-\beta \mathcal{H}(r,p)} \delta[Q(r,p) - q] dr dp \right] \tag{4.16}$$

A history-dependent bias potential $U_b(q)$ that depends on a number of collective variables is introduced:

$$\begin{aligned} F_b(q) &= -k_B T \ln \left[ C \int \mathrm{e}^{-\beta(\mathcal{H}(r,p)+U_b(q))} \delta[Q(r,p)-q] dr dp \right] \\ &= -k_B T \ln \left[ \mathrm{e}^{-\beta U_b(q)} \; C \int \mathrm{e}^{-\beta \mathcal{H}(r,p)} \delta[Q(r,p)-q] dr dp \right] \\ &= U_b(q) + F(q) \end{aligned} \tag{4.17}$$

This bias is chosen such that the biased probability of each macrostate becomes equal for each macrostate: $p(q) = \frac{1}{\Omega}$. This implies that the free energy for each macrostate is also equal (see equation 4.8):

$$F_b(q) = -k_B T \ln p(q) + F_b = k_B T \ln \Omega + F_b = constant \tag{4.18}$$

Combining this equation with equation 4.17 yields:

$$F(q) = -U_b(q) + constant. \tag{4.19}$$

This equation demonstrates that, when a metadynamics simulation has converged, the free energy is simply equal to the negative bias potential (up to a constant).

MTD can explore complex free energy surfaces that are characterized by large free energy barriers. The bias is constructed by adding Gaussian contributions at certain times throughout the simulation. During the intervals between adding Gaussian contributions, the collective variables are averaged out to determine on which position to add the Gaussians. The components of the forces due to the Gaussian hills push the system away from previously visited spots and drive them towards new, yet undiscovered regions of the FES that would be practically inaccessible in unbiased MD.

$$U_b(q,t) = \sum_{t_i<t} A_i \mathrm{e}^{-\frac{(q-q_i)^2}{2\sigma_i^2}} \tag{4.20}$$

$A_i$ and $\sigma_i$ are the height and width of the Gaussian potentials at time $t_i$, and $q_i$ are the positions on which the Gaussians are centered. Determining the height and width is a matter of striking the right balance between accuracy and sampling efficiency. Smaller values mean more accurate results but slower convergence [68]. This can easily be understood. After the calculation has converged the sum of the Gaussians is a negative image of the FES and can hence be used to reconstruct it. Higher and wider Gaussians will fill in the well more quickly, but will fail to accurately describe the fine details of the FES. The number of Gaussians that is needed to fill the well is proportional to $(\frac{1}{\sigma_i})^n$, where $n$ is

the dimensionality of the problem. Hence, the efficiency of the algorithm scales exponentially with the number of dimensions involved. If $n$ is large, reasonable efficiencies can only be obtained by choosing Gaussians that are approximately the size of the well. However, a sum of Gaussians cannot reproduce features of the FES on a scale that is finer than $\sigma$.

By changing the Gaussian parameters in the history-dependent potential during the simulation one can continuously switch between a coarse (efficient) exploration of the FES and an accurate (computationally expensive) evaluation of the free energy. This is the idea behind more advanced metadynamics methods such as well-tempered metadynamics or variational metadynamics [69, 70]. In well tempered metadynamics, the height of the added hills is rescaled during the simulation [71]:

$$A_i = A \exp\left(-\frac{-U_b(q(t_i), t_i)}{k_B \Delta T}\right), \tag{4.21}$$

where $A$ is the starting height of the gaussian hills and $\Delta T$ is a temperature, so that the total history-dependent bias becomes

$$U_b(q,t) = \sum_{t_i<t} A \mathrm{e}^{-U_b(q(t_i),t_i)/k_B\Delta T} \mathrm{e}^{-\frac{(q-q_i)^2}{2\sigma_i^2}}. \tag{4.22}$$

One of the two main differences with metadynamics is that, as the added hills become increasingly smaller, the dynamics of all the microscopic variables gradually evolves towards thermodynamic equilibrium. The second crucial difference is that the bias potential does not fully compensate the FES, but converges to

$$U_b(q, t \to \infty) = -\frac{\Delta T}{T + \Delta T} F(q) + C, \tag{4.23}$$

in which $C$ is a constant. In literature, the ratio $\gamma = \frac{T+\Delta T}{T}$ is referred to as the bias factor [72]. In the long time limit ($\to \infty$), the probability distribution of the collective variable q becomes

$$p(q) \propto \exp\left(-\frac{F(q)}{k_B(T + \Delta T)}\right). \tag{4.24}$$

In literature, the ratio $\gamma = \frac{T+\Delta T}{T}$ is referred to as the bias factor [73]. From equation 4.24, the meaning of the temperature parameter $\Delta T$ introduced earlier becomes apparent. By tuning $\Delta T$, the extent of FES sampling can be controlled. It can readily be seen that ordinary MD is recovered in the limit $\Delta T \to 0$, and that the limit $\Delta T \to \infty$ yields standard metadynamics.

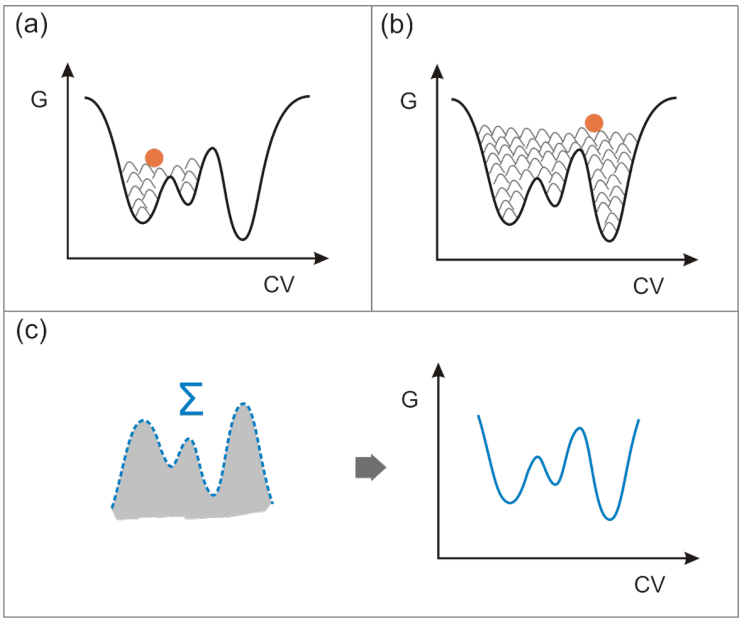


**Figure 4.1:** Schematic illustration of the metadynamics principle. The dynamics is driven by the free energy of the system and is biased by a history-dependent potential constructed as a sum of Gaussian hills centered along the trajectory of the collective variable. Over time, this potential fills the wells in the free energy surface. Along the axis defined by the collective variable, the sum of the Gaussian hills and the free energy becomes approximately constant. Figure taken from Ref. [74].

A metadynamics program should do two basic tasks: (1) keep track of the visited configurations in the CV space (or equivalently: the shape of the bias potential), and (2) add the corresponding forces to the microscopic dynamics. The former is accomplished by storing the Gaussians which have been added to the bias potential in a list. The list grows as the simulation proceeds. The latter requires the evaluation of the derivatives of the bias potential with respect to the microscopic coordinates. This is done using the chain rule:

$$\frac{\partial U_b(\boldsymbol{q},t)}{\partial r_i} = \sum_{j=1}^{d} \frac{\partial U_b(\boldsymbol{q},t)}{\partial q_j} \frac{\partial q_j(\boldsymbol{r})}{\partial r_i}, \tag{4.25}$$

where the notation $\boldsymbol{q}$ stands for the $d$-dimensional vector of collective variables $q_i$.

## 4.2 From metadynamics to dynamics

Metadynamics enables us to efficiently sample events that occur on longer timescales. Due to the contribution of the history-dependent bias potential, the system escapes free

energy minima much sooner than it would in an unbiased simulation. The dynamics of the system are thus accelerated by the gaussian hill contributions. This section explains how to calculate this acceleration factor and how to retrieve dynamical information from a metadymics run, using results from transition state theory.

The dynamics of many systems, for example diffusion in small-pore zeolites, can be described as a sequence of infrequent transitions between potential basins ("states"). As mentioned before, it is often impractical to calculate the dynamical properties of these systems with classical MD. However, transition state theory (TST) provides an elegant framework to access the dynamics on longer time scales [75]. In TST, the transition rate between states is given by the flux through a dividing surface that separates the states. As this flux is an equilibrium property of the system, the actual dynamics need not be performed. Two fundamental assumptions of TST are that each crossing of the dividing surface corresponds to an event where the system transitions from one state to another and that the system will lose all memory of this transition before the next event. To validate these assumptions, the dividing surface is best placed at the saddle points of the potential basins. In this way, we arrive at the picture of the evolution of rare-event systems as a sequence of uncorrelated transitions from state to state via saddle points on the free energy surface. Entirely in the spirit of metadynamics, a TST based method to extend the time scale of MD simulations without a priori knowledge of the free energy surface is explained in Refs. [76,77].

Consider a system of $N$ atoms in the canonical ensemble, governed by the classical equations of motion. Let $\boldsymbol{r}(t)$ and $\boldsymbol{p}(t)$ be the $3N$-dimensional vectors denoting the positions and the momenta of the atoms. Suppose the system resides in a local minimum of the free energy surface $V(\boldsymbol{r})$ and let's call this minimum state A. According to transition state theory, the escape rate from this state is equal to the flux through the boundary of state A:

$$k_{A\rightarrow}^{TST} = \langle |v_A| \delta_A(\boldsymbol{r}) \rangle_A. \tag{4.26}$$

In this equation, $v_A$ is the component of the velocity normal to the boundary of state A and $\delta_A(\boldsymbol{r})$ is a Dirac delta function at this boundary surface. The subscribt A indicates that the calculation of the ensemble average has been restricted to the part of phase space occupied by state A. The normal velocity $v_A$ and the boundary $\delta_A(\boldsymbol{r})$ are defined via a

collective variable $q(\boldsymbol{r})$ that clearly distinguishes state $A$ from its surroundings as follows:

$$q(\boldsymbol{r}) \begin{cases} > 0 \text{ if } \boldsymbol{r} \text{ is in state A} \\ = 0 \text{ if } \boldsymbol{r} \text{ is on the boundary of state A} \\ < 0 \text{ if } \boldsymbol{r} \text{ is not in state A} \end{cases}$$

Let $H$ be the Heaviside function so that $H(q(\boldsymbol{r})) \equiv H_A(\boldsymbol{r})$ is unity when the system is in state A and zero when it is not. The Dirac delta function $\delta_A(\boldsymbol{r})$ can now be defined as the gradient of this Heaviside function:

$$\delta_A(\boldsymbol{r}) = \boldsymbol{\nabla} H(q(\boldsymbol{r})). \tag{4.27}$$

The normal velocity $v_A$ is defined as

$$v_A = -\frac{\boldsymbol{\nabla} q}{|\boldsymbol{\nabla} q|} \cdot \dot{\boldsymbol{r}} \tag{4.28}$$

Written out in detail, equation 4.26 reads:

$$k_{A\rightarrow}^{TST} = \frac{\int\int |v_A| \delta_A(\boldsymbol{r}) H_A(\boldsymbol{r}) e^{-\beta K(\boldsymbol{p})} e^{-\beta V(\boldsymbol{r})} d\boldsymbol{r} d\boldsymbol{p}}{\int\int e^{-\beta K(\boldsymbol{p})} e^{-\beta V(\boldsymbol{r})} d\boldsymbol{r} d\boldsymbol{p}} \tag{4.29}$$

Introducing a bias potential $U_b(\boldsymbol{r})$ that is zero where $\delta_A(\boldsymbol{r}) = 1$ (Figure 4.2) the following is obtained:

$$\begin{aligned} k_{A\rightarrow}^{TST} &= \frac{\int\int |v_A| \delta_A(\boldsymbol{r}) H_A(\boldsymbol{r}) e^{-\beta K(\boldsymbol{p})} e^{-\beta [V(\boldsymbol{r}) + U_b(\boldsymbol{r})]} e^{\beta U_b(\boldsymbol{r})} d\boldsymbol{r} d\boldsymbol{p}}{\int\int e^{-\beta K(\boldsymbol{p})} e^{-\beta [V(\boldsymbol{r}) + U_b(\boldsymbol{r})]} e^{\beta U_b(\boldsymbol{r})} d\boldsymbol{r} d\boldsymbol{p}} \\ &= \frac{\left\langle |v_A| \delta(\boldsymbol{r}) e^{\beta U_b(\boldsymbol{r})} \right\rangle_{A_b}}{\left\langle e^{\beta U_b(\boldsymbol{r})} \right\rangle_{A_b}}, \end{aligned} \tag{4.30}$$

where the subscribt $A_b$ denotes that the ensemble average is now taken on the biased potential surface $V(\boldsymbol{r}) + U_b(\boldsymbol{r})$. Because the bias potential is zero on the boundary of state A, equation 4.30 reduces to

$$k_{A\rightarrow}^{TST} = \frac{\left\langle |v_A| \delta_A(\boldsymbol{r}) \right\rangle_{A_b}}{\left\langle e^{\beta U_b(\boldsymbol{r})} \right\rangle_{A_b}}, \tag{4.31}$$

a simple formula that relates that TST escape rate from the biased ensemble (numerator of equation 4.31) to the TST escape rate from the unbiased ensemble.

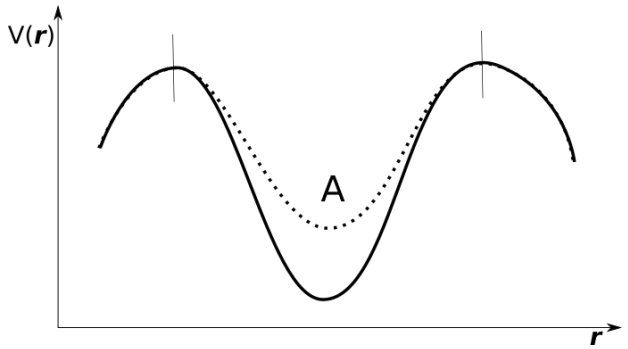


**Figure 4.2:** Simplified depiction of a state A on a free energy surface. State A is separated from its surroundings by two transition states, indicated by small vertical lines. The solid line represents the unbiased potential. The biased biased potential is drawn as a dashed line. As the bias is chosen to be zero around the boundary of state A, both lines overlap around the transition states.

In the biased system, the escape time $\tau_{A\rightarrow}$ from state $A$ will be considerably shorter than in the unbiased system. Hence, the system will evolve from state to state at an accelerated pace. However, the sequence of these transitions will remain unchanged from the unbiased system. The reason for this is that in the expression for the escape rate $k^{TST}_{A\rightarrow B}$, the denomitor is the partition function of state $A$. Substituting the denominator with the partition function for the biased state $A_b$ has no influence on the ratio of escape rates to neighbouring states:

$$\frac{k^{TST}_{A\rightarrow B}}{k^{TST}_{A\rightarrow C}} = \frac{k^{TST}_{A_b\rightarrow B}}{k^{TST}_{A_b\rightarrow C}}. \tag{4.32}$$

Considering that the escape time from state A is simply the inverse of the escape rate from state A, it is straightforward to relate the time scales of the biased an the unbiased system. Revisiting equation 4.31 we obtain:

$$\begin{aligned}
\tau_{A\rightarrow} &= \frac{1}{k^{TST}_{A\rightarrow}} = \frac{\left\langle e^{\beta U_b(\boldsymbol{r})}\right\rangle_{A_b}}{\left\langle |v_A|\delta_A(\boldsymbol{r})\right\rangle_{A_b}} \\
&= \frac{\frac{1}{n_{tot}}\sum_{i=1}^{n_{tot}} e^{\beta U_b[\boldsymbol{r}(t_i)]}}{n_{esc}/(n_{tot}\Delta t_{MD})} \\
&= \frac{1}{n_{esc}}\sum_{i=1}^{n_{tot}} \Delta t_{MD} e^{\beta U_b[\boldsymbol{r}(t_i)]},
\end{aligned} \tag{4.33}$$

where $n_{tot}$ is the total number of MD steps, $n_{esc}$ is the number of TST surface collisions (in TST, each surface collision leads to a reactive event), $t_i$ indicates the time at the $i$-th MD step, and $\Delta t_{MD}$ is the MD integration time step. The numerator was evaluated using

the ergodic hypothesis. The denominator is the escape rate from state $A$ in the biased system and is evaluated as the number of surface crossings divided by the total trajectory time. The average escape time from state $A$ is simply the total time evolved divided by the number of attempted escapes (or equivalently: surface collisions) so that the total time that the system has evolved is

$$\begin{aligned} t_b &= \sum_{i=1}^{n_{tot}} \Delta t_{MD} e^{\beta U_b[\boldsymbol{r}(t_i)]} \\ &= \sum_{i=1}^{n_{tot}} t_{b_i}. \end{aligned} \tag{4.34}$$

Clearly, the effect of adding the bias potential is to accelerate the total elapsed time and the amount by which the clock can be advanced after each MD integration step depends on the strength of the added bias at the instantaneous position of the trajectory. A so-called boost factor $\alpha$ that links the time scale in the biased system to the MD time can now be introduced

$$\alpha(t) = \frac{t_b}{t_{MD}} = \langle e^{\beta U_b(\boldsymbol{r})} \rangle = \frac{1}{n_{tot}} \sum_{i=1}^{n_{tot}} e^{\beta U_b[\boldsymbol{r}(t_i)]}. \tag{4.35}$$

This is the result as presented in Ref. [77], however there an extra time-dependency was added to the bias potential to account for a history-dependent bias potential (e.g. the bias potential constructed in metadynamics). Time is no longer an independent variable, but has become a statistically estimated property that converges to the exact result at long times because of equation 4.33 that is exact for infinitely long trajectories.

# 5 Methodology

## 5.1 Zeolite framework

Diffusion of propene is investigated in H-SAPO-34, a silico-alumino-phosphate material with a chabazite (CHA) topology; it consists of large elliptical chabazite cages ($10.0 \times 6.7$ Å$^2$) interconnected by relatively small 8-ring windows ($3.8 \times 3.8$ Å$^2$). Smaller 6- and 4-rings are also present in the material. The 8-ring windows restrict the diffusion of bulky hydrocarbons and therefore influence the selectivity, strongly biasing it towards lower olefins such as ethylene and propylene [34].

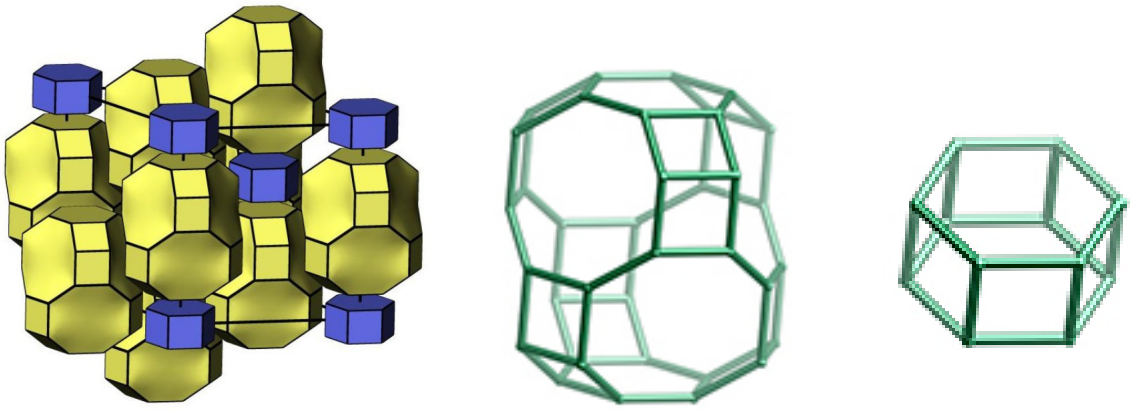

**(a)** **(b)** **(c)**

**Figure 5.1:** (a) Tiling arrangement of the Chabazite (CHA) structure. (b) Elliptical chabazite cage, clearly showing the 8-rings connecting the cages. (c) Smaller interconnecting building block. Figures are adapted from the IZA database [10].

A unit cell structure contains 36 T-sites. Two such structures are created. In the first structure, 18 Al atoms, 17 P atoms, and 1 Si atom are distributed over the T-sites, where the Brøndsted acid site is introduced by replacing a P atom by a Si atom. In the second

structure, an extra P atom is substituted in favor of a Si atom to create an 8-ring with 2 Brønsted acid sites. Various experimental studies report an (Al+P)/Si ratio of $\approx 11$, which corresponds to roughly one acid site per cage, as an optimum for the MTO process and show that lower ratios make the material more prone to catalyst deactivation [31, 34, 78]. According to this ratio, the unit cell would have to contain 3 Si atoms. However, here an attempt is made to isolate the effect of a single acid site on the free energy barrier for diffusion through a ring.

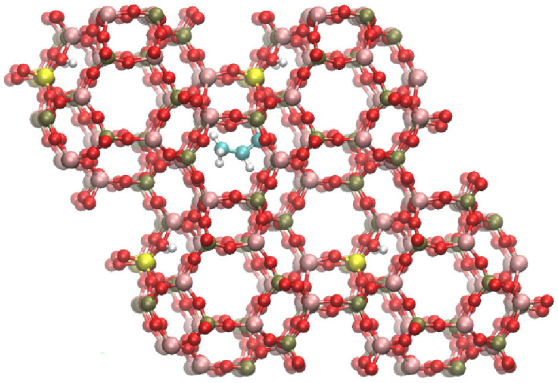

**Figure 5.2:** H-SAPO-34: $2 \times 2 \times 2$ supercell with one Brønsted acid site per unit cell viewed along $c$-direction . A propylene adsorbate is also present.

In the first unit cell structure, three different rings with a different chemical composition have been selected. In the second unit cell, only the ring with two acid sites is studied. In section 6.3, diffusion through these four distinct eight-ring types is studied in an effort to determine the influence of the ring chemistry on the height of the free energy barrier for diffusion. The ring types are defined in Figure 5.3. A type I ring is a ring without an acid site. In a type II ring, a P atom has been substituted by a Si atom, and the charge compensating proton is located in a neighbouring eight-ring. A type III ring is similar, but now the proton is in the ring. A type IV ring contains 2 Si atoms and 2 protons.

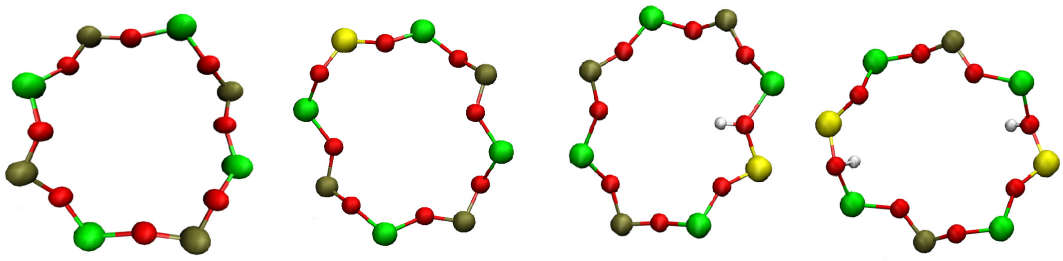

**(a)** Type I **(b)** Type II **(c)** Type III **(d)** Type IV

**Figure 5.3:** Four distinct types of eight-rings have been defined to asses the influence of the ring chemistry on the free energy barrier. From left to right these are: (a) Type I: $Al_4P_4O_8$ (b) Type II: $Al_4P_3O_8Si$, (c) Type III: $Al_4P_3O_7Si(OH)$, (d) Type IV: $Al_4P_2O_6Si_2(OH)_2$. In a type II ring, the charge-compensating proton is located in an adjacent eight-ring.

## 5.2 Molecular dynamics

### 5.2.1 Ab initio simulations

Many zeolites display negative thermal expansivity, which may have an effect on the size of the 8-ring windows studied at various temperatures in this thesis [79, 80]. Therefore, the force field calculations were preceded by ab initio relaxations of empty H-SAPO-34 unit cells. The DFT calculations have been performed with the CP2K software package [81], using a hybrid Gaussian and Plane Wave (GPW) basis set approach [82–84]. The revPBE functional was chosen over the PBE functional for its improved performance for solid-state calculations [85]. The DZVP-GTH basis set and pseudopotentials [86] with Grimme D3 dispersion corrections were used [87]. These relaxations with a fully flexible cell have been performed in the isobaric-isothermal NPT-ensemble for two distinct unit cells at three different temperatures (300K, 450K, 600K) and at a pressure of 1 atm (Table 5.2); the temperature was controlled by a chain of 5 Nosé-Hoover thermostats [88], and the pressure by a Martyna-Tobias-Klein (MTK) barostat [89]. The first unit cell contains one Brønsted acid site located in an eight-ring, the second unit cell has an eight-ring with two Brønsted acid sites.

**Table 5.1:** Overview of CP2K simulations parameters.

| | |
|---|---|
| Functional | PBE |
| Basis set | DZVP-GTH |
| Pair potential | DFT-D3 |
| Ensemble | NPT_F |
| Thermostat | Nosé-Hoover chain |
| Pressure | 1 atm |

The total simulation time is 20 ps (40000 integration steps of 0.5 fs). In these trajectories, the unit cell shape which occurred most was identified as the optimal cell shape. From the optimal unit cell shape, a $2 \times 2 \times 2$ supercell is subsequently constructed, which is then used as a starting structure for the MD runs in the NVT ensemble. Appendix B lists the obtained unit cell parameters for all ab initio relaxations. It is assumed that the additional volume fluctuations and the volume expansion caused by loading the pores with adsorbates is negligible. Hence the same volume is used independently of the loading. However, as the periodic box is a supercell, small local unit cell deformations are still possible.

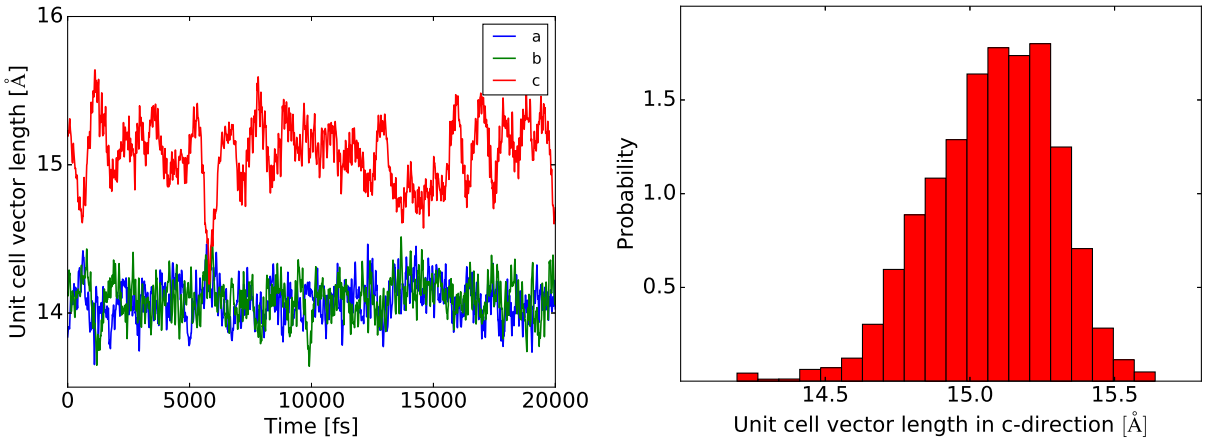


**(a)** **(b)**

**Figure 5.4:** (a) Evolution of the unit cell vectors during the ab initio relaxation of a H-SAPO-34 unit cell with one Brønsted acid site at 300 K. (b) A histogram of the unit cell vector in the *c*-direction, it has been normalized such that its integral is one.

In Figure 5.4a, the evolution of the unit cell vectors during an ab initio relaxation of a H-SAPO-34 unit cell with one Brønsted acid site is plotted. It is remarkable that the

fluctuation of the length of the unit cell vector along the $c$-direction is far greater than the fluctuation in the $a$- and $b$-directions. The expansion and contraction of the framework is thus highly anisotropic in the $c$-direction. This anisotropy has been reported both in computational and experimental studies [90, 91].

**Table 5.2:** Overview of the performed ab initio simulations.

| | 300 K | 450 K | 600 K |
|---|---|---|---|
| 1 acid site | ✓ | ✓ | ✓ |
| 2 acid sites | ✓ | ✓ | ✓ |

### 5.2.2 Force field calculations

The molecular dynamics engine used to simulate the diffusion process is DL_POLY Classic (version 1.9) [92]. To run a simulation, DL_POLY requires three input files: a FIELD file, a CONFIG file, and a CONTROL file. The FIELD file describes the force field, the CONFIG file provides DL_POLY with an initial configuration for a MD run, and the CONTROL file specifies the control variables for a MD run (e.g. temperature, integration step, etc.). Free energy calculations have been performed with PLUMED, an open source library for free energy calculations in molecular systems that works together with many popular molecular dynamics engines [93]. All MD simulations were performed in the NVT ensemble where the temperature is controlled by means of a Nosé-Hoover thermostat with a coupling time constant of 1 ps. As the Nosé-Hoover thermostat couples to the entire system, each particle is only lightly perturbed and hence the true dynamic quantities can be almost exactly recovered from the simulation. This is crucial when modeling diffusion [94]. The velocity Verlet integrator was used with a time step of 1 fs. Long-range interactions are evaluated using the smoothed particle mesh Ewald method with a cutoff radius of 11.8 Å [95].

The potential energy surface is defined by a fully flexible force field that can handle zeolites and silico-alumino-phosphate (SAPO) materials with any (Si,Al,P) distribution and with Brønsted acid sites [37]. As the propylene molecules tightly fit the narrow 8-rings of the H-SAPO-34 framework, it is conceivable that the flexibility of the framework can expedite diffusion by temporarily stretching the rings. The opposite case where the diffusion is hindered by shrinking rings is also possible. The parameters of the flexible force field are listed in Appendix A.

## 5.3 Enhanced sampling simulations

### 5.3.1 Collective variable

The construction of the free energy profile requires the definition of a collective variable. The collective variable should be able to distinguish between the different stable states and the transition states. Here, the coordinate $\xi$ is used to describe the position of a molecule with respect to a ring. $\xi$ is the projection of the center of mass of the molecule onto the axis that is normal to the ring plane and goes through the geometrical center of the ring. Ring crossings occur when $\xi$ changes sign. A plane is fitted to a ring which consists of N atoms using the following procedure. Suppose each of the atoms has coordinates $\boldsymbol{r_i}$. The geometrical center $\boldsymbol{r_c}$ can now be determined.

$$\boldsymbol{r_c} = \frac{1}{N}\sum_{i=1}^{N} \boldsymbol{r_i} \tag{5.1}$$

The normal to the plane $\boldsymbol{n_{plane}}$ of the ring can be determined by first subtracting out the geometrical center, then calculating weighted averages of the positions of the atoms constituting the ring and finally computing the cross product between the two weighted averages.

$$\boldsymbol{r_{i0}} = \boldsymbol{r_i} - \boldsymbol{r_c} \tag{5.2}$$

$$\boldsymbol{R_1} = \sum_{i=1}^{N} \boldsymbol{r_{i0}} \sin\left(\frac{2\pi i}{N}\right) \tag{5.3}$$

$$\boldsymbol{R_2} = \sum_{i=1}^{N} \boldsymbol{r_{i0}} \cos\left(\frac{2\pi i}{N}\right) \tag{5.4}$$

$$\boldsymbol{n_{plane}} = \frac{\boldsymbol{R_1} \times \boldsymbol{R_2}}{|\boldsymbol{R_1} \times \boldsymbol{R_2}|} \tag{5.5}$$

Because the center of the ring and the normal to the plane are now known, it is straightforward to write down the equation describing the $\xi$-axis.

$$\boldsymbol{r_\xi}(\xi) = \boldsymbol{r_c} + \xi \boldsymbol{n_{plane}} \tag{5.6}$$

The collective variable is the projection of the center of mass of the molecule $\boldsymbol{r_M}$ onto this $\xi$-axis.

$$\xi = (\boldsymbol{r_M} - \boldsymbol{r_c}) \cdot \boldsymbol{n_{plane}} \tag{5.7}$$

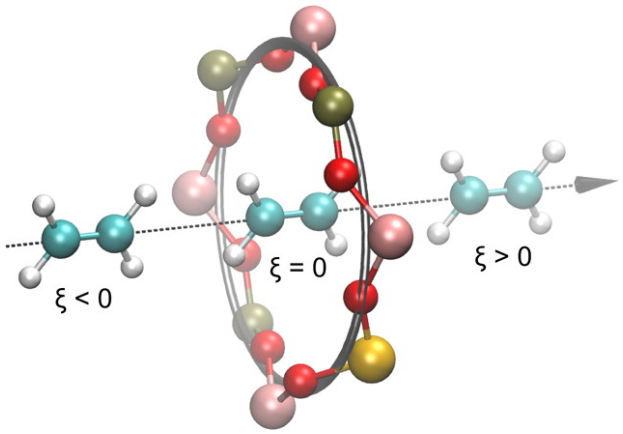


**Figure 5.5:** A graphical representation of the collective variable, the center of mass of the ethylene molecule is projected onto the $\xi$-axis. Figure taken from Ref. [37].

### 5.3.2 Restraints

The collective variable depends both on the position of the propylene molecule and the geometrical center of the ring. This implies that both the propylene molecule and the ring molecules will feel the influence of the metadynamics potential. To eliminate framework translation, the ring under study is fixed, using a harmonic potential with a force constant of 1500 kJ.mol$^{-1}$.

To ensure the propylene molecule does not escape the cage via a different ring than the one under investigation, restraints were added on the collective variable. Harmonic walls were placed at $\pm$ 8.5 Å along the $\xi$-axis with a force constant of 1500 kJ.mol$^{-1}$/Å$^2$. The distance to the $\xi$-axis ($\equiv r$) has also been restricted to a maximum of 5.0 Å by means of a harmonic wall with a force constant of 1500 kJ.mol$^{-1}$/Å$^2$. Together, these walls fence of a cylindrical space that is accessible to the center-of-mass of the propylene molecule. Of course, the restraints should not hinder the natural motion of the molecules in the cage. Therefore, the $r$ and $\xi$ coordinates of the propylene molecule have been tracked during a simulation without restraints (Figure 5.6a). It is clear that $|\xi_{max}| = 8.5$ Å and $r_{max} = 5$ Å are indeed reasonable choices.

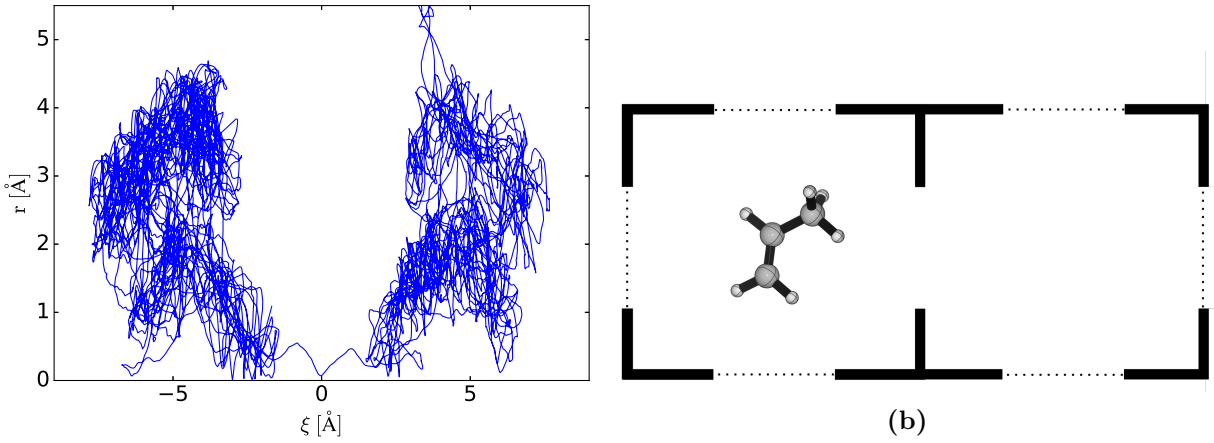


**Figure 5.6:** (a) Motion of a propylene molecule tracked throughout a metadynamics simulation with no extra restraints on the position of the molecule. Without extra restraints, the propylene molecule escapes the cage via different rings. (b) Schematic depiction of two neighbouring cages. Dashed lines represent restraints which have been put in place to ensure the propylene molecule only diffuses through the ring under investigation.

Instead of confining the propylene molecule to a cylindrical space around the $\xi$-axis, a better procedure is proposed. The first step is to identify all the eight-rings in a cage. In the next step, a $\xi$-axis is defined through each of these eight rings. Subsequently, the center of mass of the propylene molecule is projected orthogonally onto each of these axes. Because of the convex shape of the chabazite cages, these axes can be defined such these projections all have the same sign. By imposing that the projections on the different axes can not change sign, the molecule can be confined more precisely to the cage. However, the implementation of this procedure is cumbersome, which is why the simpler cylindrical approach was chosen.

### 5.3.3 Validation of free energy method

To eliminate obvious mistakes in the implementation of the free energy calculations, the free energy barrier has been determined using two different techniques: metadynamics and umbrella sampling.

The metadynamics results are obtained as follows. A first metadynamics simulation serves the purpose of generating possible starting configurations that are stored in a HISTORY file. Random snapshots are then taken from this HISTORY file and are formatted as

a CONFIG file to serve as input for a series of 10 new metadynamics simulations. The free energy profiles that result from these 10 simulations are combined into an average profile, which is the blue line in figure 5.7. The size of the error bars is one standard deviation. Finding reasonable compromises for the values of the metadynamics parameters (height and width of the gaussian hills, pace of deposition of the hills) is often a matter of trial and error. In these simulations the gaussian hills had a height of 0.5 kJ.mol$^{-1}$, a width of 0.5 Å, and one gaussian hill was deposited every 5000 integration steps.

A different procedure was applied to perform umbrella sampling. First, a simulation with a moving restraint pulls the molecule through the ring and back to minimize potential hysteresis effects. Next, the position of the molecule along the $\xi$ axis is checked for each frame of the HISTORY file; for each point in a series of 50 equidistant points ranging from -5 Å to 5 Å along the $\xi$-axis, the frame where the molecule was closest that point was converted into a CONFIG file. This CONFIG file serves as an input for a simulation where the center of mass of the molecule is kept in place by an umbrella with a spring constant of 100 kJ.mol$^{-1}$/Å$^2$. This relatively high value is necessary to ensure sufficient sampling in the region around the top of the barrier. However, one must be careful as choosing the spring constant too high can limit the rotational degrees of freedom of the molecule. To obtain the free energy profile, the histograms of the biased simulations were combined into the histogram of the unbiased system using the weighted histogram analysis method. The error bars were obtained via a bootstrapping method.

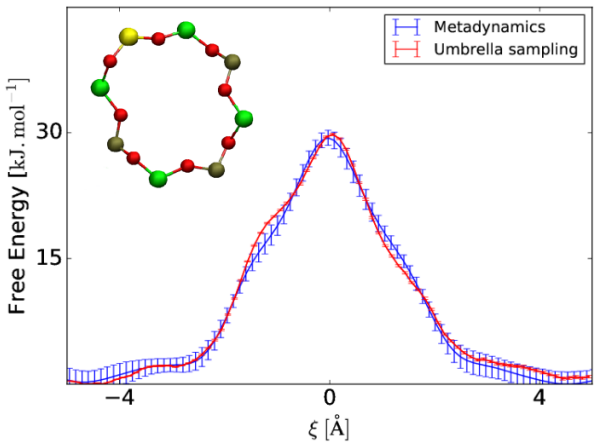


**Figure 5.7:** Free energy profile for propylene crossing a ring of type II. This free energy profile was determined using two different methods: metadynamics (blue line) and umbrella sampling (red line).

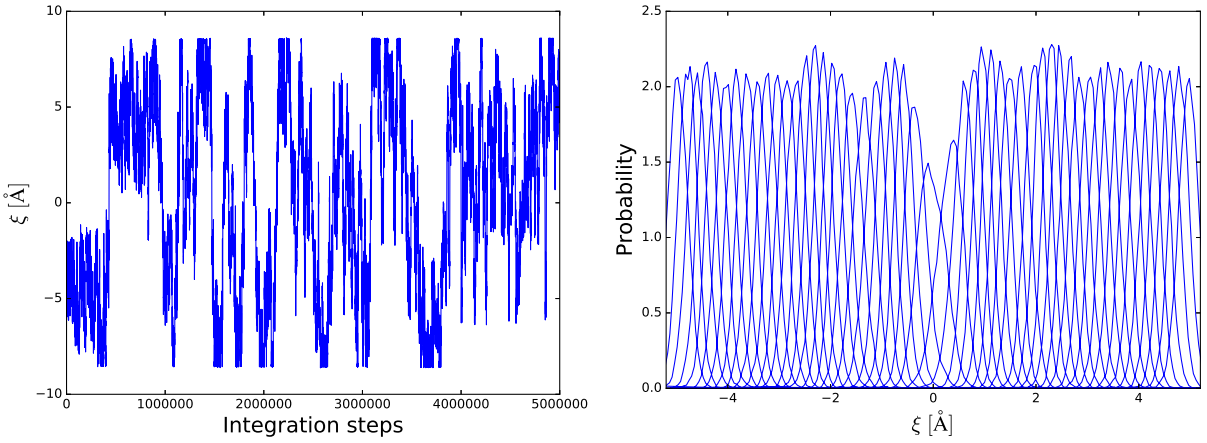


**(a)** **(b)**

**Figure 5.8:** (a) Position of the propylene molecule along the $\xi$ axis during a metadynamics run. Ring crossings occur whenever $\xi$ is 0. Diffusive behavior is clearly observed, an indication of convergence for the metadynamics simulation. (b) Histograms of the collective variable for each of 50 umbrella sampling runs. The condition of sufficient overlap between the umbrellas for the WHAM scheme is fulfilled. Each histogram has been normalized to one in the sense that $\int p(x)\mathrm{d}x = 1$. The histogram are wider around $\xi = 0$.

As an additional verification, metadynamics is also applied to determine the free energy barrier for the case of ethylene. The deposition stride for the Gaussian hills was 5000 steps, which amounts to a metadynamics time of 5 ps. The height and width of the Gaussian hills were 0.25 kJ.mol$^{-1}$ and 0.4 Å, respectively. Ten independent runs have been performed and subsequently averaged out to extract a sampling error. Figure 5.9 shows the resulting free energy barrier for diffusion of an ethylene molecule through a type II ring. The free energy barrier has a height of 31.9 kJ.mol$^{-1}$, which corresponds to 8.5 $k_BT$. This result is in excellent agreement with the barrier height that Ghysels *et al.* found by using classical MD simulations with the same force field, although it should be noted that Ghysels *et al.* reported the free energy profiles clustered into groups with different barrier heights. [37]. This effect was not found here, as only one ring is investigated at once.

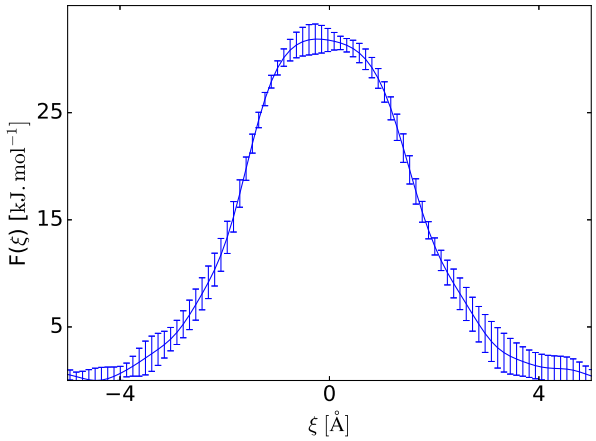


**Figure 5.9:** Free energy profile for ethylene crossing a ring of type II. This free energy profile was determined using metadynamics. Error bars are one standard deviation.

### 5.3.4 Simulations with a fixed bias

In order to estimate how large the entropic and the energetic contributions to the free energy barrier are, simulations with a fixed bias are performed. To ensure sufficient sampling, the propylene molecule should be able to move more or less freely along the $\xi$-axis. Therefore, the applied bias should approximately flatten out the free energy surface. This is achieved by fitting a $14^{\text{th}}$ order polynomial to the average metadynamics bias computed from earlier simulations.

The interaction energy between the propylene molecule and the zeolite lattice was separated from the energy of the zeolite structure by using the *decompose* option in DL_POLY. For technical reasons, this requires that the long-range interactions are calculated via the Ewald method instead of the usual smoother particle mesh ewald method. The ensemble averages over the biased and unbiased systems are connected via the formula

$$\langle E \rangle = \frac{\langle E \exp\left[\beta U_b(\xi)\right] \rangle_b}{\langle \exp\left[\beta U_b(\xi)\right] \rangle_b}, \tag{5.8}$$

where the subscript $b$ stands for an ensemble average over the biased systen, $E$ is the energy, and $U_b(\xi)$ is the added bias that depends only on the collective variable $\xi$. Here, the function $\langle E(\xi) \rangle$ is needed. To see how $\langle E(\xi) \rangle$ is derived, equation 5.8 is written out in detail:

$$\langle E \rangle = \frac{\int E(\boldsymbol{r}) \exp\left[\beta U_b(\xi)\right] \exp\left(-\beta[\mathcal{H}(\boldsymbol{r}) + U_b(\xi)]\right) \mathrm{d}\boldsymbol{r}}{\int \exp\left[\beta U_b(\xi)\right] \exp\left(-\beta[\mathcal{H}(\boldsymbol{r}) + U_b(\xi)]\right) \mathrm{d}\boldsymbol{r}}, \tag{5.9}$$

where $\boldsymbol{r}$ stands for all positional degrees of freedom of the system. The integration over $\boldsymbol{r}$ can be split into an integration over $\xi$, and over all degrees of freedom that are orthogonal to $\xi$, which are denoted by $\xi^{\perp}$. Additionally, a Dirac delta function is now introduced to extract the average energy for a specific value of the collective variable $\xi_0$:

$$\langle E(\xi_0)\rangle = \frac{\int\int \delta(\xi-\xi_0)E(\xi,\xi^{\perp})\exp\left[\beta U_b(\xi)\right]\exp\left(-\beta[\mathcal{H}(\xi,\xi^{\perp})+U_b(\xi)]\right)\mathrm{d}\xi\mathrm{d}\xi^{\perp}}{\int\int \delta(\xi-\xi_0)\exp\left[\beta U_b(\xi)\right]\exp\left(-\beta[\mathcal{H}(\xi,\xi^{\perp})+U_b(\xi)]\right)\mathrm{d}\xi\mathrm{d}\xi^{\perp}} \tag{5.10}$$

$$= \frac{\int E(\xi_0,\xi^{\perp})\exp\left[\beta U_b(\xi_0)\right]\exp\left(-\beta[\mathcal{H}(\xi_0,\xi^{\perp})+U_b(\xi_0)]\right)\mathrm{d}\xi^{\perp}}{\int \exp\left[\beta U_b(\xi_0)\right]\exp\left(-\beta[\mathcal{H}(\xi_0,\xi^{\perp})+U_b(\xi_0)]\right)\mathrm{d}\xi^{\perp}}. \tag{5.11}$$

The meaning of $\langle E(\xi)\rangle$ is now clear, the ensemble average is performed over all orthogonal degrees of freedom.

# 6 Results and discussion

## 6.1 Overview

It has generally been acknowledged that diffusion of the product species determines to a large extent the product selectivity and distribution for the MTO process. Nevertheless, theoretical diffusion studies for ethylene and propylene in small-pore zeolites are limited. This is especially true for the study of diffusion of propylene as diffusion itself becomes a rare event and special sampling techniques are required to obtain free energies of diffusion and diffusion coefficients [37]. The methodology developed in chapter 5 is applied here to assess the influence of the temperature, the ring chemistry, and the pore loading on the diffusion of propylene through H-SAPO-34.
First, the influence of the temperature is studied by determining the free energy barrier for diffusion of propylene molecules at 300 K, 450 K, and 600 K using metadynamics simulations. The relevant process temperature for the MTO process is 600 K. By repeating this procedure for each of the four ring types defined in section 5.1, the influence ofBrønsted acid sites in the ring on the free energy barrier for diffusion is also investigated. Special attention is given to the effect of adding Brønsted acid sites to the rings.

In an effort to better model the true process conditions during the MTO conversion, the loading of the pores is gradually increased by adding extra propylene molecules to the cages of H-SAPO-34. The effect on the free energy barrier is again determined by metadynamics simulations. However, these have only been performed at the relevant process temperature of 600 K. Additionally, to study the influence hydrocarbon pool molecules on diffusion, separate simulations are performed in which a hexamethylbenzene molecule is added to one of the cages instead of extra propylene molecules.

An attempt is made to recover kinetic information from biased MD simulations. Transition state theory is applied to relate the time scales of the biased and unbiased systems. Two

approaches for adding bias to the system are tested. One is to use well-tempered metadynamics, and the other is to use a fixed bias.

This chapter is concluded by condensing the obtained results into a global picture of diffusion of product species in H-SAPO-34.

## 6.2 Influence of temperature

The free energy barrier has been determined at 300 K, 450 K, and 600 K for each of the four ring types defined in section 5.1. The results are presented in Figures 6.1 and 6.2. For each curve in Figure 6.2, 10 independent metadynamics runs with a length of $10^7$ integration steps, which amounts to a metadynamics time of 10 ns, have been performed. Subsequently, the 10 free energy profiles obtained from these simulations are averged out to construct a mean free energy profile and to extract a sampling error. In each of these simulations, the height of the Gaussian hills is 0.5 kJ.mol$^{-1}$, the width is 0.5 Å, and the deposition stride is 5 ps (metadynamics time).

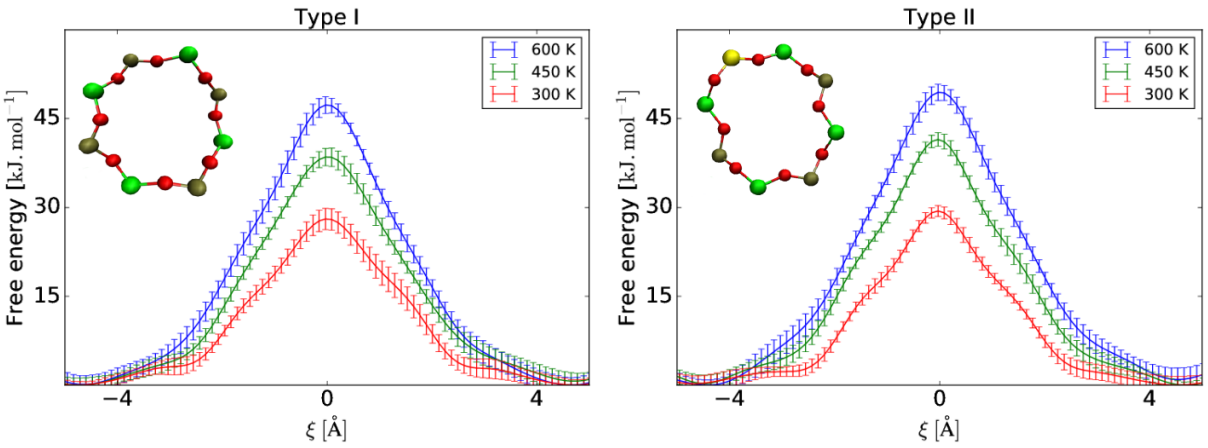


**(a)** **(b)**

**Figure 6.1:** The diffusion barrier is shown for 4 different eight-rings, the error bars are one standard deviation. At higher temperatures, sampling is more efficient, resulting in smaller error bars. The free energy barrier increases with temperature, this is mostly an entropic effect.

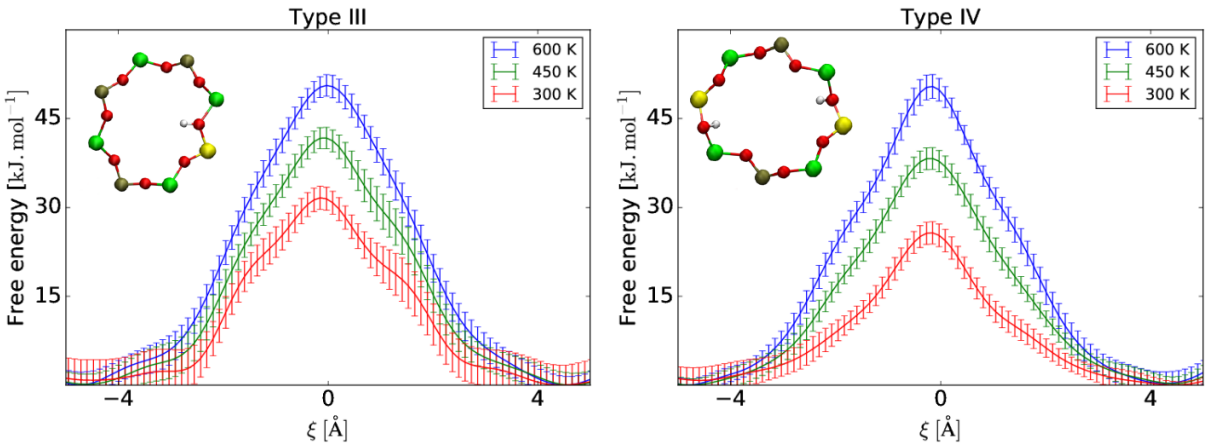


(a) (b)

**Figure 6.2:** The diffusion barrier is shown for 4 different eight-rings, the error bars are one standard deviation. At higher temperaturs, sampling is more efficient, resulting in smaller error bars. The free energy barrier increases with temperature, this is mostly an entropic effect.

An increase of the diffusion barrier from roughly 30 kJ.mol$^{-1}$ at 300 K to around 50 kJ.mol$^{-1}$ at 600 K is observed. These values correspond to 12 $k_B$T and 10 $k_B$T, respectively. This implies that a higher diffusion coefficient is expected at higher temperatures when the diffusion coefficient is interpreted as the product of an attempt rate and a success rate. The success rate is related to the free energy barrier by the Boltzmann factor $\exp(-F(0)/k_BT)$, which expresses the probability that the propylene molecule is at the top of the barrier.

The free energy barrier consists of two contributions: an energetic barrier and an entropic barrier.

Figure 6.3a shows the energy profile along the $\xi$-axis for a type I ring at 300 K, 450 K, and 600 K. This energy consists only of the non-bonding interactions (Coulomb and van der Waals interactions) between the propylene molecule and the H-SAPO-34 host lattice. No significant bond stretching or bending of the propylene molecule was observed, hence it was left out. Possible ring stretching has also been left out of the equation because it could not be separated from the total bond energy and valence energy of the zeolite lattice. At 300 K, the energetic barrier is approximately 9 kJ.mol$^{-1}$ and it rises to about 14 kJ.mol$^{-1}$ at 600 K. This small increase of 5 kJ.mol$^{-1}$ is probably caused by the negative thermal expansion coefficient of H-SAPO-34 and the associated reduction of the

accessible window area of the ring as defined by Ghysels *et al* [37]. At all temperatures, the energetic barrier makes up no more than one third of the free energy barrier for diffusion.

A noteworthy feature of the energy profiles shown in Figure 6.3 are the two energy wells left and right of the barrier that are caused by the attractive van der Waals interactions between the propylene molecules and the ring molecules. Energetically, it is thus favorable for the propylene molecules to be close to the ring.

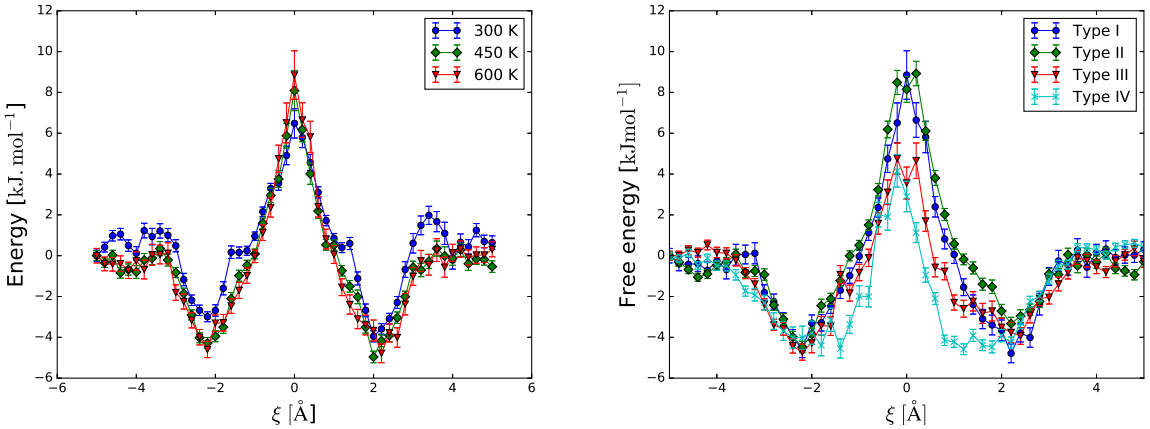


**Figure 6.3:** (a) Energy profile along the $\xi$-axis for a type I ring at 300 K, 450 K, and 600 K. At 600 K, the energy barrier is around 3 kJ.mol$^{-1}$ higher than at 300 K. Each simulation consists of 4 $\times 10^6$ integration steps. (b) Energy profile along the $\xi$-axis at 600 K for each of the four ring types. The presence of Brønsted acid sites lowers the energy barrier.

The free energy barrier for diffusion is dominated by the entropic contribution (-TS). This is clearly demonstrated in Figure 6.4a, in which both contributions to the free energy barrier for a type I ring at 600 K are plotted. The entropic barrier is due to the tight fit of the propylene molecule in the small eight-rings, which forces the molecule into a limited set of configurations when pushed through the ring. In the cages, the molecule can access more configurations because there is more space. Figure 6.4b shows a snapshot from a metadynamics simulation at 300 K which shows both a front and side view of a ring crossing event. The propylene molecule has a specific orientation, longitudinally along the $\xi$-axis, and crosses the elliptical eight-ring through its center.

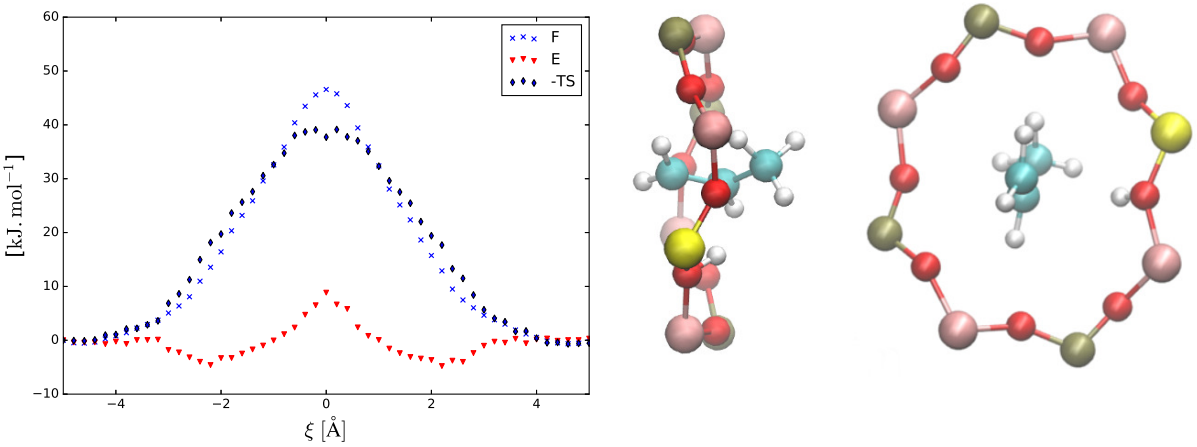


**(a)** **(b)**

**Figure 6.4:** (a) Energetic and entropic contributions to the free energy barrier for a type I ring at 600 K. Clearly, the dominant contribution to the free energy barrier is the entropic barrier (-TS). Error bars are not plotted for the sake of clarity. (b) The propylene molecule is oriented along the $\xi$-axis.

As the energy barrier increases relatively little with temperature (Figure 6.3a) compared to the free energy barrier (Figures 6.1 and 6.2), it can be concluded that the increase of the free energy barrier is dominantly entropy-driven. It has already been established that the entropy itself (S) is much higher in the cages than in the ring. Increasing the temperature further enhances this effect because of a decrease of the accessible window area caused by the negative thermal expansion coefficient of H-SAPO-34. However, this is likely a minor effect, as the temperature dependence of the entropic barrier (-TS) is fairly linear. This can be deduced by comparing the free energy and energy barrier heights at the three different temperatures in Figures 6.1a and 6.3a, respectively. As the temperature doubles, the entropic barrier (-TS) also approximately doubles.

## 6.3 Influence of ring chemistry

To assess how the presence of an acid site in an eight-ring influences diffusion, the analysis above has been repeated for each of the four ring types defined in section 5.1. It is expected that changing the chemistry of the ring affects its shape, for example via deviating bond lengths and bond angles. The shape of the ring impacts both the energetic and the entropic

barrier. For example, a tighter ring leads to stronger interactions between propylene and the ring atoms (energetic effect), and also leaves less space for the propylene molecule to pass (entropic effect).

Table 6.1 provides on overview of the free energy barrier heights for each ring type. A clear trend in the free energy barriers as a function of the amount of acid sites in the ring can not be immediately distinguished, although it stands out that for a type IV ring (with two acid sites), the free energy barrier is lower than for the other ring types. This is most likely an energetic effect, as can be seen in Figure 6.3b, in which the energy barriers for the four ring types are shown (at 600 K).

The observation that the free energy barrier for diffusion for ethylene is lowered with the addition of a second Brønsted acid site to a ring is suprising as for ethylene, diffusion is considerably slower when acid sites are introduced [37]. The interpretation of the diffusion coefficient as an attempt rate multiplied with a success rate, suggests that the presence of the acid sites affects the attempt rate, which is related to the motion of the propylene molecule inside the cages. To study how the presence of the acid sites influences the motion of the molecules in the cages and how the diffusion paths are altered is an interesting line of future research. The accessible window area (AWA) correlates very well with the number of ethene crossings [37]. To better understand why diffusion in acidic materials is slower, it would be interesting to see if there is also a correlation between the AWA and the chemical composition of the ring. Also, a deeper insight into how the chemical composition of the rings influences the AWA and the shape of the unit cell would enable tuning the ring chemistry for a larger AWA, leading to so-called faster rings and possibly the creation of 'diffusion highways' inside the material.

**Table 6.1:** Overview of the free energy barrier heights for each of the four ring types. Standard deviations have been provided. Units are in kJ.mol$^{-1}$.

| | Type I | Type II | Type III | Type IV |
|---|---|---|---|---|
| 300 K | 28.1 (1.8) | 29.4 (0.9) | 31.6 (1.9) | 25.7 (1.9) |
| 450 K | 38.5 (1.5) | 41.5 (1.2) | 41.7 (1.8) | 38.3 (1.8) |
| 600 K | 47.3 (1.4) | 49.5 (1.4) | 50.6 (1.8) | 50.4 (2.0) |

## 6.4 Increasing the pore loading

### 6.4.1 Adding extra propylene molecules

During the transport of the product species in the MTO process, it probable that situations arise in which multiple propylene molecules share a cage. Here, the loading of the cages is gradually increased to determine the influence of extra spectator molecules on the free energy barrier. Figures 6.5 and 6.6 show the various cases that are simulated. The ring under investigation is a type III ring, the temperature is always 600 K, and the total number of integration steps is always $10^7$, which amounts to a total metadynamics time of 10 ns. In these simulations, one propylene molecule is actively pushed through the ring by means of a metadynamics bias, whereas the other propylene molecules are simply spectator molecules. To prevent the extra spectator molecules from escaping via another ring than the one under investigation, they are confined to their cages by extra restraints on the collective variable $\xi$ and the radius $r$. For example, the center of mass of the spectator molecule in the right cage on Figure 6.5a can move freely in a cylindrical space with $\xi$ ranging from 0 Å to 8.5 Å, and with radius 5 Å.

As the loading of cage increases, the free energy inside that cage rises. Because the interactions between the propylene molecules are weak, this is most likely an entropic effect. The molecules inside the cage struggle for space and hence the entropy in the cage drops, resulting in a reduction of the free energy barrier. In case of one extra spectator molecule per cage, the effect is rather small. Both in the asymmetric (Figure 6.5a) and the symmetric case (Figure 6.5b), a reduction of the free energy barrier of about 5 kJ.mol$^{-1}$ is observed. When two spectator molecules are present in a cage, the effect is much more pronounced. In the asymmetric case (Figure 6.6a), an effect of around 20 kJ.mol$^{-1}$ is observed, while in the symmetric case (Figure 6.6b) there is a reduction of the free energy barrier of approximately 15 kJ.mol$^{-1}$. It is expected that other kinds of spectator molecules, e.g. ethylene, will have a similar effect, that is stronger as the spectator molecules are larger.

In Ref. [37] it was found that for propylene, diffusion itself is a rare event at the time scale of MD simulations and it is impossible to extract meaningful quantitative information. However, the reduction of the free energy barrier at higher pore loadings opens up new perspectives. Whereas Ghysels *et al.* performed MD simulations with a loading of one or two molecules per cage, the results here suggest that simulations with higher pore loadings, for example three to four molecules per cage, are better suited for a kinetic study

of diffusion with classical MD. Whether such loadings are relevant for the MTO process of course depends on the operating conditions.

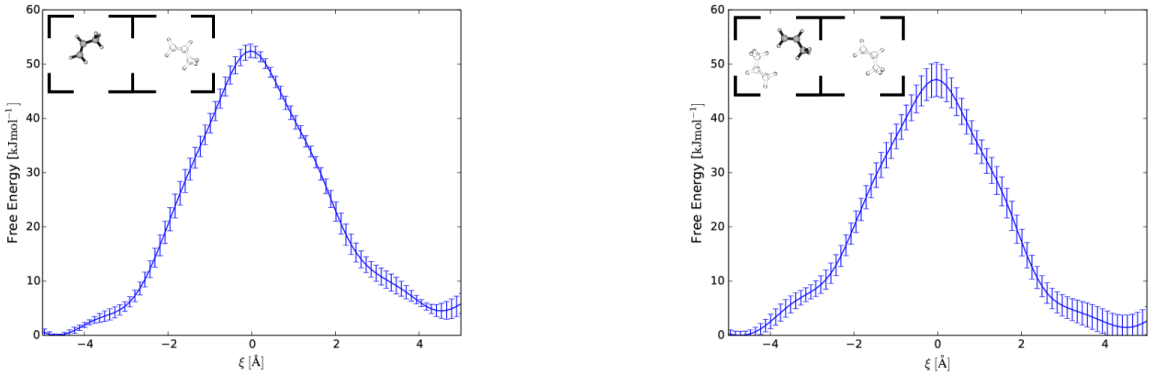


**(a)** **(b)**

**Figure 6.5:** Situations with one extra spectator molecule per cage. The coloured propylene molecule is actively pushed through the ring via a metadynamics bias. The transparent propylenes molecule are confined in their cages. Both in the asymmetric (a) and the symmetric (b) case, the free energy barrier is lowered by approximately 5 kJ.mol$^{-1}$.

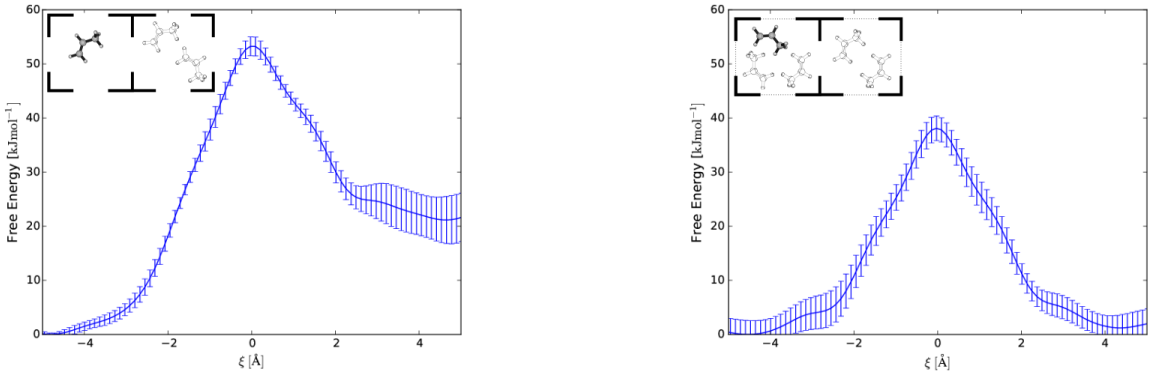


**(a)** **(b)**

**Figure 6.6:** Situations with two extra spectator molecules per cage. The coloured propylene molecule is actively pushed through the ring via a metadynamics bias. The transparent propylene molecules are confined to their cages. (a) The free energy profile is now highly asymmetrical, the free energy barrier is reduced by about 20 kJ.mol$^{-1}$. (b) In the symmetric case, the energy barrier is lowered by around 15 kJ.mol$^{-1}$.

### 6.4.2 Studying the presence of hydrocarbon pool species

In the MTO process, the hydrocarbon pool (HP) species grow by repeated methylation. Light olefins are subsequently eliminated, regenerating the HP species and closing the catalytic cycle. To assess the influence of the HP species on diffusion of the product species, metadynamics simulations are performed for the situation depicted in top left corner of Figure 6.7, in which the right cage contains a hexamethylbenzene (HMB) molecule, an important hydrocarbon pool species in the MTO process [14]. The ring under study was a type III ring, the temperature was 600 K, and the total amount of integration steps was $12 \times 10^6$, which adds up to a total metadynamics time of 12 ns. For technical reasons, an ethylene molecule was pushed through the ring instead of a propylene molecule.

Figure 6.7 shows the resulting free energy profile along the $\xi$-axis. The presence of the HMB molecule clearly has a large effect on the free energy landscape in the cage. The barrier for entering the cave is not raised, however, it is reasonable to suspect that the ethylene molecule will generally spend much less time in cages where large HP species are present, as the ethylene molecule experiences a heavily restricted freedom of motion inside these cages. For example, suppose an ethylene molecule accidentally enters a cage with a HMB molecule, it will likely immediately hop back again as there is no stable minimum, which leads to the picture of blocked sites that diminish the overal diffusion coefficient of the material. Additionally, once the ethylene molecule has been eliminated from a HP molecule, its first diffusion step will almost certainly be faster than the subsequent steps.

However, one must be careful when interpreting these results for three reasons. Firstly, the collective variable $\xi$ that is used here is very good at describing a profile for diffusion through a ring, it cannot capture in detail how the free energy surface changes inside the cages. Secondly, the restraints on the position of the propylene molecule (Section 5.3.2), in combination with the HMB molecule, can create artificial wells in the free energy surface. To see why, consider the situation that an ethylene molecule is stuck in between the HMB molecule and a harmonic wall that prevents the ethylene molecule from escaping through a neighbouring ring. As more metadynamics bias is added, the ethylene molecule will eventually rotate the HMB molecule and escape from its original position. Now suppose that it requires more energy to turn the bulky HMB molecule around than it takes to simply hop through a ring and the origin of the artificial well -which is an artifact of putting up the harmonic wall- becomes clear. The third reason is that the error bars on the results are much larger than for the other simulations. This is due to the introduction of extra degrees

of freedom into the system. In this case, these degrees of freedom are the position of the HMB molecule, its orientation, and all its internal degrees of freedom. Properly sampling these extra degrees of freedom takes a very long time, especially since the HMB molecule moves around rather slowly compared to the ethylene molecule.

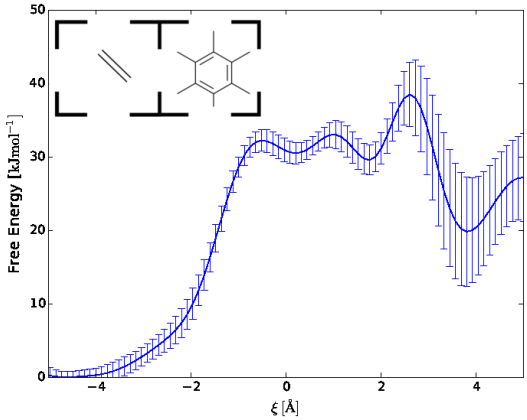


**Figure 6.7:** Free energy profile along $\xi$ with a so-called blocked site. The simulated situation is depicted in the top left corner: the right cage contains a hexamethylbenzene (HMB) molecule, which is an important hydrocarbon pool species in the MTO process.

## 6.5 Recovering kinetic information

### 6.5.1 Well-tempered metadynamics

In metadynamics, the sampling of rare events is accelerated by pushing the system away from local free energy minima. As explained in section 4.2, it is possible to link the time scales of the biased and the unbiased systems via transition state theory. It is essential that the bias potential is zero on the boundary surface seperating the free energy wells. To avoid depositing bias in the transition region around $\xi = 0$, well-tempered metadynamics simulations are performed with a bias factor (section 4.1.4) of 5. As demonstrated in Figure 6.9a), this bias factor ensures that the height of the gaussian hills is rescaled relatively quickly, which limits the risk of overfilling the potential wells. One gaussian hill is added every 15000 integration steps which is much slower than the time-scale of the jumping event (Figure 6.8), limiting the probability that the crossing of the barrier and the Gaussian deposition coincide. Figure 6.9b shows that no bias is deposited in the transition region. Further evidence is provided in Figure 6.10a, which shows how the bias is

constructed. Simulations are performed for a type I ring at 300 K, 450 K, and 600 K. The width and initial height of the Gaussian hills are 0.5 Å and 0.625 kJ.mol$^{-1}$, respectively. The total metadynamics time is 6 ns (6 $\times 10^6$ integration steps).

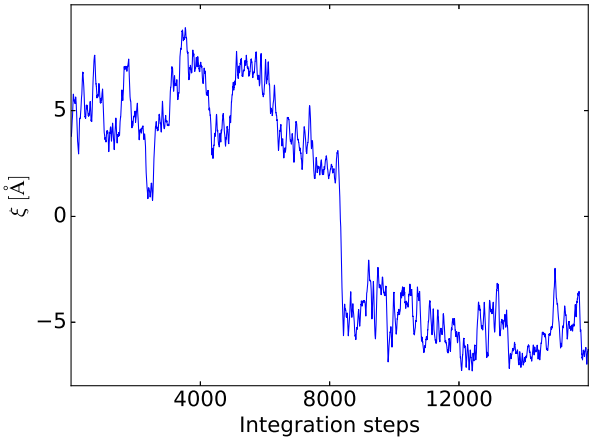


**Figure 6.8:** Position of a propylene molecule along the $\xi$-axis, tracked during a metadynamics simulation. Approximately 15000 integration steps are shown. Around the $8000^{th}$ step, the propylene molecule jumps through the ring. The molecule clearly spends most of its time in the cage, the jump itself takes less than a picosecond.

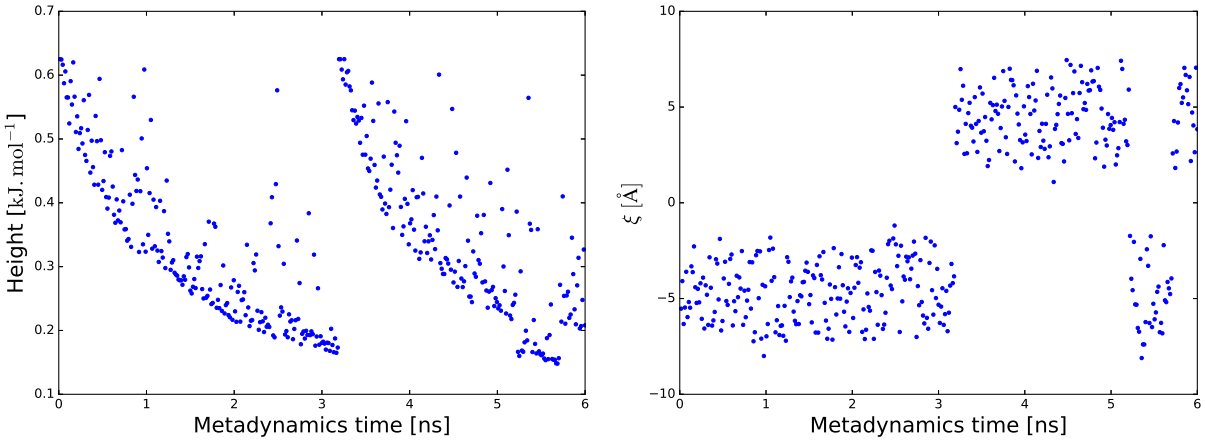


**(a)** **(b)**

**Figure 6.9:** A well-tempered metadynamics simulation, performed at 300 K. The ring under investigation is a type I ring. Only 3 ring crossings are observed. (a) The height of the Gaussian hills is rescaled as the simulations progresses, the crossings of the ring can clearly be seen. (b) The positions where the Gaussian hills are deposited. No bias is deposited in the region around $\xi = 0$.

Unfortunately, during the simulation at 300 K, only 3 ring crossings were observed. This is not enough to accurately determine the average waiting time for diffusion. For longer simulation times, the deposition of bias in the transition region is inevitable, unless a larger deposition stride or a smaller bias factor are specified. However, this can lead to unpractically long computation times. Figure 6.10b shows the evolution throughout the simulation of the acceleration factor that connects the metadynamics time scale to the time scale of the unbiased system. It displays clear kinks whenever the barrier between the two cages is crossed. In the beginning of the simulation, the acceleration factor is simply one as bias has not yet been added to the system. As the simulations proceeds and more hills are deposited, the acceleration factor rises. At the end of the simulation, the acceleration factor is just under 45, which is apparently too low to observe a significant number of crossings. In the simulations at 450 K and 600 K, more crossings were observed but bias was deposited in the transition region, which invalidates the results. Applying well-tempered metadynamics to find the acceleration factor and to compute diffusion coefficients proves to be very challenging.

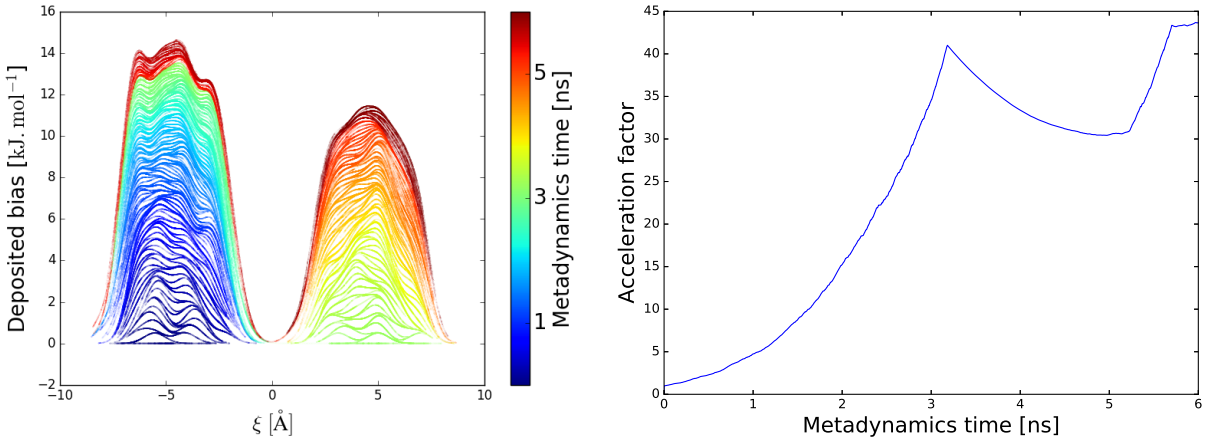


**(a)** **(b)**

**Figure 6.10:** (a) Evolution of the bias potential at during a well-tempered metadynamics simulation at 300 K. No bias is deposited at $\xi = 0$. (b) Evolution of the acceleration factor, showing a clear kink when the propylene molecule crosses the ring.

### 6.5.2 Fixed bias

Instead of constructing a history-dependent bias with well-tempered metadynamics, a fixed bias can be used to accelerate the dynamics of the system. Constructing such a fixed bias potential requires knowledge of the free energy profile, which has already been obtained from earlier simulations. This technique avoids the problem of not depositing bias over the transition state region, even for very long simulation times. Two other advantage compared to well-tempered metadynamics are that there is more control over the shape of the applied bias potential, and that no computation time is spent depositing the initial Gaussian contributions.

The biasing potential used here has been devised by Hamelberg *et al.* [96] and has the form

$$U_b(q) = f\mathrm{H}(E_b - F(q))\frac{[E_b - F(q)]^2}{[a + E_b - F(q)]}, \tag{6.1}$$

where $\mathrm{H}(x)$ is the Heaviside function, $E_b$ is a free energy level above which the added bias potential $U_b$ becomes zero, and $a$ controls the curvature of the bias potential. The multiplicative factor $f$ has been introduced as an extra parameter to add even more flexibility. In PLUMED, this biasing potential is implemented by first fitting a $14^{\text{th}}$ order polynomial to the average free energy profile extracted from earlier metadynamics runs. This polynomial

fit then plays the role of $F(q)$ in equation 6.1. Figure 6.11a shows the average free energy barrier for a type I ring at 300 K, the polynomial fit, and the shape of the added bias. The evolution of the acceleration factor during a simulation at 300 K is plotted in Figure 6.11b, it converges to a value close to 2300, which is almost two orders of magnitude larger than the acceleration factor found in the well-tempered metadynamics simulation.

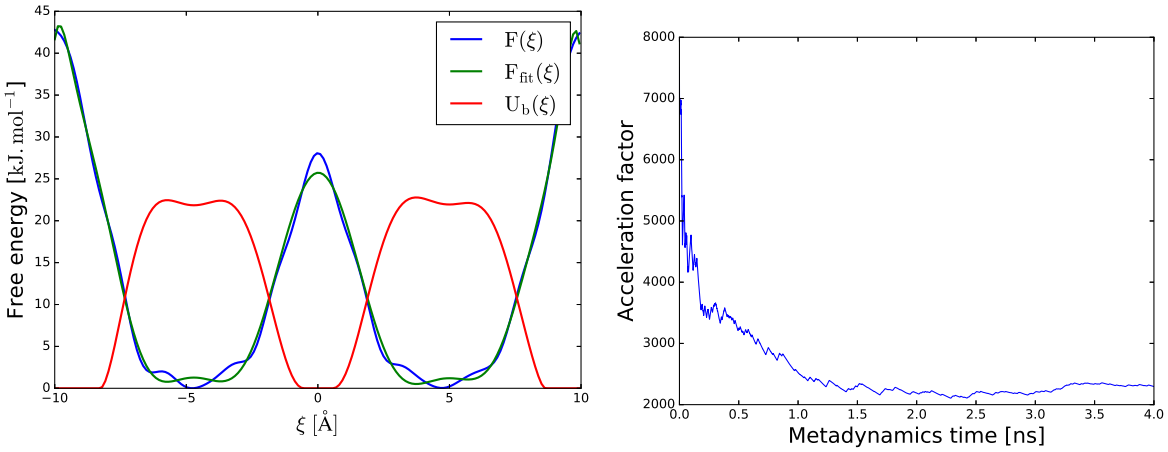


**(a)** **(b)**

Simulations are performed for a type I ring, again at 300 K, 450 K, and 600 K. Once a satisfactory amount of crossings is observed, the average waiting time $\tau$ for diffusion is calculated as

$$\tau = \frac{\alpha.t_{MTD}}{N_{crossings}}, \tag{6.2}$$

where $\alpha$ is the acceleration factor, $t_{MTD}$ is the total elapsed metadynamics time, and $N_{crossings}$ is the number of observed crossing events. The diffusion coefficient is subsequently calculated via equation 2.23 (section 2.3), where the average jump length $\lambda$ is assumed to be 10 Å. This average jump length was determined ad hoc based on the distance between the minima of the potential wells. Table 6.2 presents an overview of the used bias parameters, the number of observed crossings, and the computed diffusion coefficients for each of the simulations. These diffusion coefficients are in reasonable good agreement with literature data 2.5. Figure 6.11 is an Arrhenius plot of these diffusion coefficients. The activation energy extracted from this Arrhenius plot is 9.6 kJ.mol$^{-1}$. This value is on the same order as activation energies found in literature (see section 2.5).

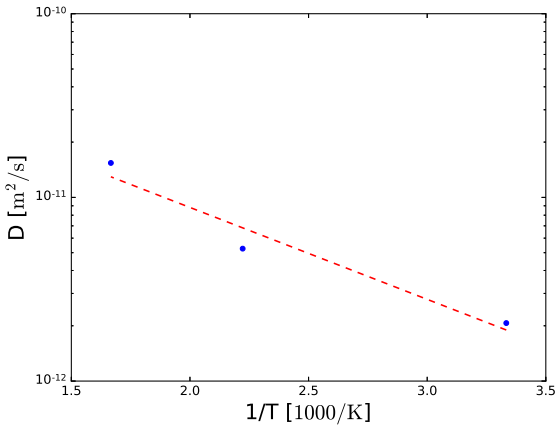


**Figure 6.11:** Arrhenius plot for the diffusion coefficient. The blue dots are the values obtained from the simulation. The dashed red line is a fit. An activation energy of 9.6 kJ.mol$^{-1}$ was extracted.

Although the diffusion coefficients estimated from the biased simulations are reasonably well behaved, in the sense that they lie relatively close to the fitted line, this result should be interpreted with caution. The assumption about the average jump length, though reasonable, has not been verified and the physical meaning of the obtained diffusion coefficients is still questionable. After all, diffusion coefficients are macroscopic properties whereas here, only crossings through one particular ring have been studied. The diffusion coefficients obtained here are likely a measure of the 'speed' of the ring under investigation, where 'speed' is related to the number of expected ring crossings. Considering there are 8 eight-ring windows in a chabazite cage, which are topologically equivalent [37], one could naively argue that the chance a propylene molecule escapes the cage is eight times higher in a real system than in the system currently under investigation (where the propylene molecule can only cross the ring under investigation). Therefore, the diffusion coefficient must be 8 times higher in the real system as well. Of course, introducing such an unsophisticated correction would be unwise, and much more research is necessary before one can truly model the kinetics of these rare diffusion events. For example, the introduction of the acid sites might affect the motion of the product species in the cages and lift the equivalence of the eight-rings by inducing structural deformations. In a more perfect world, one suggested approach is to extend the methodology used here to three dimensions, in order to fully model the free energy landscape inside the cages, instead of simply projecting it onto the $\xi$-axis. The knowledge of this energy landscape could then be used to construct a three dimensional biased potential by generalizing equation 6.1, which should then be added to all the cages,

not just a limited system of two cages as studied in this work. As the diffusion would no longer be one-dimensional, the diffusion coefficient should be calculated differently, by using the Einstein relation, as that requires less assumptions about the waiting time and the average jump length.

**Table 6.2:** Overview of the used bias potential parameters and of the obtained diffusion results.

| | $f$ | $E_b$ [kJ.mol$^{-1}$] | $a$ [kJ.mol$^{-1}$] | $N_{crossings}$ | $\alpha$ | $D$ [$10^{-12}\frac{m^2}{s}$] |
|---|---|---|---|---|---|---|
| 300 K | 1.3 | 24 | 8 | 38 | 2296 | 2.1 |
| 450 K | 1.1 | 34 | 10 | 59 | 689 | 5.4 |
| 600 K | 1.05 | 42 | 10 | 104 | 421 | 15.4 |

## 6.6 Resulting picture of diffusion

From a broader point of view, the goal of this research is to work towards a deeper understanding of the global picture of diffusion of the product species of the MTO process in H-SAPO-34. Figure 6.12 combines several of the insights and hypotheses gathered in this results section into a single overview picture.

In the top left corner, a propylene molecule is eliminated from a HP molecule, this elimination is catalyzed by a Brønsted acid site and is represented by a purple star. Its first diffusion step is likely to be a fast one (section 6.4.2). The molecule then continues its path through the structure via several slower diffusion steps (labelled 'slow' in Figure 6.12), the speed of which will depend on the process temperature. This is supported by the fact that the free energy barrier decreases with temperature (when expressed in units $k_BT$) and that the diffusion coefficient for hopping through a ring satisfies an Arrhenius relation.

Ghysels *et al.* have established that these hops will preferentially happen through rings with a larger AWA [37]. Gathering insight into the parameters that control the AWA of the rings is an interesting line of future research. As the propylene molecule progresses on its path out of the material, it might come across a so-called blocked site and accidentally jump in. However, the molecule is not expected to stay long as, on average, there is no stable minimum inside such a blocked cage. As the concentration of these blocked sites increases, the overall diffusion coefficient of the material is expected to decrease. In Figure 6.12, the propylene molecule turns around after hopping into a HP occupied cage and continues its

path into another cage which happens to contain extra spectator molecules. In section 6.4.1, it was found that in this case, the propylene molecule will also be inclined to leave sooner which is why the diffusion out of this cage was also labelled as fast. However, as diffusion out of the cages with extra spectator molecules is faster than diffusion into these cages, asymmetrical situations in which one cage houses more molecules than its neighbouring cages are probably rare.

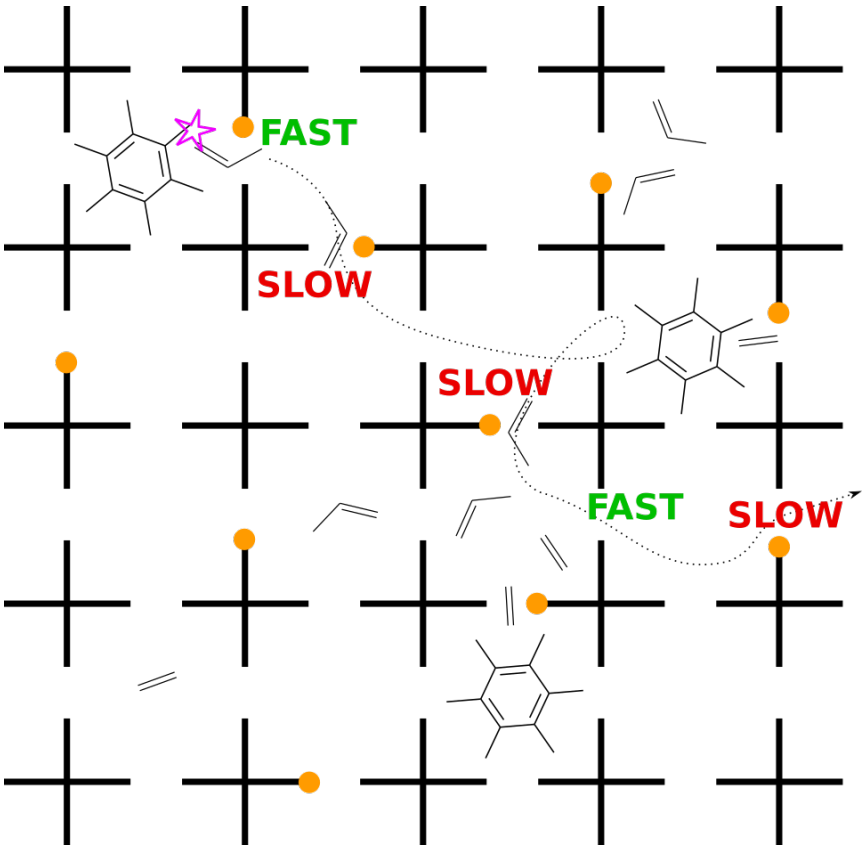


**Figure 6.12:** An overview picture of the diffusion process of product species of the MTO process in H-SAPO-34. The purple star represents the elimination of a propylene molecule from a HP molecule. Acid sites are represented by orange dots. Diffusion events have been labelled 'fast' or 'slow' based on the height of the free energy barrier for diffusion.

# 7 Conclusions

This research is relevant in the context of the methanol-to-olefins (MTO) process, in which methanol is converted into base chemicals such as ethylene and propylene. This conversion happens via a catalytic cycle that involves a complex hydrocarbon pool mechanism. For the MTO process, diffusion of the product species through small-pore zeolites determines to a large extent the product selectivity and distribution. Nevertheless, computational diffusion studies for ethylene and propylene in small-pore zeolites are scarce. This is especially true for the study of diffusion of propylene as diffusion itself is a rare event on the time scale of classical MD simulations and advanced sampling techniques are required to obtain free energy barriers for diffusion and diffusion coefficients [37]. This thesis explored the validity and applicability of advanced molecular dynamics techniques based on force fields to study the diffusion of propylene through the small eight-rings of H-SAPO-34, one of the most promising and industrially relevant catalysts for the MTO process. The influence of the temperature, the ring chemistry, and of the pore loading has been assessed.

Four different ring types with a varying amount of Brønsted acid sites have been defined. The free energy barrier for diffusion through each of these rings has been determined at 300 K, 450 K, and 600 K by metadynamics simulations. It has been established that the entropic contribution (-TS) dominates the free energy barrier. A significant increase of the free energy barrier with temperature was observed. The effect on the diffusion barrier of adding Brønsted acid sites to the ring is much less pronounced. However, Ghysels *et al.* found that, in case of ethylene, diffusion is considerably slower in acidic materials [37]. It is an interesting line of future research to see what drives this decline of the diffusion coefficient, as no significant effect on the height of the diffusion barrier is seen, especially at higher temperatures, where the entropic contribution to the free energy is dominant.

In an effort to better model the true process conditions during the MTO conversion, the loading of the pores was gradually increased by adding extra propylene molecules to the

cages. Several cases have been investigated with up to three molecules per cage. As the pore loading was increased, a considerable decrease of the free energy barrier was found. This observation opens up interesting new perspectives on the modelling of diffusion of propylene in small-pore zeolites. While Ghysels *et al.* [37] found that for propylene, diffusion is a rare event on the time scale of classical MD simulations, the results in this work suggest that this problem can be alleviated by increasing the pore loading. Whether such higher loadings are relevant for the MTO process of course depends on the operating conditions.

The key steps in the production of ethylene and propylene are repeated methylation of the HP species followed by olefin elimination. To gain insight into the effect of the presence of HP species on diffusion, a hexamethylbenzene (HMB) molecule was introduced into one of the cages. The effect of the HMB molecule on the free energy landscape inside the cage is substantial. No stable minima along the $\xi$ axis are observed, suggesting that the driving force for diffusion will point outwards of such a cage, creating a so-called blocked site. It should be noted that the methodology used here is incapable to capture all the details of the transformation free energy landscape inside the cage as the collective variable used here is one dimensional. However, it can be argued that diffusion of propylene is less probable through a cage in which a HMB molecule is present, as the HMB molecule severely restricts the freedom of motion of the propylene molecule in its cage.

Next, an attempt was made to recover kinetic information from biased MD simulations. The diffusion coefficients that are found for propylene are about two orders of magnitude lower than those reported for ethylene in Ref. [37]. However, as diffusion coefficients are macroscopic quantities, these results should be interpreted with caution. The obtained diffusion coefficients are arguably a better measure of the 'rate' of the ring under investigation, where 'rate' is related to the number of ring crossings.

This thesis was concluded with a hypothetical global picture of diffusion of the product species in H-SAPO-34. The speed of the diffusion increases with temperature. On the way out of the crystal, the product species will generally avoid, or spend less time in, sites that are occupied by large hydrocarbon pool species or even other spectator molecules. As the concentration of these large hydrocarbon pool molecules increases, the overall diffusion coefficient will decline. Asymmetrical situations in which a cage contains a higher concentration of product molecules than its neighbouring cages are unlikely.

# Appendices

# A Force field

## A.1 Force field

In MD a force field calculates the system's potential energy as a sum of various energy terms which can be classified into covalent and non-covalent terms.

$$E_{system} = E_{covalent} + E_{noncovalent} \tag{A.1}$$

Evaluating the energy and the forces involves summing over all pairs of particles, it is the most expensive part of an MD simulation. Both the covalent and the noncovalent terms can be further separated into several contributions. In general, the noncovalent terms are the most difficult to get right.

$$E_{covalent} = E_{bond} + E_{angle} + E_{dihedral} + E_{outofplane} \tag{A.2}$$

$$E_{noncovalent} = E_{electrostatic} + E_{vanderWaals} \tag{A.3}$$

The exact functional form of the potential energy function depends on the specific problem that is studied. Some of the most popular functional forms for the bond terms are harmonic and Morse potentials. It is crucial that these potentials accurately represent the interactions in the system being simulated. In the ideal case, this is ensured by fitting the potentials to quantum chemical data. In this work, a force field is used that can handle both zeolites and silico-alumino-phosphates with Brønsted acid sites. This general compatibility comes at the price of sacrificing accuracy. [37]

## A.2 H-SAPO-34

### A.2.1 Atom types

Oxygens play an important role in zeolite frameworks, therefore their charges have been differentiated depending on their local chemical environment. Two types have been distinguished: O1 for Si-O1(H1)-Al (Brønsted site), O2 for Si-O2-Si and Al-O2-P, and also O2 for Si-O2-Al (neighbour to a Brønsted site). In case of O2, equalizing these three oxygen types was found to be a reasonable approximation. [97] The oxygen charges are the only difference between these oxygens as their O-O van der Waals interactions do not distinguish between oxygen types. All charges in the system are optimized within the logical bounds imposed by the electroneutrality if pure silica, AlPO, and SAPO compositions.

**Table A.1:** Overview in the atom types in the zeolite framework H- SAPO- 34.

| atomtype | mass [amu] | charge [e] |
|---|---|---|
| O1 | 15.99940 | -0.725000 |
| O2 | 15.99940 | -1.050000 |
| Al | 26.98200 | 1.575000 |
| P | 30.97400 | 2.625000 |
| Si | 28.08600 | 2.100000 |
| H1 | 1.007970 | 0.200000 |

### A.2.2 Bond terms

Brønsted sites are parametrized by a Morse potential:

$$U(r) = E_0[\{1 - \exp(-k(r - r_0))\}^2 - 1]. \tag{A.4}$$

The OH term has been tuned to achieve a typical OH distance for Brønsted sites, which is around 0.96 Å

**Table A.2:** Bond term in H-SAPO-34.

| atom 1 | atom 2 | $E_0$ [eV] | $r_0$ [Å] | k [$Å^{-1}$] |
|---|---|---|---|---|
| O1 | H1 | 7.0525 | 0.94760 | 2.1986 |

### A.2.3 Angle terms

Harmonic angle terms have been introduced for the following triads: O-Si-O, Al-O-Si, P-O-Al, and Al-O-Si. The functional form is

$$U(\theta) = \frac{1}{2}k(\theta - \theta_0)^2. \tag{A.5}$$

Improving the harmonic approximation would certainly benefit the accuracy at higher temperatures; as previously mentioned, this force field sacrifices accuracy in favor of simplicity/compatibility.

**Table A.3:** Overview of the angle terms in H-SAPO-34.

| atom 1 | atom 2 | atom 3 | k [eV/Å$^2$] | $\theta_0$ [°] |
|---|---|---|---|---|
| O2 | Si | O1 | 1.494400 | 109.47000 |
| O2 | Si | O2 | 1.494400 | 109.47000 |
| Al | O1 | Si | 1.787500 | 140.83000 |
| P | O2 | Al | 1.787500 | 140.83000 |
| Al | O2 | Si | 1.787500 | 140.83000 |

## A.3 Propylene

### A.3.1 Atom types

**Table A.4:** Overview of the atom types in propylene.

| atom | mass [amu] | charge [e] |
|---|---|---|
| H2 | 1.007970 | 0.1159000 |
| C1 | 12.000000 | -0.3250000 |
| C3 | 12.000000 | -0.0849000 |
| C2 | 12.000000 | -0.2855000 |

### A.3.2 Bond terms

There are two types of C-C bond in propylene: the C2-C3 double bond is shorter than the C1-C3 bond. Now a harmonic potential has been used to parametrize the bonds:

$$U(r) = \frac{1}{2}k(r - r_0)^2 \tag{A.6}$$

**Table A.5:** Overview of the bond terms in propylene.

| atomtype 1 | atomtype 2 | k eV/Å$^2$ | $r_0$ [Å] |
|---|---|---|---|
| H2 | C* | 28.71 | 1.095 |
| C1 | C3 | 31.75 | 1.498 |
| C2 | C3 | 60.59 | 1.335 |

### A.3.3 Angle terms

Simple harmonic angle terms describe the bending of the propylene molecule:

$$U(\theta) = \frac{1}{2}k(\theta - \theta_0)^2. \tag{A.7}$$

**Table A.6:** Overview of the angle terms in propylene.

| atom 1 | atom 2 | atom 3 | $r_0$ [Å] | k [eV/Å$^2$] |
|---|---|---|---|---|
| H2 | C1 | C3 | 2.50 | 109.5 |
| H2 | C1 | H2 | 2.06 | 109.2 |
| C1 | C3 | C2 | 6.87 | 121.5 |
| C1 | C3 | H2 | 6.87 | 117.5 |
| C3 | C2 | H2 | 4.06 | 121.0 |
| C3 | C1 | H2 | 2.50 | 109.5 |
| C2 | C3 | H2 | 4.06 | 121.0 |
| H2 | C2 | H2 | 4.06 | 118.0 |

### A.3.4 Dihedral terms

The dihedral terms are described by a potential with the following form.

$$U(\phi) = A[1 + \cos(m\phi - \delta)]. \tag{A.8}$$

**Table A.7:** Overview of the dihedral terms in propylene.

| atom 1 | atom 2 | atom 3 | atom 4 | A [eV] | $\delta$ | m |
|---|---|---|---|---|---|---|
| H2 | C1 | C3 | C2 | -0.0087 | 0.0 | 3.0 |
| H2 | C1 | C3 | H2 | 0.0108 | 0.0 | 3.0 |
| C1 | C3 | C2 | H2 | 0.3254 | 180.0 | 2.0 |
| H2 | C3 | C2 | H2 | 0.3254 | 180.0 | 2.0 |

## A.4 van der Waals parameters

The nonbonding interactions in the zeolite framework not only include T-O and O-O terms, but also T-T terms. As is expected for zeolites where oxygen anions, with a larger size than T cations, dominate the reaction, the O-O terms contribute more than the other terms. The functional form of the nonbonding interactions is:

$$U(r_{ij}) = \left(\frac{A}{r_{ij}^{12}}\right) - \left(\frac{B}{r_{ij}^{6}}\right). \tag{A.9}$$

**Table A.8:** Overview of the van der Waals parameters.

| atom 1 | atom 2 | A [eV.Å$^{12}$] | B [eV.Å$^{6}$] |
|---|---|---|---|
| Si | Si | 0.5601 | 0.0004000 |
| Al | Si | 1.0153 | 0.0005000 |
| Al | Al | 1.8405 | 0.0006000 |
| O2 | Si | 172.6992 | 0.1086000 |
| O2 | Al | 342.4165 | 0.0786000 |
| O1 | Si | 218.1689 | 0.9583000 |
| O1 | Al | 259.9127 | 0.0786000 |
| O2 | O2 | 26877.9664 | 29.8306000 |
| O2 | O1 | 26877.9664 | 29.8306000 |
| O1 | O1 | 26877.9664 | 29.8306000 |
| P | Si | 0.5403 | 0.0003000 |
| P | Al | 0.9794 | 0.0004000 |
| P | P | 0.5211 | 0.0003000 |
| O2 | P | 118.3529 | 0.0930000 |
| O1 | P | 118.3529 | 0.0930000 |
| C1 | C1 | 1.96920e+4 | 18.0933 |
| C1 | C2 | 1.96920e+4 | 18.0933 |
| C1 | C3 | 1.96920e+4 | 18.0933 |
| C2 | C2 | 1.96920e+4 | 18.0933 |
| C2 | C3 | 1.96920e+4 | 18.0933 |
| C3 | C3 | 1.96920e+4 | 18.0933 |
| C1 | H2 | 2.80000e+3 | 5.8415 |
| C2 | H2 | 2.80000e+3 | 5.8415 |
| C3 | H2 | 2.80000e+3 | 5.8415 |
| C1 | H1 | 2.80000e+3 | 5.8415 |
| C2 | H1 | 2.80000e+3 | 5.8415 |
| C3 | H1 | 2.80000e+3 | 5.8415 |

**Table A.9:** Overview of the van der Waals parameters (continued).

| | | | |
|---|---|---|---|
| H2 | H2 | 3.84840e+2 | 1.9867 |
| H2 | H1 | 3.84840e+2 | 1.9867 |
| H1 | H1 | 3.84840e+2 | 1.9867 |
| C1 | Si | 0.00 | 0.00 |
| C2 | Si | 0.00 | 0.00 |
| C3 | Si | 0.00 | 0.00 |
| C1 | Al | 0.00 | 0.00 |
| C2 | Al | 0.00 | 0.00 |
| C3 | Al | 0.00 | 0.00 |
| C1 | P | 0.00 | 0.00 |
| C2 | P | 0.00 | 0.00 |
| C3 | P | 0.00 | 0.00 |
| H1 | Si | 0.00 | 0.00 |
| H2 | Si | 20918.49 | 21.9676 |
| H1 | Al | 0.00 | 0.00 |
| H2 | Al | 30972.76 | 28.2991 |
| H1 | P | 0.00 | 0.00 |
| H2 | P | 14763.60 | 17.2239 |
| C1 | O2 | 11000.00 | 17.654 |
| C2 | O2 | 11000.00 | 17.654 |
| C3 | O2 | 11000.00 | 17.654 |
| C1 | O1 | 11000.00 | 17.654 |
| C2 | O1 | 11000.00 | 17.654 |
| C3 | O1 | 11000.00 | 17.654 |
| H1 | O2 | 1556.40 | 5.5717 |
| H2 | O2 | 1556.40 | 5.5717 |
| H1 | O1 | 0.00 | 0.00 |
| H2 | O1 | 1556.40 | 5.5717 |

# B Unit cell parameters

This appendix provides an overview of unit cell parameters that have been obtained from the ab initio molecular dynamics simulations via the procedure described in section 5.2.1. In Table B.1 it can be seen that the addition of a second unit cell to a ring has a substantial effect on the shape of the unit cell.

**Table B.1:** My caption

| | T | a | b | c | $\alpha$ | $\beta$ | $\gamma$ |
|---|---|---|---|---|---|---|---|
| 1 acid site | 300 K | 14.10 | 14.07 | 15.21 | 89.76 | 89.85 | 119.62 |
| | 450 K | 14.03 | 14.08 | 14.91 | 90.18 | 90.24 | 119.85 |
| | 600 K | 14.08 | 14.04 | 14.77 | 90.02 | 89.91 | 119.96 |
| 2 acid sites | 300 K | 14.12 | 14.15 | 15.00 | 90.18 | 93.13 | 119.21 |
| | 450 K | 13.70 | 13.31 | 15.12 | 87.75 | 92.86 | 116.34 |
| | 600 K | 13.82 | 14.12 | 14.87 | 89.15 | 90.88 | 119.00 |

# Bibliography


[1] M. Muhler, "Jm thomas and wj thomas: Principles and practice of heterogeneous catalysis, vch, weinheim, 1997, isbn 3-527-29239-x, preis: 88,–dm," *Berichte der Bunsengesellschaft für physikalische Chemie*, vol. 101, no. 10, pp. 1560–1560, 1997.

[2] D. Schuring, *Diffusion in zeolites: towards a microscopic understanding*. PhD thesis, Technische Universiteit Eindhoven, 2002.

[3] G. Ertl, "Wilhelm ostwald: Founder of physical chemistry and nobel laureate 1909," *Angewandte Chemie International Edition*, vol. 48, no. 36, pp. 6600–6606, 2009.

[4] S. I. Zones and M. E. Davis, "Zeolite materials: recent discoveries and future prospects," *Current Opinion in Solid State and Materials Science*, vol. 1, no. 1, pp. 107–117, 1996.

[5] B. R. L. Virta and D. M. Flanagan, "2014 Minerals Yearbook," no. July, 2015.

[6] U.S. Geological Survey, "ZEOLITES (NATURAL) - Mineral Commodity Summaries," *World*, no. 703, pp. 186–187, 2011.

[7] V. Van Speybroeck, K. Hemelsoet, L. Joos, M. Waroquier, R. G. Bell, and C. R. A. Catlow, "Advances in theory and their application within the field of zeolite chemistry," *Chemical Society Reviews*, vol. 44, no. 20, pp. 7044–7111, 2015.

[8] J. V. Smith, "Topochemistry of Zeolites and Related Materials . 1 . Topology and Geometry," *Chemical reviews*, vol. 88, pp. 149–182, 1988.

[9] C. Baerlocher, L. McCusker, and D. Olson, *Atlas of zeolite framework types*, vol. 12. 2007.

[10] "Database of Zeolite Structures." `http://www.iza-structure.org/databases/`. Accessed: 2015-11-05.

[11] M. Occelli, *Fluid Catalytic Cracking VII:: Materials, Methods and Process Innovations*. Studies in Surface Science and Catalysis, Elsevier Science, 2011.

[12] Y. K. Park, C. W. Lee, N. Y. Kang, W. C. Choi, S. Choi, S. H. Oh, and D. S. Park, "Catalytic cracking of lower-valued hydrocarbons for producing light olefins," *Catalysis Surveys from Asia*, vol. 14, no. 2, pp. 75–84, 2010.

[13] N. A. Owen, O. R. Inderwildi, and D. A. King, "The status of conventional world oil reserveshype or cause for concern?," *Energy policy*, vol. 38, no. 8, pp. 4743–4749, 2010.

[14] K. Hemelsoet, J. Van der Mynsbrugge, K. De Wispelaere, M. Waroquier, and V. Van Speybroeck, "Unraveling the reaction mechanisms governing methanol-to-olefins catalysis by theory and experiment," *ChemPhysChem*, vol. 14, no. 8, pp. 1526–1545, 2013.

[15] C. D. Chang and A. J. Silvestri, "The conversion of methanol and other o-compounds to hydrocarbons over zeolite catalysts," *Journal of Catalysis*, vol. 47, no. 2, pp. 249–259, 1977.

[16] F. J. Keil, "Methanol-to-hydrocarbons : process technology," vol. 29, pp. 49–66, 1999.

[17] M. St "Methanol-to-hydrocarbons: catalytic materials and their behavior," *Microporous and Mesoporous Materials*, vol. 29, no. 12, pp. 3 – 48, 1999.

[18] C. H. Bartholomew, "Mechanisms of catalyst deactivation," *Applied Catalysis A: General*, vol. 212, no. 1, pp. 17–60, 2001.

[19] S. Kolboe, "On the mechanism of hydrocarbon formation from methanol over protonated zeolites," in *Methane ConversionProceedings of a Symposium on the Production of Fuels and Chemicals from Natural Gas* (R. H. D.M. Bibby, C.D. Chang and S. Yurchak, eds.), vol. 36 of *Studies in Surface Science and Catalysis*, pp. 189 – 193, Elsevier, 1988.

[20] D. Lesthaeghe, V. Van Speybroeck, G. B. Marin, and M. Waroquier, "Understanding the failure of direct cc coupling in the zeolite-catalyzed methanol-to-olefin process," *Angewandte Chemie International Edition*, vol. 45, no. 11, pp. 1714–1719, 2006.

[21] I. Dahl and S. Kolboe, "On the reaction mechanism for hydrocarbon formation from methanol over sapo-34: I. isotopic labeling studies of the co-reaction of ethene and methanol," *Journal of Catalysis*, vol. 149, no. 2, pp. 458 – 464, 1994.

[22] I. M. Dahl and S. Kolboe, "On the reaction mechanism for hydrocarbon formation from methanol over sapo-34: 2. isotopic labeling studies of the co-reaction of propene and methanol," *Journal of Catalysis*, vol. 161, no. 1, pp. 304 – 309, 1996.

[23] I. M. Dahl and S. Kolboe, "On the reaction mechanism for propene formation in the mto reaction over sapo-34," *Catalysis Letters*, vol. 20, no. 3, pp. 329–336.

[24] J. F. Haw and D. M. Marcus, "Well-defined (supra)molecular structures in zeolite methanol-to-olefin catalysis," *Topics in Catalysis*, vol. 34, no. 1, pp. 41–48.

[25] A. Sassi, M. A. Wildman, H. J. Ahn, P. Prasad, J. B. Nicholas, and J. F. Haw, "Methylbenzene chemistry on zeolite HBeta: Multiple insights into methanol-to-olefin catalysis," *Journal of Physical Chemistry B*, vol. 106, no. 9, pp. 2294–2303, 2002.

[26] W. Song, J. B. Nicholas, A. Sassi, and J. F. Haw, "Synthesis of the heptamethylbenzenium cation in zeolite-$\beta$: In situ nmr and theory," *Catalysis letters*, vol. 81, no. 1-2, pp. 49–53, 2002.

[27] M. Bjørgen, U. Olsbye, S. Svelle, and S. Kolboe, "Conversion of methanol to hydrocarbons: the reactions of the heptamethylbenzenium cation over zeolite h-beta," *Catalysis letters*, vol. 93, no. 1-2, pp. 37–40, 2004.

[28] W. Song, D. M. Marcus, H. Fu, J. O. Ehresmann, and J. F. Haw, "An oft-studied reaction that may never have been: Direct catalytic conversion of methanol or dimethyl ether to hydrocarbons on the solid acids hzsm-5 or hsapo-34," *Journal of the American Chemical Society*, vol. 124, no. 15, pp. 3844–3845, 2002.

[29] Y. Jiang, W. Wang, V. R. Marthala, J. Huang, B. Sulikowski, and M. Hunger, "Effect of organic impurities on the hydrocarbon formation via the decomposition of surface methoxy groups on acidic zeolite catalysts," *Journal of Catalysis*, vol. 238, no. 1, pp. 21–27, 2006.

[30] M. Vandichel, D. Lesthaeghe, J. V. der Mynsbrugge, M. Waroquier, and V. V. Speybroeck, "Assembly of cyclic hydrocarbons from ethene and propene in acid zeolite catalysis to produce active catalytic sites for {MTO} conversion," *Journal of Catalysis*, vol. 271, no. 1, pp. 67 – 78, 2010.

[31] B. P. Hereijgers, F. Bleken, M. H. Nilsen, S. Svelle, K.-P. Lillerud, M. Bjørgen, B. M. Weckhuysen, and U. Olsbye, "Product shape selectivity dominates the methanol-to-

olefins (mto) reaction over h-sapo-34 catalysts," *Journal of catalysis*, vol. 264, no. 1, pp. 77–87, 2009.

[32] J. Kärger, "Comment on pfg nmr self-diffusion of small hydrocarbons in high silica ddr, cha and lta structures[micropor. mesopor. mater. 109 (2008) 327]," *Microporous and Mesoporous Materials*, vol. 116, no. 1, pp. 715–717, 2008.

[33] A. Vidoni and D. M. Ruthven, "Diffusion of c2h6 and c2h4 in ddr zeolite," *Industrial & Engineering Chemistry Research*, vol. 51, no. 3, pp. 1383–1390, 2012.

[34] W. Dai, M. Scheibe, L. Li, N. Guan, and M. Hunger, "Effect of the methanol-to-olefin conversion on the pfg nmr self-diffusivities of ethane and ethene in large-crystalline sapo-34," *The Journal of Physical Chemistry C*, vol. 116, no. 3, pp. 2469–2476, 2012.

[35] J. Kärger and D. M. Ruthven, *Diffusion in zeolites and other microporous solids*. Wiley New York, 1992.

[36] I. M. Dahl and S. Kolboe, "On the reaction mechanism for propene formation in the mto reaction over sapo-34," *Catalysis Letters*, vol. 20, no. 3-4, pp. 329–336, 1993.

[37] A. Ghysels, S. Moors, K. Hemelsoet, and K. De Wispelaere, "Shape-selective diffusion of olefins in 8-ring solid acid microporous zeolites," 2015.

[38] S. Wilson and P. Barger, "The characteristics of SAPO-34 which influence the conversion of methanol to light olefins," *Microporous and Mesoporous Materials*, vol. 29, no. 1-2, pp. 117–126, 1999.

[39] A. Izadbakhsh, F. Farhadi, F. Khorasheh, S. Sahebdelfar, M. Asadi, and Y. Z. Feng, "Effect of sapo-34's composition on its physico-chemical properties and deactivation in mto process," *Applied Catalysis A: General*, vol. 364, no. 1, pp. 48–56, 2009.

[40] J. Q. Chen, A. Bozzano, B. Glover, T. Fuglerud, and S. Kvisle, "Recent advancements in ethylene and propylene production using the uop/hydro mto process," *Catalysis Today*, vol. 106, no. 1, pp. 103–107, 2005.

[41] R. M. Roque-Malherbe, *Adsorption and diffusion in nanoporous materials*. CRC press, 2007.

[42] D. Frenkel and B. Smit, *Understanding molecular simulation: from algorithms to applications*, vol. 1. Academic press, 2001.

[43] G. Saracco and V. Specchia, "Catalytic inorganic-membrane reactors: present experience and future opportunities," *Catalysis ReviewsScience and Engineering*, vol. 36, no. 2, pp. 305–384, 1994.

[44] M. Wang and Z. Li, "Nonideal gas flow and heat transfer in micro-and nanochannels using the direct simulation monte carlo method," *Physical Review E*, vol. 68, no. 4, p. 046704, 2003.

[45] R. Roque-Malherbe, *The Physical Chemistry of Materials: Energy and Environmental Applications*. CRC Press, 2009.

[46] R. Barrer, "Migration in crystal lattices," *Transactions of the Faraday Society*, vol. 37, pp. 590–599, 1941.

[47] D. Eley, H. Pines, and P. Weisz, *Advances in Catalysis*. No. v. 21 in Advances in Catalysis, Elsevier Science, 1971.

[48] J. Xiao and J. Wei, "Diffusion mechanism of hydrocarbons in zeolitesi. theory," *Chemical Engineering Science*, vol. 47, no. 5, pp. 1123–1141, 1992.

[49] B. W. H. van Beest, G. J. Kramer, and R. A. van Santen, "Force fields for silicas and aluminophosphates based on *ab initio* calculations," *Phys. Rev. Lett.*, vol. 64, pp. 1955–1958, Apr 1990.

[50] C. Wang, B. Li, Y. Wang, and Z. Xie, "Insight into the topology effect on the diffusion of ethene and propene in zeolites: A molecular dynamics simulation study," *Journal of Energy Chemistry*, vol. 22, no. 6, pp. 914 – 918, 2013.

[51] . Alfonso Pedone, . Gianluca Malavasi, . M. Cristina Menziani, . Alastair N. Cormack, , and . Ulderico Segre*, "A new self-consistent empirical interatomic potential model for oxides, silicates, and silica-based glasses," *The Journal of Physical Chemistry B*, vol. 110, no. 24, pp. 11780–11795, 2006. PMID: 16800478.

[52] A. Combariza, G. Sastre, and A. Corma, "Propane/propylene diffusion in zeolites: Framework dynamics," *Journal of Physical Chemistry C*, vol. 113, no. 26, pp. 11246–11253, 2009.

[53] G. Sastre, "Computational study of diffusion of propane in small pore acidic zeotypes AFX and AEI," *Catalysis Today*, vol. 226, pp. 25–36, 2014.

[54] N. Hedin, G. J. DeMartin, W. J. Roth, K. G. Strohmaier, and S. C. Reyes, "{PFG} {NMR} self-diffusion of small hydrocarbons in high silica ddr, {CHA} and {LTA} structures," *Microporous and Mesoporous Materials*, vol. 109, no. 13, pp. 327 – 334, 2008.

[55] D. H. Olson, M. A. Camblor, L. A. Villaescusa, and G. H. Kuehl, "Light hydrocarbon sorption properties of pure silica si-cha and itq-3 and high silica zsm-58," *Microporous and Mesoporous Materials*, vol. 67, no. 1, pp. 27 – 33, 2004.

[56] D. M. Ruthven and S. C. Reyes, "Adsorptive separation of light olefins from paraffins," *Microporous and Mesoporous Materials*, vol. 104, no. 13, pp. 59 – 66, 2007. Special Issue: Dedicated to the Late Lovat Rees in Appreciation of His Outstanding Contribution to Zeolite Science.

[57] J. Thijssen, *Computational physics*. Cambridge University Press, 2007.

[58] B. J. Alder and T. E. Wainwright, "Studies in Molecular Dynamics. I. General Method," *Journal of Chemical Physics*, vol. 31, pp. 459–466, Aug. 1959.

[59] L. Verlet, "Computer "experiments" on classical fluids. i. thermodynamical properties of lennard-jones molecules," *Phys. Rev.*, vol. 159, pp. 98–103, Jul 1967.

[60] H. C. Andersen, "Molecular dynamics simulations at constant pressure and/or temperature," *The Journal of Chemical Physics*, vol. 72, no. 4, pp. 2384–2393, 1980.

[61] S. Nos, "A unified formulation of the constant temperature molecular dynamics methods," *The Journal of Chemical Physics*, vol. 81, no. 1, pp. 511–519, 1984.

[62] W. G. Hoover, "Canonical dynamics: Equilibrium phase-space distributions," *Physical Review A*, vol. 31, pp. 1695–1697, Mar. 1985.

[63] A. Pohorille, *Free energy calculations theory and applications in chemistry and biology*. Berlin: Springer, 2007.

[64] C. D. Christ, A. E. Mark, and W. F. van Gunsteren, "Basic ingredients of free energy calculations: A review," *Journal of Computational Chemistry*, vol. 31, no. 8, pp. 1569–1582, 2010.

[65] G. M. Torrie and J. P. Valleau, "Nonphysical sampling distributions in Monte Carlo free-energy estimation - Umbrella sampling," *Journal of Computational Physics*, vol. 23, pp. 187–199, Feb. 1977.

[66] A. Ferrenberg and R. Swendsen, "New Monte Carlo technique for studying phase transitions," *Physical review letters*, vol. 61, no. 23, pp. 2635–2638.

[67] E. Rosta and G. Hummer, "Free energies from dynamic weighted histogram analysis using unbiased markov state model," *Journal of Chemical Theory and Computation*, vol. 11, no. 1, pp. 276–285, 2015. PMID: 26574225.

[68] A. Laio, A. Rodriguez-Fortea, F. L. Gervasio, M. Ceccarelli, and M. Parrinello, "Assessing the accuracy of metadynamics," *The Journal of Physical Chemistry B*, vol. 109, no. 14, pp. 6714–6721, 2005.

[69] A. Barducci, G. Bussi, and M. Parrinello, "Well-tempered metadynamics: A smoothly converging and tunable free-energy method," *Phys. Rev. Lett.*, vol. 100, p. 020603, Jan 2008.

[70] O. Valsson and M. Parrinello, "Variational approach to enhanced sampling and free energy calculations," *Physical review letters*, vol. 113, no. 9, p. 090601, 2014.

[71] A. Barducci, M. Bonomi, and M. Parrinello, "Metadynamics," *Wiley Interdisciplinary Reviews: Computational Molecular Science*, vol. 1, no. 5, pp. 826–843, 2011.

[72] P. Tiwary and M. Parrinello, "A time-independent free energy estimator for metadynamics," *The Journal of Physical Chemistry B*, vol. 119, no. 3, pp. 736–742, 2014.

[73] M. Bonomi, A. Barducci, and M. Parrinello, "Reconstructing the equilibrium boltzmann distribution from well-tempered metadynamics," *Journal of computational chemistry*, vol. 30, no. 11, pp. 1615–1621, 2009.

[74] V. Van Speybroeck, K. De Wispelaere, J. Van der Mynsbrugge, M. Vandichel, K. Hemelsoet, and M. Waroquier, "First principle chemical kinetics in zeolites: the methanol-to-olefin process as a case study," *Chemical Society Reviews*, vol. 43, no. 21, pp. 7326–7357, 2014.

[75] H. Eyring, "The activated complex in chemical reactions," *The Journal of Chemical Physics*, vol. 3, no. 2, pp. 107–115, 1935.

[76] A. F. Voter, "A method for accelerating the molecular dynamics simulation of infrequent events," *Journal of Chemical Physics*, vol. 106, no. 11, pp. 4665–4677, 1997.

[77] P. Tiwary and M. Parrinello, "From Metadynamics to Dynamics," *Physical Review Letters*, vol. 111, no. 23, p. 230602, 2013.

[78] N. Katada, K. Nouno, J. K. Lee, J. Shin, S. B. Hong, and M. Niwa, "Acidic properties of cage-based, small-pore zeolites with different framework topologies and their silicoaluminophosphate analogues," *The Journal of Physical Chemistry C*, vol. 115, no. 45, pp. 22505–22513, 2011.

[79] P. Tschaufeser and S. Parker, "Thermal expansion behavior of zeolites and alpo4s," *The Journal of Physical Chemistry*, vol. 99, no. 26, pp. 10609–10615, 1995.

[80] D. A. Woodcock, P. Lightfoot, L. A. Villaescusa, M.-J. Díaz-Cabañas, M. A. Camblor, and D. Engberg, "Negative thermal expansion in the siliceous zeolites chabazite and itq-4: A neutron powder diffraction study," *Chemistry of materials*, vol. 11, no. 9, pp. 2508–2514, 1999.

[81] J. Hutter, M. Iannuzzi, F. Schiffmann, and J. VandeVondele, "cp2k: atomistic simulations of condensed matter systems," *Wiley Interdisciplinary Reviews: Computational Molecular Science*, vol. 4, no. 1, pp. 15–25, 2014.

[82] J. VandeVondele, M. Krack, F. Mohamed, M. Parrinello, T. Chassaing, and J. Hutter, "Quickstep: Fast and accurate density functional calculations using a mixed gaussian and plane waves approach," *Computer Physics Communications*, vol. 167, no. 2, pp. 103–128, 2005.

[83] G. Lippert, J. Hutter, and M. Parrinello, "The gaussian and augmented-plane-wave density functional method for ab initio molecular dynamics simulations," *Theoretical Chemistry Accounts*, vol. 103, no. 2, pp. 124–140, 1999.

[84] B. G. LIPPERT, J. H. PARRINELLO, and MICHELE, "A hybrid gaussian and plane wave density functional scheme," *Molecular Physics*, vol. 92, no. 3, pp. 477–488, 1997.

[85] K. Yang, J. Zheng, Y. Zhao, and D. G. Truhlar, "Tests of the rpbe, revpbe, $\tau$-hcthhyb, $\omega$b97x-d, and mohlyp density functional approximations and 29 others against representative databases for diverse bond energies and barrier heights in catalysis," *The Journal of chemical physics*, vol. 132, no. 16, p. 164117, 2010.

[86] S. Goedecker, M. Teter, and J. Hutter, "Separable dual-space gaussian pseudopotentials," *Physical Review B*, vol. 54, no. 3, p. 1703, 1996.

[87] S. Grimme, J. Antony, S. Ehrlich, and H. Krieg, "A consistent and accurate ab initio parametrization of density functional dispersion correction (dft-d) for the 94 elements h-pu," *The Journal of chemical physics*, vol. 132, no. 15, p. 154104, 2010.

[88] G. J. Martyna, M. L. Klein, and M. Tuckerman, "Nosé–hoover chains: the canonical ensemble via continuous dynamics," *The Journal of chemical physics*, vol. 97, no. 4, pp. 2635–2643, 1992.

[89] G. J. Martyna, D. J. Tobias, and M. L. Klein, "Constant pressure molecular dynamics algorithms," *The Journal of Chemical Physics*, vol. 101, no. 5, pp. 4177–4189, 1994.

[90] K. De Wispelaere, B. Ensing, A. Ghysels, E. J. Meijer, and V. Van Speybroeck, "Complex reaction environments and competing reaction mechanisms in zeolite catalysis: insights from advanced molecular dynamics," *Chemistry–A European Journal*, vol. 21, no. 26, pp. 9385–9396, 2015.

[91] D. S. Wragg, R. E. Johnsen, P. Norby, and H. Fjellvåg, "The adsorption of methanol and water on sapo-34: in situ and ex situ x-ray diffraction studies," *Microporous and Mesoporous Materials*, vol. 134, no. 1, pp. 210–215, 2010.

[92] W. Smith and T. Forester, "Dl_poly_2. 0: a general-purpose parallel molecular dynamics simulation package," *Journal of molecular graphics*, vol. 14, no. 3, pp. 136–141, 1996.

[93] G. Tribello, M. Bonomi, D. Branduardi, C. Camilloni, and G. Bussi, "Plumed 2: New feathers for an old bird," *Computer Physics Communications*, vol. 185, no. 2, pp. 604–613, 2014.

[94] B. Smit and T. L. M. Maesen, "Towards a molecular understanding of shape selectivity.," *Nature*, vol. 451, no. 7179, pp. 671–678, 2008.

[95] U. Essmann, L. Perera, M. L. Berkowitz, T. Darden, H. Lee, and L. G. Pedersen, "A smooth particle mesh ewald method," *The Journal of chemical physics*, vol. 103, no. 19, pp. 8577–8593, 1995.

[96] D. Hamelberg, J. Mongan, and J. A. McCammon, "Accelerated molecular dynamics: a promising and efficient simulation method for biomolecules," *The Journal of chemical physics*, vol. 120, no. 24, pp. 11919–11929, 2004.

[97] J. D. Gale and N. J. Henson, "Derivation of interatomic potentials for microporous aluminophosphates from the structure and properties of berlinite," *J. Chem. Soc., Faraday Trans.*, vol. 90, no. 20, pp. 3175–3179, 1994.

# List of Figures

# List of Tables